INVESTIGATION OF MINERAL DUST AEROSOL – CHEMISTRY INTERACTIONS IN THE MARINE ENVIRONMENTS

A Thesis
Presented to
The Academic Faculty

by

Gill-Ran Jeong

In Partial Fulfillment
Of the Requirements for the Degree
Doctor of Philosophy in the
School of Earth and Atmospheric Sciences

Georgia Institute of Technology

December, 2007

INVESTIGATION OF MINERAL DUST AEROSOL – CHEMISTRY INTERACTIONS IN THE MARINE ENVIRONMENTS

Approved by:

Dr. Irina N.Sokolik, Advisor
School of Earth and Atmospheric Sciences
Georgia Institute of Technology

Dr. Anthanasios Nenes
School of Earth and Atmospheric Sciences and
School of Chemical and Biochemical Engineering
Georgia Institute of Technology

Dr. Paul Wine
School of Earth and Atmospheric Sciences and
School of Chemistry and Biochemistry
Georgia Institute of Technology

Dr. Irina Petropavlovskikh
Research Scientist, ESRL/NOAA

Dr. Rodney Weber
School of Earth and Atmospheric Sciences
Georgia Institute of Technology

Date Approved: August 8th, 2007

To my parents, with my great respect

ACKNOWLEDGEMENTS

From the bottom of my heart, I would like to give special thanks to my advisor, Professor Irina Sokolik. From Boulder to Atlanta, she gave me excellent guidance and teaching, all the while exercising great patience. Most of all, she encouraged me to brainstorm and to enjoy the many scientific issues that opened the world of mineral dust for me.

I would like to express my appreciation to Professors Paul Wine, Rodney Weber, Anthanasios Nenes, and Dr. Irina Petropavlovskikh for their fruitful comments and discussions on my thesis.

I also would like to thank my previous mentors, Professors Yoo-Keun Kim, Soon-Chang Yoon, Zhuangjie Li, and Walter Robinson for their guidance and advice in my undergraduate and Master's pursuits. Their guidance was invaluable.

And what would an education be without the many hours of interaction with other students? Our group members, Kremena, Anton, Greg, Tom, Drexel, Hyung-Jin, Prashant, and Kurosaki, had many constructive discussions and agreeable conversations. I also would like to thank the EASers, especially, Sangmyung, Changsub, Yunsoo, Saewung, Sangil, Paula, and Carlos for sharing a wonderful camaraderie at Georgia Tech. Thanks to all of you. Also, a big thanks to Dr. Eun-Su Yang for his mature advice.

I would like to express my thanks to my best friends, Young-Hee and Min-Jeong for their friendship and advanced ideas. And also to my lovely Joo-Hyun, Hye-Ran, Young-Geun, Eun-Jeong, Sun-Kyoung, Sunyoung, and Namjung for their cheers and prayers.

I deeply appreciate my parents for their tremendous love and constant support to me. They were always proud of me and uplifted me every moment throughout my life. To my lovely brother and sister - thanks for your encouragement and endless love.

TABLE OF CONTENTS

LIST OF TABLES

LIST OF FIGURES

Page

Page

LIST OF ABBREVIATIONS

Chapter 2

HC1999	*He and Carmichael*, 1999
D1987	*d'Almeida* 1987
D1991	*d'Almeida et al.*, 1991
H1998	*Hess et al.*, 1998
C2004	*Clarke et al.*, 2004
C04	Dust size distribution measured by Clarke et al. (2004) during the ACE-Asia.
O98	Dust size distribution used in the optical package of aerosols and clouds (1998).
D87	Dust size distribution in background aerosols, published by d'Almeida et al. (1987).
L91	Dust size distribution in the case of longrange transport, published by d'Almeida et al. (1991).
B02	The dust size distribution used for the retrieval of AERONET site at Bahrain published by Duvobik et al. (2002).
H10	Strong absorbing dust composed of 90% kaolinite and 10% hematite
H5	Moderate absorbing dust composed of 95% kaolinite and 5% hematite
H1	Low absorbing dust composed of 99% kaolinite and 1% hematite

Chapter 4

NO_DUST	Aerosol and gas species loading scenario, clean marine (dust-free) atmosphere.
DUST_ONLY	Aerosol and gas species loading scenario, clean marine atmosphere with dust embedded in the layer from 1 to 3km.
MIXED_DUST	Aerosol and gas species loading scenario, polluted marine atmosphere with dust mixed with other aerosol and gaseous species, embedded in the layer from 1 to 3km.

LIST OF SYMBOLS

Chapter 3

Ca0A50Q50	the mass fraction among calcite, clay aggregates, and quartz of 0: 50: 50
Ca50A50Q0	the mass fraction among calcite, clay aggregates, and quartz of 50: 50: 0
Ca50A0Q50:	the mass fraction among calcite, clay aggregates, and quartz of 50: 0: 50
Ca50A25Q25:	the mass fraction among calcite, clay aggregates, and quartz of 50: 25: 25
Ca100A0Q0	the mass fraction among calcite, clay aggregates, and quartz of 100: 0: 0
Ca0A50Q50_F10	the dust mixture with mass fraction of calcite, clay aggregates, and quartz is 0:50:50 and the fine mode (SMD<2.5um) is 10% of dust size distribution.
Ca0A50Q50_F50	the dust mixture with mass fraction of calcite, clay aggregates, and quartz is 0:50:50 and the fine mode (SMD<2.5um) is 50% of dust size distribution.
Ca0A50Q50_F90	the dust mixture with mass fraction of calcite, clay aggregates, and quartz is 0:50:50 and the fine mode (SMD<2.5um) is 90% of dust size distribution.

Chapter 4

Ca0A50(H1)Q50_C04	low (no) alkalinity, low absorption, the dust size distribution shifted to coarse mode (C04)
Ca0A50(H1)Q50_B02	low (no) alkalinity, low absorption, the dust size distribution shifted to fine mode (B02)
Ca0A50(H10)Q50_C04	low (no) alkalinity, high absorption, the dust size distribution shifted to coarse mode (C04)
Ca50A50(H1)Q0_C04	high alkalinity, low absorption, the dust size distribution shifted to coarse mode (C04)
Ca50A50(H10)Q0_C04	high alkalinity, high absorption, the dust size distribution shifted to coarse mode (C04)

SUMMARY

Mineral dust aerosols play an important role in atmospheric chemistry through photolysis and heterogeneous uptake. Both mechanisms strongly depend on the size and composition of mineral dust aerosols. Because of the complex nature of dust, chemistry modeling commonly relies on simplified assumptions about the properties of dust particles relevant to physiochemical processes**.** The goal of this thesis is to investigate the impact of size-resolved composition of dust aerosols on atmospheric photochemistry. The relative importance of dust characteristics in photolysis and heterogeneous loss and the relative roles of the two mechanisms on atmospheric photochemistry are investigated.

A new block of spectral aerosol optical properties was developed and incorporated into the tropospheric ultraviolet and visible radiation transfer code in order to calculate spectral actinic fluxes and photolysis rates, J-values. The Fuchs-Sutugin approximation was employed to compute mass transfer from gas to dust mineral species and heterogeneous loss rate, $k_{loss,j}$. The J-values and $k_{loss,j}$ were incorporated into a one-dimensional photochemistry model to simulate the diurnal cycle of a vertical profile of photochemical species. Several cases of dust loading were considered in the remote marine and polluted atmospheric conditions. A size-resolved mineralogical composition was constructed by selecting a range of the mass fraction of the three main mineral species, specifically considering iron oxide-containing clay minerals and alkalinity from carbonate-containing species. We used the spectral refractive indices from the Library of Atmospheric Aerosol Refractive Indices and the uptake coefficients of individual minerals and dust samples from recent laboratory studies. Several size distributions

reported from recent field experiments and/or used in prior modeling studies were considered.

This work demonstrates that differences in microphysical and chemical properties of mineral dust lead to the important changes in spectral optical properties, photolysis rates, and heterogeneous loss rates. It also shows that non-linear relationships of photochemical species with two mechanisms result in various changes in the photochemical oxidant fields and that the most important factor controlling the photochemistry field is the dust size distribution, followed by the amount of mineral species with high uptake coefficients and the amount of iron oxide-clay aggregates.

This work also demonstrates that accounting for regional differences in microphysical and chemical properties of mineral dust aerosols will improve the assessment of the impact of mineral dust on tropospheric photochemistry. In addition, it suggests that the size and composition of mineral dust particles will lead to a deeper understanding of the impact of mineral dust aerosols on the global climate system.

CHAPTER I

INTRODUCTION

Mineral dust aerosols play several important roles in the physical and chemical processes of the atmosphere. Between 200 and 5,000 metric tons of dust aerosols are emitted into the atmosphere every year [*Goudie*, 1983; Pye, 1987]. Mineral dust aerosols absorb and scatter in the UV, visible, and IR regions, leading to positive or negative direct radiative forcing, changing heating and cooling rates in the atmosphere, and altering photolysis [IPCC, 2007; *Sokolik et al.*, 2001]. Because of its peculiar chemical properties such as alkalinity and reducing capacity, mineral dust also interacts with gaseous species via heterogeneous chemistry on the surface of dust particles. This interaction leads to the loss of acidic gases and species [*Grassian*, 2001; *Usher et al.*, 2003]. In addition, mineral dust aerosols interact with clouds by serving as cloud condensation nuclei (CCN) after obtaining hygroscopic properties through sulfate coating on the dust surface [*Levin et al.*, 1996; *Fan et al.*, 2004] or through morphological changes in specific mineral species in high relative humidity [*Gibson et al.*, 2006; *Mashburn et al.*, 2006]. Long-range transported mineral dust can contribute to the biogeochemical cycle by carrying iron from the dust source region to the ocean [*Jickells et al.*, 2005; *Meskhidze et al.*, 2005]. Mineral dust aerosols can also carry the air pollutants such as carbonaceous, sulfate, or nitrate species [*Ooki and Uematsu*, 2005; *Mastumoto et al.*, 2006]. In addition, dust aerosols cause environmental problems such as visibility impairment when the size of dust aerosols is optically efficient, and health

problems such as respiratory diseases when particle size is fine enough to navigate through the air passages of the lungs [*Eschenbacher et al.*, 2000; *Levin et al.*, 2002].

In the chemistry of atmosphere, mineral dust aerosols perturb photochemical oxidant fields through photolysis and heterogeneous reactions [*Dentener et al.*, 1996; *He and Carmichael*, 1999; *Liao et al.*, 1999; *Bian and Zender*, 2003; *Martin et al.*, 2003; *Tang et al.*, 2004a; *Bauer et al.*, 2004]. Both mechanisms strongly depend on the size and composition of mineral dust aerosols. In order to estimate the impact of mineral dust aerosols, the incorporation of the size-resolved mineralogical composition of dust aerosols in chemistry and climate modeling was proposed [*Sokolik et al.*, 1998].

For the effects of mineral dust aerosols on photolysis rates, the photolysis rate constant, called the J-value, of a gaseous species, i is calculated as

$$J(i) = \int_{\lambda_{1,i}}^{\lambda_{2,i}} \sigma_i(\lambda, P, T)\Phi_i(\lambda, P, T)F(\lambda)d\lambda \qquad (1.1)$$

where $\lambda_{1,i}$ and $\lambda_{2,i}$ are the shortest and the longest photolytic wavelengths, respectively, at which the i*th* gaseous species absorbs light; σ_i (λ, P, T) is the absorption cross section of the i*th* species; Φ_i (λ, P, T) is the quantum yield for the photolysis of the i*th* species, and F(λ) is the actinic flux [*Seinfeld and Pandis*, 1998]. All three variables are a function of wavelength λ. The actinic flux F(λ), a spherical irradiance, reflects the atmospheric conditions such as clouds and aerosols as well as the position of sun. In the dust-laden atmosphere, the interactions between atmospheric radiation and mineral dust aerosols depend on the spectral optical properties of dust aerosols, which are functions of the size and composition of mineral dust aerosols.

Few previous studies showed the effects of the size and composition of mineral dust aerosols on J-values and atmospheric photochemistry. *Bian and Zender* [2003] showed that the differences in dust size distribution caused different vertical profiles for the J-values. However, past studies only used a simple probability distribution function or a dust transport model for the both calculation of J-values and heterogeneous loss rates, $k_{loss,j}$. For refractive indices, very limited data were available such as *Patterson* et al. [1977] and *Sokolik et al.* [1993]. Even though the role of iron oxide (hematite) contents in clay aggregates to light absorption was measured and modeled [*Alfaro et al.*, 2004; *Sokolik and Toon*, 1999], the data of varying amounts of iron oxides according to the dust source regions were recently available from experiments and modeling studies [*Lafon et al.*, 2006].

For the effects of mineral dust on the heterogeneous chemistry, the heterogeneous loss rates, $k_{loss,j}$ are calculated by

$$k_{loss.j} = \int_{r_1}^{r_2} k_{d,\,j}(r,\ \gamma) n(r) dr \qquad (1.2)$$

where $k_{loss,\,j}$ is the overall heterogeneous loss rate of the reactive gaseous species j on the particle; $k_{d,j}$ is the gas-to-particle diffusion rate constant of species j for a particle of radius r ($cm^3 s^{-1}$) and γ is uptake coefficient by aerosol particles; n(r) is the number size distribution between radii r and r+dr (cm^{-4}). Therefore, $k_{loss,j}$ strongly depends on the size and uptake coefficients.

Although heterogeneous reactions on dust particles result from the interaction between gas species and the surface materials, past studies selected and parameterized the uptake coefficients as one-value among those adopted from the uptake coefficients of

mineral species, mineral oxides, or authentic dust samples or those borrowed from the uptake coefficient of other types of aerosols such as sulfate, carbonaceous aerosols or water vapor [*Dentener et al.*, 1996; *Zhang et al.*, 1999; *De Reus et al.*, 2000; *Bian and Zender*, 2003; *Martin et al.*, 2003; *Liao et al.*, 2004; *Tang et al.*, 2004b; *Bauer et al.*, 2004]. Some studies calculated the effective uptake coefficient of dust based on uptake coefficients of several pure component oxides [*Usher et al.*, 2002]. However, the distinct abilities of dust aerosols to react with other atmospheric constituents were suggested to be based on the mineralogical components rather than chemical (elemental) components [*Usher et al.*, 2003; *Kruger et al.*, 2004]. In addition, laboratory studies have produced the broad understanding of heterogeneous reactions on mineral species such as clay minerals, quartz, and calcite, as well as their RH dependence or morphological changes [*Mashburn et al.*, 2006; *Usher et al.*, 2003 (reference there in); *Martin et al.*, 2001; *Krueger et al.*, 2003; *Laskin et al.*, 2005]. Therefore, the heterogeneous loss of gaseous species on the mineral dust surfaces can now be more vigorously examined.

However, past chemistry modeling studies did not consider mineral species essential to photolysis or heterogeneous reactions at the same time and they combined and compared the effects of mineral dusts through the two mechanisms. A simple assumption on size distribution and uniform composition of mineral dust aerosols in modeling photolysis and $k_{loss,j}$ cause inconsistency in modeling photochemistry [*Bian and Zender*, 2003; *Martin et al.*, 2003; *Tang et al.*, 2004a; *Bauer et al.*, 2004]. Although past studies recognized the importance of microphysical and chemical properties of mineral dust aerosols in the atmospheric photochemistry [*Bian and Zender*, 2003; *Tang et al.*, 2004b], none has investigated the effects of size-resolved mineralogical composition on

photochemistry and the interaction between the vertical profiles of J-values and $k_{loss,j}$ and the vertical distribution of photochemical oxidant.

In this thesis, we investigate the effects of size and compositions of mineral dust on the vertical profiles and diurnal variation of photolysis rates and heterogeneous loss rates independently, as well as on the combined effect of these two mechanisms. For this purpose, we introduce the dust mixtures appropriate needed to model each photochemical mechanism. Secondly, we incorporate each mechanism into a newly developed photochemistry model, DUST-CHEM. This model was specifically developed in order to be consistent with the assumptions on dust particles between photolysis and heterogeneous loss mechanisms and to closely examine the role of photolysis and heterogeneous loss in the impact of mineral dust on photochemistry. The DUST-CHEM has two important features. One is a new treatment of dust aerosols, considering them as a mixture of several key species. Another is the characterization of the impact of size-resolved dust composition on the atmospheric photochemistry through photolysis and heterogeneous reactions.

Several important issues must be addressed to build a dust mixture appropriate for this study. One is to determine the mineral species essential to atmospheric photochemistry. Another is to select the representative range of physiochemical characteristics of individual mineral species. The third is to select the mass fraction of such mineral species against total mass of dust aerosols. The mineralogical components of dust aerosols are assumed to be iron oxides in clay aggregates which absorb UV and visible light, carbonate-containing mineral species which exert alkalinity, and quartz. The selected microphysical and chemical information is provided for calculating the range of

the optical and chemical properties required for the calculation of J-values and $k_{loss,j}$. Such representative ranges of dust properties are pre-requisites for answering the scientific question of how the size and composition of mineral dust aerosols affect the atmospheric photochemistry through photolysis and heterogeneous loss.

A 1-D model is often used for the sensitivity test with respect to a specific physiochemical process such as radiative transfer, vertical convection, and the effects of surface emission or top fluxes. In contrast, a 3-D model can be used to simulate more realistic atmospheric phenomena such as long-range transport of pollutants or atmospheric circulation. In addition, the mass distribution of mineral dust aerosols has been quantitatively simulated considering their emission, transport, and deposition [*Ginoux et al.*, 2001; *Zender et. al.*, 2003; *Miller et al.*, 2006]. However, it is still necessary to quantify the atmospheric burden of mineral dust aerosols in space and time [*Darmenova*, 2006]. In addition, the information on the size-resolved mineralogical composition of the parent soil is not available [*Sokolik*, 1999] and the quantification of atmospheric burden of mineral species of dust aerosols is challengeable through either modeling or observation. Because of such complexity, it is difficult to treat the size-resolved mineralogical mixture of dust particles in the 3-D transport model. Hence, this thesis uses a 1-D photochemistry model to focus on the impact of size-resolved mineralogical mixture of dust aerosols on atmospheric photochemistry through J-values and $k_{loss,j}$.

In this thesis, the vertical profiles of J-values and $k_{loss,j}$ are incorporated into the 1-D photochemistry model. The chemistry module in DUST-CHEM includes the gaseous reaction rate constants of NO_x-HO_x-CH_4-sulfur chemistry, and the J-values and $k_{loss,j}$

reflecting the impact of mineral dust aerosols. While gaseous reaction rates are "constant" with those regularly published by NASA/JPL and IUPAC (the International Union of Pure and Applied Chemistry), the J-values and $k_{loss,j}$ are "variables" that depend on the dust load conditions. The J-values and $k_{loss,j}$ are incorporated into the Sparse-Matrix-Vectorized (SMV) gear code according to sun position and altitude under the dust-laden conditions. Based on the interpretation of the results from the DUST-CHEM model, this thesis focuses on investigating the sensitivity of photochemical species to the dust size distribution, the amounts of hematite in iron oxide-clay aggregates, and gaseous uptakes. For several types of dust mixtures that have contrasting physiochemical properties of dust aerosols, the contribution of photolysis and heterogeneous loss or both mechanisms to atmospheric photochemistry is examined.

Specific goals of this thesis include the investigation of the impact of the size-resolved mineralogical composition of dust aerosols on atmospheric photochemistry, determination of the relative importance of dust characteristics in photolysis and heterogeneous loss, and characterization of the relative roles of these two mechanisms on atmospheric photochemistry. While pursuing these goals, this study will address the following three scientific questions:

1. How do the size and composition of mineral dust (specifically, Asian dust) affect the spectral optical properties in the UV and visible regions, and what are the implications for the spectral actinic fluxes and photolysis rates under representative aerosol-laden conditions in the clean and polluted marine environments?

2. How do the size and mineralogical composition of dust affect the heterogeneous loss rates ($\boldsymbol{k_{loss,\ j}}$) of gaseous species on particle surfaces, and what are the implications for the tropospheric photochemistry?
3. How do the vertical profiles of J-values and $k_{loss,j}$ perturbed by mineral dust aerosols affect the vertical distribution of photochemical species? How much can such tendency vary with the size-resolved mineralogical mixtures of dust particles? What are the importance of dust characteristics and the relative role of these two mechanisms to atmospheric photochemistry?

In order to answer these questions, specific objectives are accomplished in each chapter. Chapter II describes a newly-developed aerosol optical module which is incorporated into the NCAR TUV radiative transfer code. The microphysical and chemical properties of the main aerosol types and loading conditions are selected based on data from recent field measurements and laboratory and modeling studies. This chapter also analyzes the behavior of the spectral optical properties of aerosols and their effects on the spectral actinic flux and photolysis rate, focusing on the impact of dust.

Chapter III addresses the heterogeneous chemistry on dust particle surfaces. The chapter starts by introducing the size-resolved mineralogical mixtures of dust particles constructed by selecting a range of the mass fraction of the three main mineral species. Heterogeneous loss rates ($k_{loss,j}$) are calculated using the *Fuchs-Sutugin* approximation in the transition regime. Recent data on the uptake coefficients of individual minerals and authentic dust and several dust size distributions reported from field and laboratory experiments are used.

Chapter IV introduces DUST-CHEM which is developed to incorporate the vertical profiles and diurnal variation of J-values and $k_{loss,j}$ into the 1-D photochemistry model. Dust aerosols are considered as an external mixture of main mineral species such as iron oxide-clay aggregates, calcite, and quartz. The size distributions, ranges of the amount of iron oxide in clay minerals, and the amount of carbonate compounds are the same as those used in photolysis and heterogeneous studies (Chapters 2 and 3). The chapter also discussed the selection of aerosol and gas phase species and dust loading scenarios.

Chapter V summarizes the findings and conclusions.

CHAPTER II

THE EFFECT OF MINERAL DUST AEROSOLS ON THE PHOTOLYSIS RATES IN THE CLEAN AND POLLUTED MARINE ENVIRONMENTS

2.1 Introduction

Aerosol particles scatter, and some can absorb UV and visible radiation, altering the actinic flux and, hence, photolysis rates. The radiative processes involving dust particles strongly depend on their physiochemical properties, especially size and composition. The focus of this chapter is to investigate how mineral dust can affect the photolysis rates of gaseous species that are of importance to atmospheric chemistry.

The first-order photolysis rate constant, called the J-value, of a gaseous species, i, is calculated as

$$J(i) = \int_{\lambda_{1,i}}^{\lambda_{2,i}} \sigma_i(\lambda, P, T)\Phi_i(\lambda, P, T)F(\lambda)d\lambda, \qquad (2.1)$$

where $\lambda_{1,i}$ and $\lambda_{2,i}$ are the shortest and the longest photolytic wavelengths, respectively, at which the i*th* gaseous species absorbs light; σ_i (λ, P, T) is the absorption cross section of the i*th* species; Φ_i (λ, P, T) is the quantum yield for the photolysis of the i*th* species, and F(λ) is the actinic flux [*Seinfeld and Pandis*, 1998]. The absorption cross section and quantum yield are functions of temperature T and pressure P as well as wavelength λ. Actinic flux F(λ), a spherical irradiance, depends on atmospheric conditions, including the position of the sun and the presence of clouds and aerosols. Under aerosol- and cloud-free conditions, the spectral behavior of actinic flux is governed by extraterrestrial solar radiation and molecular (Rayleigh) scattering and absorption. In an aerosol-laden atmosphere, interactions of aerosol particles with atmospheric radiation depend on their spectral optical characteristics such as optical depth, $\tau(\lambda)$, single scattering albedo, $\omega_0(\lambda)$,

and asymmetry parameter, g(λ). Photolysis rates are controlled by the actinic flux available in the photolytic wavelength range, which varies among gases. For instance, NO_2 photo-dissociates at 210-420 nm, and $O_3(O^3P)$ photo-dissociates at 210-365 nm and 405-730 nm. Thus to adequately quantify their effects on photolysis rates, the optical properties of aerosols are required in the spectral range from UV to visible.

Some past studies have suggested that strongly absorbing aerosols cause a decrease in photolysis rates, whereas non-absorbing aerosols increase them compared to clear-sky conditions. In urban environments, absorption of UV and visible radiation is attributed mainly to the presence of black carbon (BC) and some organics, whereas in and downwind of arid and semi-arid regions mineral dust is a main absorbing species [*Jacobson*, 1998; *Dickerson et al.*, 1997; *Liao et al.*, 1999; *He and Carmichael*, 1999 (hereafter *HC*1999)]. However, past studies dealing with dust have relied on a number of oversimplified assumptions, especially about the size and composition of dust particles. The recent data from ACE-Asia along with new measurements of the content of iron oxides in dust aggregates [e.g., *Lafon et al*., 2006] provide an opportunity to re-examine the effect of dust on J-values under more realistic assumptions.

The particle size distribution of dust is often approximated with one or a few lognormal functions from observation or modeling [*Patterson and Gillette*, 1977; *d'Almeida* 1987 (hereafter *D*1987); *d'Almeida et al.*, 1991 (hereafter *D*1991); *Hess et al.*, 1998 (hereafter *H*1998); *Alfaro et al.*, 1998; *Dubovik et al.*, 2002; *Reid et al.*, 2003; *Zhang et al.*, 2003; *Clarke et al.*, 2004 (hereafter *C*2004)]. Despite the differing size distributions reported for dust, previous studies of photolysis rates relied only on a particular aerosol model [*Liao et al.* ,1999; 2003; *Bian et al*., 2003]. *Bian and Zender* [2003] pointed out that the selection of dust size distributions might cause the differences in $J[O_3(O^1D)]$ and $J[NO_2]$ of 10-25%, comparing their results from the DEAD model with those of *Martin et al.* [2002] which used another dust size representation in their transport model. Moreover, size distributions considered in the above modeling studies

differ from either those retrieved from AERONET [*Dubovik et al.*, 2002] or those measured during the ACE-Asia field experiment [*C*2004]. Therefore the effect of dust size distribution on the optical properties of mineral dust, actinic fluxes, and J-values must be re-examined taking into account recent data.

Another important issue is the selection of spectral refractive indices. Past studies mainly relied on the data of *Patterson et al.* [1977], which were measured for bulk samples of unknown composition of far-traveled Saharan dust. The imaginary part of the *Patterson's* refractive index is very high (0.025 at 300 nm and 0.0038 between 600 and 700 nm). Thus mineral dust was treated as a strong absorbing aerosol. Both *Martin et al.* [2002, 2003] and *Bian and Zender* [2003] used the Patterson's refractive index. *Liao et al.* [1999, 2003] used the wavelength-dependent refractive indices of dust samples from Tadzhikistan, Central Asia, which *Sokolik et al.* [1993] reported as 0.01 at 300 nm and about 0.005 at 700 nm and which was lower than *Patterson's* refractive indices. Alternatively, it has been demonstrated that accounting for the mineralogical composition provides a better approach for modeling optical properties of dust, given that dust is a mixture of various individual minerals and their aggregates [*Sokolik and Toon*, 1999]. In particular, iron oxide-clay aggregates are the key species controlling the ability of dust to absorb sunlight. No studies so far have examined the effect of the varying iron oxide amount in the aggregates on actinic fluxes and J-values.

Some studies have used the aerosol packages such the *d'Almeida* models [*D*1991] and Optical Package of Aerosols and Clouds (OPAC) [*H*1998] for both regional and global modeling, despite the fact that these models were built on the limited data for Saharan dust. For instance, *Tang et al*. [2003] concluded that Asian aerosol would exert a strong effect on O_3 production during TRACE-P, and *Tang et al.*[2004a] found that Asian dust through photolysis could decrease OH levels by 20% near the surface during ACE-Asia. However, *Tang et al.* calculated the photolysis rates not by using size distribution

and composition determined for Asian dust but by employing OPAC models adjusted to mass concentrations measured from the field experiments.

ACE-Asia measurements confirmed that, downwind of their sources, dust particles can be internally or externally mixed with other aerosols [*Arimoto et al*., 2006]. Both the abundance of species and their mixing state could affect the spectral optical properties. For instance, during ACE-Asia the single scattering albedo in the presence of dust and pollution (0.84 to 0.9) was lower than that in the dusty condition (0.93 to 0.98) [*C*2004; *Kim et al.*, 2004; C*onant et al.*, 2003]. Those values are higher than $\omega_o = 0.88$ of OPAC at 550 nm. Thus it is important to examine the effect of mineral dust on photolysis rates by taking into account not only mineralogical composition but also the presence of other aerosols and how they mix with dust, especially mixing with BC. This issue also was not addressed by previous studies.

The goal of the present study is to investigate how the size and composition of mineral dust (especially Asian dust) affect the spectral optical properties in the UV and visible and what the implications for the spectral actinic fluxes and photolysis rates under representative aerosol-laden conditions are. Our approach is introduced in section 2.2. Section 2.3 describes the selection of the microphysical and chemical properties of the main aerosol types and loading conditions. In section 2.4 we analyze the behavior of the spectral optical properties of aerosols, considering the mixing state of dust, BC, and other aerosol species. Section 2.5 presents our modeling results of spectral actinic fluxes and photolysis rates, and Section 2.6 summarizes the major findings of this chapter.

2.2 Approach

We use a tropospheric ultraviolet-visible (TUV) one-dimensional radiative transfer code (version 4.2) developed at the National Center for Atmospheric Research (NCAR) [*Madronich*, 1989; http://cprm.acd.ucar.edu/ Models/ TUV]. The TUV code

computes the actinic flux taking into account gaseous absorption by O_3, NO_2, and SO_2 as well as molecular (Rayleigh) scattering. TUV version 4.2 includes 115 photo-dissociation reactions with the most recent data on the absorption cross sections and quantum yields based on regular publications of the evaluation panels for kinetic data from the NASA/Jet Propulsion Laboratory (JPL) and the International Union of Pure and Applied Chemistry (IUPAC). The optical depth due to Rayleigh scattering τ_R is calculated using the Nicolet's Rayleigh cross-section and the U.S. Standard Atmosphere 1976. When τ_R calculations resulting from TUV were compared with those from the approach discussed by *Bucholtz* [1995], differences were negligibly small.

The TUV model was set up for 17 April 2001 for the northwestern Pacific Ocean (132ºE and 34ºN) to simulate a diurnal sun cycle representative of the ACE-Asia time period. The radiative transfer model was run in a two-stream approximation, which is of sufficient accuracy for the purpose of this study. TUV calculations were performed over the wavelength range from 210 to 735 nm with a spectral resolution of 5 nm. The surface albedo of 0.05 was selected, assuming that the spectral variation of the ocean surface albedo is small, and the constant value would be a good approximation. Our analysis focuses on the 13 photo-dissociation reactions important in the tropospheric photochemical oxidant system shown in Table 2.1. Considered reactions were classified into three groups that will be discussed in section 2.5.

We have modified TUV by incorporating a new block that calculates the spectral optical characteristics of aerosols developed in this study. The Mie code was used to compute the spectral extinction and scattering coefficients, scattering phase function, and asymmetry parameter for a given spectral refractive index of aerosol particles and their particle size distribution. The spectral refractive indices were taken from the Library of Atmospheric Aerosol Refractive Indices (LAARI) that we have been developing over the years [e.g., *Sokolik and Toon*, 1999]. Depending on aerosol loading and mixing state,

effective optical properties of each atmospheric layer are calculated by combining the spectral optical properties of atmospheric gases and aerosols.

Table 2.1: Main Photolysis Reactions Considered in This Study

	Photolysis Reaction	Photolytic Wavelength (nm)	Group
J1	$O_3 \rightarrow O_2 + O(^3P)$	210 - 365, 405 – 730	III
J2	$O_3 \rightarrow O_2 + O(^1D)$	210 – 340	I
J3	$NO_2 \rightarrow NO + O$	210 – 420	II
J4	$NO_3 \rightarrow NO_2 + O(^3P)$	400 – 635	III
J5	$NO_3 \rightarrow NO + O_2$	585 – 635	III
J6	$HONO \rightarrow OH + NO$	310 - 395	II
J7	$N_2O_5 \rightarrow NO_3 + NO_2$	225 - 380	I
J8	$HNO_3 \rightarrow OH + NO_2$	210 - 350	I
J9	$HO_2NO_2 \rightarrow HO_2 + NO_2$	210 - 330	I
J10	$H_2O_2 \rightarrow OH + OH$	210 - 350	I
J11	$CH_3OOH \rightarrow CH_3O + OH$	210 - 325	I
J12	$CH_2O \rightarrow H + HCO$	240 - 340	I
J13	$CH_2O \rightarrow H_2 + CO$	240 - 355	I

2.3 Analysis and Selection of Microphysical and Chemical Characteristics of Aerosols for Optical Modeling

We used new data from the ACE-Asia experiment and laboratory dust measurements to define the main aerosol types and their properties, especially those of dust aerosols, as well as to constrain the representative scenarios of aerosol-laden conditions. Five types of atmospheric aerosol species are considered: water-soluble aerosols (WSAs) consisting mainly of sulfates and nitrates, sea-salt, black carbon (BC), organic carbon (OC), and mineral dust.

The aerosol size distribution is commonly approximated by a log-normal function or by several log-normal functions in the case of multiple size modes as

$$\frac{dN(r)}{d(\log r)} = \sum_{i=1}^{n} \frac{N_i}{\sqrt{2\pi}\log\sigma_i} \exp\left(-\frac{(\log r - \log r_{g,i})^2}{2(\log\sigma_i)^2}\right), \quad (2.2)$$

where N(r) is the aerosol particle number concentration, *i* is the size mode, N_i is the number concentration of the i*th* size mode, and $r_{g,i}$ and σ_i are the median radius and geometric standard deviation of the i*th* size mode, respectively. The mass concentration can be calculated from the number concentration by taking the third moment of the log-normal distribution function

$$MW_{tot} = \int_0^\infty \rho \frac{4}{3}\pi r^3 \frac{dN}{dr} dr, \quad (2.3)$$

where MW_{tot} is the total mass concentration, and ρ is the particle density. It has been suggested that a size cutoff be applied, that is, to perform the integration from some minimum radius to maximum radius. Here we use a cutoff (maximum) radius of 7.5 μm following the OPAC models.

2.3.1 Non-Absorbing Aerosols

Sea-salt and WSAs are the main aerosol constituents in the clean marine atmosphere. We assume that sea-salt with the concentration of 68.9 μg/m^3 is present only in the marine boundary layer (MBL) [*D*1991]. The concentration of WSAs in the MBL is assumed to be 3.0 μg/m^3, and it decreases exponentially with altitude [*H*1998]. In the polluted atmosphere, WSAs were determined by summing up the concentrations of sulfate, ammonium, and nitrate ions using the ACE-Asia data from *Bahreini et al.* [2003]. Determined mass concentrations of WSAs varied from about 4.68 to 9.41μg/m^3. We used these values as the concentration of WSAs in the MBL to represent low and high polluted conditions.

Table 2.2: The Microphysical Properties of Sea-salt, Water-soluble, Organic Carbon, and Black Carbon Based on *d'Almeida et al.* [1991], except [c:] *Clarke et al.* [2004]

Chemical component (Size mode)	r_g (μm) Median radius	σ_g Standard deviation	ρ Density (g/m^3)	M* ($\mu g\ m^{-3}$)/ (cm^{-3})
Sea-salt, NaCl	0.05(0% RH)	2.03	2.17	1.099E-2
(nuclei)	0.098(70% RH)		1.23	4.628E-2
Sea-salt, NaCl	0.4(0% RH)	2.03	2.17	5.506E+0
(accumulation)	0.716(70% RH)		1.23	1.595E+1
Sea-salt, NaCl	3.30(0% RH)	2.03	2.17	5.290E+2
(coarse)	5.908(70% RH)		1.23	3.748E+2
Water-soluble, $(NH_4)_2SO_4$	0.0285(0% RH)	2.239	1.77	3.248E-3
(nuclei)	0.0309(50% RH)		1.39	3.196E-3
	0.0314(70% RH)		1.30	3.137E-3
Organic Carbon (nuclei)	0.0118	2.0	1.20	7.137E-5
Black Carbon (nuclei)	0.0118	2.0	1.25	7.472E-5
Organic Carbon (nuclei)	0.071[c]	1.59[c]	1.20	4.740E-3
Black Carbon (nuclei)	0.071[c]	1.59[c]	1.25	4.930E-3

Note: M* is the ratio of mass and particle number size concentrations calculated for a given size distribution using cutoff radius of 7.5 μm.

The size distributions of sea-salt and WSAs were adopted from *D*1991 (as shown in Table 2.2). Because these aerosols are hygroscopic, their particle sizes and refractive indices vary with relative humidity, RH. In this study we consider the lowest three vertical layers of the atmosphere in which RH was set to 70%, 50%, and 0%, based on ACE-Asia observations. For these RH values, the refractive indices of aqueous aerosols were calculated by using the molar refraction approach [*Stelson*, 1990] and spectral refractive indices of individual dry salts and water, which were taken from LAARI. Ammonium sulfate and sodium chloride are assumed to be representative of WSAs and

sea-salt, respectively. In turn, organic carbon (OC) is considered as dry and non-absorbing in this study, even though some OC is soluble in water and can absorb UV radiation. The size distribution of OC in *D*1991 has the same parameters as those of BC.

2.3.2 Black Carbon

The imaginary part of the refractive index of BC in the UV-visible can be as high as 0.8 [*Bond and Bergstrom*, 2006]. Thus even a relatively small amount of BC might strongly affect the overall absorption of the aerosol mixtures. In general, the ratio between the mass concentration of OC (or total carbon) and BC varies depending on the sources. We used measurements from ACE-Asia [*Mader et al.*, 2002] to constrain OC and BC concentrations for our study. Because measurements were carried out during flights that were intentionally conducted in the dust (and/or pollution) layers and relatively clean layers, obtained concentrations of BC and OC are likely to represent upper and lower values rather than a mean value. Therefore we introduce high and low pollution cases as having BC concentrations of 0.2 and 1.8 $\mu g/m^3$, respectively. OC concentrations for low and high pollution cases are 0.58 and 29.0 $\mu g/m^3$.

BC particles are assumed to be dry and hydrophobic. The BC size distribution of *D*1991 has one size mode defined by $r_g = 0.012$ μm and $\sigma_g = 2.0$ (see Table 2.2). During ACE-Asia, *C*2004 measured the size distribution of BC with $r_g = 0.071$ μm and $\sigma_g = 1.59$. The median radius of the latter size distribution is larger than that of *D*1991 by about a factor of six. Our calculations show that using the *Clarke* size distribution for BC leads to large extinction coefficients, resulting in an unrealistically large optical depth for the considered BC concentrations. Therefore we chose to use the *d'Almeida* size distribution for BC in this study. In the case of an internal mixture of dust and BC, the parameters of the size distribution of the mixture were calculated with a well-mixed sphere approach following *Lesins et al.* [2002] as described in section 4.1.

2.3.3 Mineral Dust

We consider three different cases of the mineralogical composition of dust aggregates: strong absorbing dust (H10) composed of 90% kaolinite and 10% hematite, moderate absorbing dust (H5) composed of 95% kaolinite and 5% hematite, and low absorbing dust (H1) composed of 99% kaolinite and 1% hematite (by volume fraction). Although the data of iron oxides in aggregates are still limited, it has been suggested that Asian dust falls more likely between H1 and H5 cases [*Lafon et al.*, 2006]. The spectral refractive indices of the aggregates were calculated by applying the effective medium approximation to the refractive indices of individual components following *Sokolik and Toon* [1999]. We assume that both the refractive index and the sizes of dust particles are not sensitive to RH.

The above compositional cases were considered in a combination with several dust particle size distributions that either were reported from recent measurements or were used for actinic flux modeling by previous studies. Table 2.3 compares these size distributions in terms of their individual size modes delineating the similarities and differences. The C04 denotes the size distribution which was measured during ACE-Asia and fitted with three size modes [*C*2004]. The third mode of C04, which was taken from *Alfaro et al.* [1998], has a large median radius r_g = 4.33 μm similar to the third mode of the size distribution from *d'Almeida et al.* [1987] (hereafter D87). Unlike C04 and D87 which both have larger mass fractions in their coarse modes, O98 has about 76% of the total mass in the accumulation mode (r_g = 0.39 μm). The L91 is a long-range transported dust from *d'Almeida et al.* [1991], and B02 stands for dust size distribution retrieved from the NASA AERONET site in Bahrain [*Dubovik et al.*, 2002]. The C04 was measured in East Asia, whereas the D87, O98, and L91 size distributions were derived for Saharan dust. Appendix D includes the number, area, and mass size distributions.

Table 2.3: The Median Radius, r_g (μm), Geometric Standard Deviation, σ_g, and the Mass Fraction of Dust Size Distribution Models

Dust Size Distribution / Reference	Size mode	Mode1	Mode2	Mode3	Mode4	Mode5
C04	r_g (μm)		0.345	0.885		4.335
Clarke et al. [2004]	σ_g		1.46	1.85		1.50
	Mass fraction		1.8%	69.4%		28.8%
D87	r_g (μm)	0.08		0.7		4.99
D'Almeida [1987]	σ_g	2.10		1.90		1.60
	Mass fraction	1.0%		95.3%		3.7%
O98	r_g (μm)	0.07	0.39		1.9	
Hess et al. [1998]	σ_g	1.95	2.00		2.15	
	Mass fraction	3.4%	76.1%		20.5%	
L91	r_g (μm)			0.5		
D'Almeida et al. [1991]	σ_g			2.20		
	Mass fraction			100%		
B02	r_g (μm)	0.088		0.832		
Dubovik et al. [2002]	σ_g	1.52		1.84		
	Mass fraction	9.1%		90.9%		

To illustrate the effect of dust size distributions, Figure 2.1 shows the extinction coefficient, k_{ext}, single scattering albedo, ω_0, and absorption coefficient, k_{abs}, calculated for dust aggregates with the mineralogical composition of 99% kaolinite and 1% hematite (H1 dust) for a dust concentration of 1500 μg/m^3. Although C04, L91, D87, and O98 give

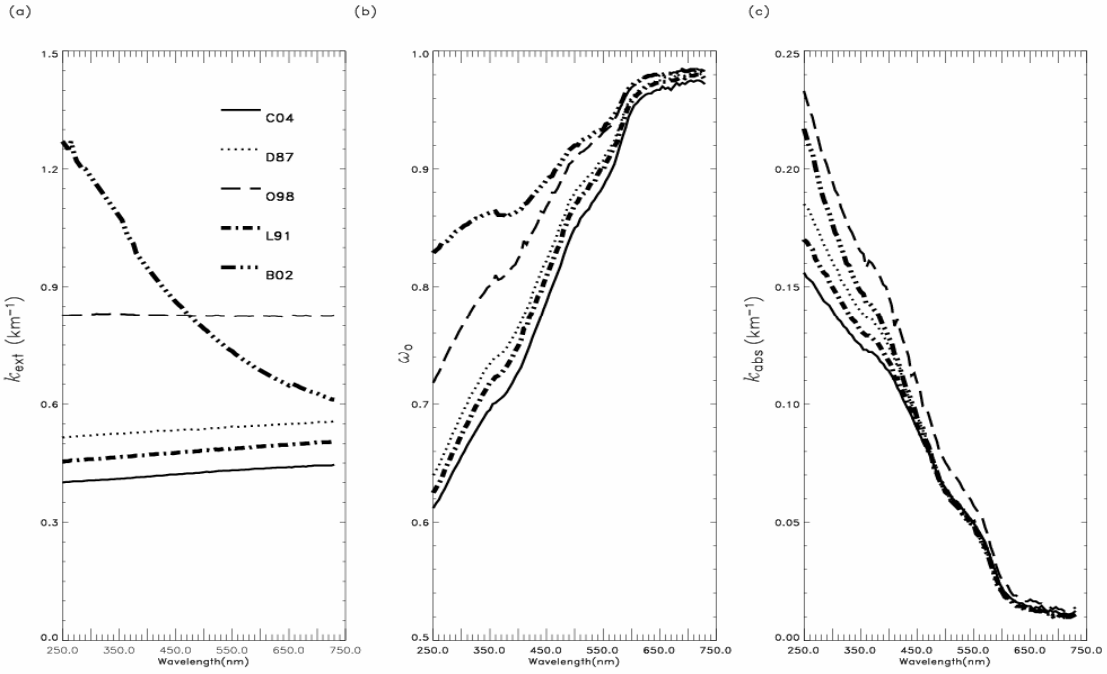

Figure 2.1: (a) The extinction coefficient, k_{ext}, (b) the single scattering albedo, ω_0, and (c) the absorption coefficient, k_{abs}, calculated for five dust size distributions and H1 dust.

similar neutral spectral behavior of k_{ext}, values of k_{ext} are quite different, especially those of O98. In contrast, the B02 size distribution results in the strong wavelength dependence of k_{ext} with the largest values in the UV. This is because B02 has a large mass fraction in the smallest size mode (i.e., it is shifted to the fine size mode) compared to the others. All size distributions give the lowest values of ω_0 in the UV, and ω_0 increases as wavelength increases. The B02 and O98 have the largest values of ω_0 which exhibit the weakest dependence on wavelength. The k_{abs} values of B02 and O98 cases are larger than those of the C04, L91, and D87 cases. In the following analysis we use the C04 size distribution as a reference case to calculate the optical properties of Asian dust, whereas other dust size distributions are used to carry out the sensitivity study to delineate the effects of dust size spectra on photolysis rates.

We also used the ACE-Asia data to constrain the concentration of dust particles. The dust mass concentrations were reported in the range from 30 to 5000 μg/m^3 [e.g., *Alfaro et al.*, 2003; *C*2004]. However, it has been well recognized that dust particles are particularly difficult to measure, especially from an aircraft [e.g., *Reid et al*., 2003]. Another way to infer dust loading is to use measurements of the aerosol optical depth τ. During ACE-Asia, τ measured with a sun photometer at 550 nm was reported to be 1.6-1.8 under heavy dust loading [*Alfaro et al*., 2003], 1.0-1.2 under moderate dust loading, and 0.15 under clean maritime conditions [*Bergstrom et al.*, 2004; *Sano et al.*, 2003]. The latter is in the upper limit of values reported for the clean maritime atmosphere [*Smirnov et al.*, 2003]. Performing Mie calculations with the C04 size distribution, we found that the total dust mass concentration should be about 5000 μg/m^3, 3000 μg/m^3, and 1000 μg/m^3 for heavy, moderate, and light dust loadings, respectively, to match the observations. These values were used in our calculations and were equally distributed between two dust layers located between 1 km and 3 km, that is to say that, for instance, in case of moderate dust loading, the dust mass concentration in a 1 km-thick layer is 1500 μg/m^3. Although these values are in agreement with *Alfaro et al.* [*2003*], they are somewhat higher than values reported from aircraft measurements during ACE-Asia. For instance, the highest concentration reported by *C*2004 was 1000 μg/m^3 during research flight 13. A number of factors could have been responsible for the lower values of mass concentrations observed from the aircraft. More than 50% of dust particles may have been lost during aircraft sampling and another 50% from the capacity of the instruments, which only measured the particles with an aerodynamic diameter of less than 9 μm, and by about 50% underestimation of real concentration from the generic optical particle

counter problem on measuring dust particles [*Reid et al*., 2003]. Also, research flight 13 did not measure a heavy dust storm during ACE-Asia. Therefore we believe that our values adequately represent the heavy, moderate, and light dust loadings.

2.3.4 Selection of Aerosol Loading Scenarios

Based on aircraft measurements during ACE-Asia, *Wang et al.* [2002] introduced three different layers below 4 km: the MBL (from 0 to 1 km), the transition layer (1 to 2 km), and the free troposphere layer (above 2 km). We adopted this structure to set up the vertical distribution of aerosol species for our study. Table 2.4 shows the considered cases of aerosol loadings: a clean maritime atmosphere (case 1), low (case 2) or high (case 3) pollution over a low polluted MBL, moderate (case 4) or heavy (case 5) dust above a clean MBL, moderate dust over a high polluted MBL (case 6), and dust mixed with BC over a low polluted MBL (case 7). The sensitivity of the optical properties and J-values to the size distribution and mineralogical composition were investigated in detail in case 4, while the sensitivity to the mixture of dust and BC were examined in the condition of moderate dust and low or high pollution cases over a low polluted MBL (case 7) by varying the mineralogical composition, BC concentration, and dust and BC mixing state.

Table 2.4: Aerosol Loading Scenarios

Vertical Layer (km)	Clean marine	Low pollution	High pollution over low polluted MBL	Moderate dust outbreak	Heavy dust outbreak	Moderate dust outbreak over high polluted MBL	Moderate dust mixed with BC and pollution over low polluted MBL
	Case1	Case2	Case3	Case4	Case5	Case6	Case7
2 -3	CLEAN	LOWPOLL	HIGHPOLL	DUST(M)	DUST(H)	DUST(M)	DUST/BC/POLL
1- 2	CLEAN	LOWPOLL	HIGHPOLL	DUST(M)	DUST(H)	DUST(M)	DUST/BC/POLL
0 – 1	CLEAN	LOWPOLL	LOWPOLL	CLEAN	CLEAN	HIGHPOLL	LOWPOLL

M and H denote moderate and high dust loadings, respectively.

2.4 Analysis of Calculated Spectral Optical Properties

Given that spectral actinic fluxes in the atmosphere are ultimately controlled by both gases and aerosols, we focus on the analysis of the effective spectral optical properties. Also, because of strong absorption and scattering by gases whose spectral features are well known in the UV-visible, analyzing the effective optical properties helps to determine whether the differences in spectral aerosol characteristics are important or not.

Figure 2.2 shows the effective optical depth, τ_{eff}, effective single scattering albedo, $\omega_{0,eff}$, and the effective absorption optical depth, $\tau_{abs,eff}$, calculated in a layer between 1 km and 2 km for differing aerosol loading cases (see Table 2.4). In all cases, τ_{eff} is larger in the UV than in the visible mainly due to strong gaseous absorption and Rayleigh scattering. In the presence of dust, τ_{eff} is much larger compared to the dust-free cases. The τ_{eff} in the high polluted atmosphere (case 3) is larger than in the low polluted (case 2) or clean marine atmosphere (case 1) because of higher concentrations of WSAs, OC, and BC.

The various differences in $\omega_{0,eff}$ are apparent in Figure 2.2, especially in the spectral behavior. Because of the strong impact of gaseous absorption, values of $\omega_{0,eff}$ are the lowest in the UV. As expected in the presence of non-absorbing aerosols, $\omega_{0,eff}$ reaches 1 outside the region of gaseous absorption. The difference in the concentration of BC between low and high pollution (cases 2 and 3, respectively) results in noticeable differences in $\omega_{0,eff}$, although in both instances $\omega_{0,eff}$ values decrease with increasing wavelength. In contrast, $\omega_{0,eff}$ increases as wavelength increases in the presence of dust. An increase in the dust concentration has the negligible effect on $\omega_{0,eff}$ in the dust layer.

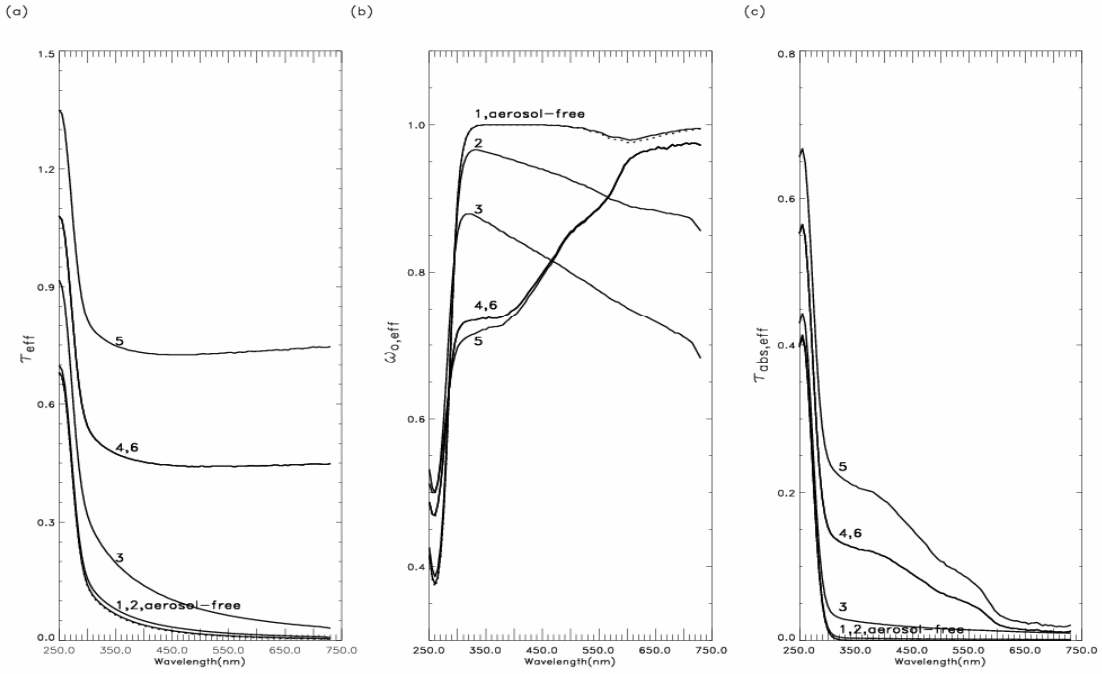

Figure 2.2: (a) The effective optical depth, τ_{eff}, (b) the effective single scattering albedo, $\omega_{0,eff}$, and (c) the effective optical depth, $\tau_{abs,eff}$, calculated in a 1- 2 km layer for considered aerosol loading scenarios denoted by case numbers (see Table 2.4). The H1 dust and the C04 size distribution were used.

Figure 2.3 shows τ_{eff}, $\omega_{0,eff}$, and $\tau_{abs,eff}$ in a 1-2 km layer with moderate dust loading calculated for five dust size distributions for the same dust composition (H1) as in Figure 2.2. The τ_{eff}, $\omega_{0,eff}$, and $\tau_{abs,eff}$ for the "dust-like" model adopted from *D*1991 are also shown to facilitate the comparison with previous studies. The "dust-like" model has a single size mode with a median radius of 0.471 μm and a standard deviation of 2.512 and the refractive indices of *Patterson et al.* [1977]. Although the spectral dependence of τ_{eff} is rather similar between the dust models, except B02, values of τ_{eff} calculated with C04, D87, and L91 are smaller than those calculated with O98, reflecting the differences in the extinction coefficient of dust shown in Figure 2.1(a). The "dust-

like" model gives the highest τ_{eff} and $\tau_{abs,eff}$ but the lowest $\omega_{0,eff}$ relative to all others over the entire photolytic region.

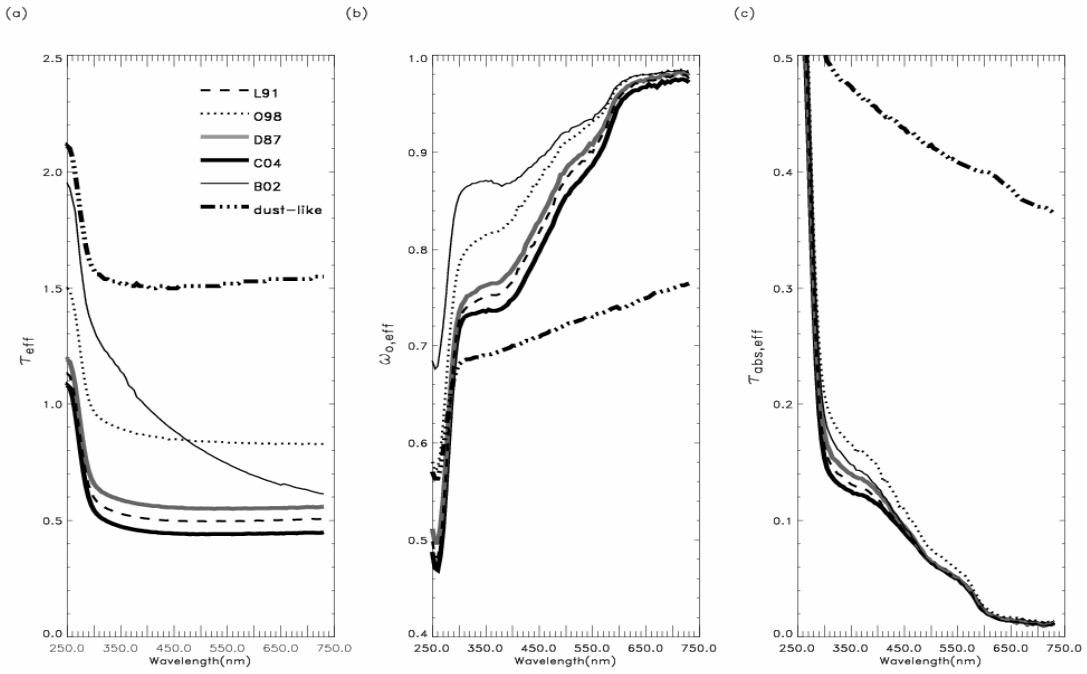

Figure 2.3: (a) The effective optical depth, τ_{eff}, (b) the effective single scattering albedo, $\omega_{0,eff}$, and (c) the effective absorption optical depth, $\tau_{abs,eff}$ calculated for five dust size distributions for a layer between 1 and 2 km in the condition of the moderate dust loading and H1 composition. "Dust-like" is from *d'Almeida et al.* [1991].

The effect of differing composition is shown in Figure 2.4. This figure presents τ_{eff}, $\omega_{0,eff}$, and $\tau_{abs,eff}$ computed for the H1, H5, and H10 dust aggregates. The dust size distribution is the same as in Figure 2.2. It is apparent that τ_{eff} is little affected by the changes in the amount of iron oxides in dust aggregates. However, these changes strongly affect not only values of $\omega_{0,eff}$ but also its dependence on the wavelength. Overall, Figures 2.2 - 2.4 show that the spectral behaviors of τ_{eff} and $\omega_{0,eff}$ have various features depending on the properties of dust itself as well as other aerosols. The changes in size distribution

and the amount of iron oxides result in changes of the optical characteristics that vary as a function of wavelength. Thus changes in dust properties are likely to cause the differing impact on J-values of gases with different photolytic wavelength ranges. Quantitative assessment of this impact will be addressed in section 2.5.

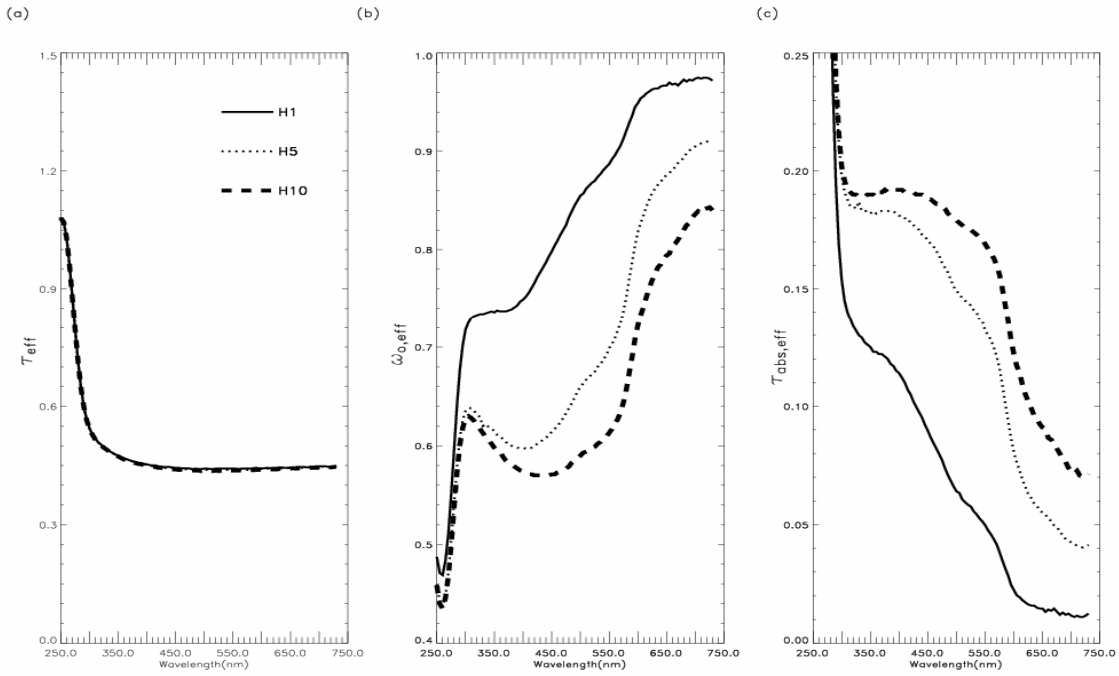

Figure 2.4: (a) The effective optical depth, τ_{eff}, (b) the effective single scattering albedo, $\omega_{0,eff}$, and (c) the effective absorption optical depth, $\tau_{abs,eff}$ calculated for three different mineralogical compositions, C04 size distribution and moderate dust loading in a 1-2 km layer.

To the extent possible, we validated the computed spectral optical characteristics against measurements. *Alfaro et al.* [2003] measured the Angstrom exponent (Å) of 0.19-0.6 at wavelengths between 441 nm and 670 nm and aerosol optical depth ranging from 1.2-1.6 at 441 nm using a CIMEL sun photometer in Zhenbeitai, China, during a dust storm. *Sano* [2003] measured a similar Å of 0.2-0.6 between 443 nm and 865 nm in the East China Sea in a dust event during ACE-Asia. In our calculations using several dust

size distributions in the moderate dust loading, Å was estimated to be from -0.1 to 0.68 at 440 nm and 670 nm when τ was about 1.0-1.9 at 440 nm. We estimated Å of 0.68 using B02.

Calculated spectral single scattering albedos are more difficult to validate. Because during ACE-Asia the scattering coefficient was measured at three wavelengths (450, 550, and 700 nm) using a nephelometer and the absorption coefficient was measured at 550 nm using a PSAP (Particle Soot Absorption Photometer), ω_0 can be inferred directly from measurements at only 550 nm. Only a few studies reported ω_0 at several wavelengths, mainly based on retrievals from radiation measurements. *Bergstrom et al.* [2004] retrieved ω_0 of 0.87 at 400 nm and 0.95 at 900 nm from upward and downward spectral solar irradiances measured during ACE-Asia. *Alfaro et al.* [2003] determined ω_0 of 0.89 at 441 nm and 0.95 at 873 nm by inverting sun photometer measurements in the high dust event at Zhenbeitai. *Dubovik et al.* [2002] retrieved ω_0 of 0.92, 0.95, 0.96, and 0.97 at 440, 670, 870, and 1020 nm, respectively, from the AERONET site in Bahrain. These values agree with the upper bound of our modeled aerosol single scattering albedo.

2.4.1 Mixing State

Some modeling studies have suggested that an internal mixture of BC and non-absorbing aqueous aerosols absorbs more light than their external mixture does. Here we consider the external mixing of BC and non-absorbing aerosols, but we investigate the internal mixing of BC and dust in order to examine how the mixing of the two absorbing aerosols, having different size modes and spectral absorption features, can affect spectral light absorption and actinic fluxes. To this end, we analyzed eight types of BC and dust mixtures, which were constructed by applying internal or external mixing states to four combinations of H10 or H1 dust and high BC in the presence of high pollution or low BC

in the presence of low pollution. The high and low concentrations of BC were 1.8 and 0.2 $\mu g/m^3$, respectively (see section 3.2). The H10 or H1 dust has the moderate loading and C04 size distribution. Note that high and low pollution cases differ not only in the amount of BC, but also in OC and WSAs, both of which do not absorb light but contribute to scattering.

The optical calculations of dust-BC internal mixtures are difficult because the particles are solid and exhibit complex irregular shapes. Although during ACE-Asia the microscopic measurements of dust-BC aggregated particles were conducted by the Anderson group [*Arimoto et al.*, 2006], the data reported are not sufficient to perform the accurate optical modeling that takes into account the morphology and composition of dust-BC particles as a function of size. Therefore we adopted the simplified well-mixed sphere method of *Lesins et al.* [2002], in which the new mass distribution of a dust-BC internal mixture is calculated by adding the mass of the smaller size mode to that of the larger size modes to form a homogeneous sphere. Thus the number concentration of the larger size mode increases. We assume that homogeneous spheres are formed in dust size modes, so the mass of BC was partitioned between dust size modes according to their mass fractions.

Figure 2.5(a) displays ω_0 calculated for eight dust-BC mixtures, while Figure 2.5(b) presents $\omega_{0,eff}$ calculated in the 1- 2 km layer in which external or internal mixtures of dust and BC are mixed externally with low or high pollution. The differences in the single scattering albedos shown in Figures 2.5(a) and 2.5(b) demonstrate the need to consider not only BC but also other aerosol species that commonly accompany BC in the pollution outbreak while assessing the impact of dust mixing with pollution. Notice that both ω_0 and $\omega_{0,eff}$ fall into two groups depending on the dust composition: the upper family of curves is for H1 dust, and the lower one is for H10. These groups differ not only in values of ω_0 and $\omega_{0,eff}$ but also in their dependences on λ.

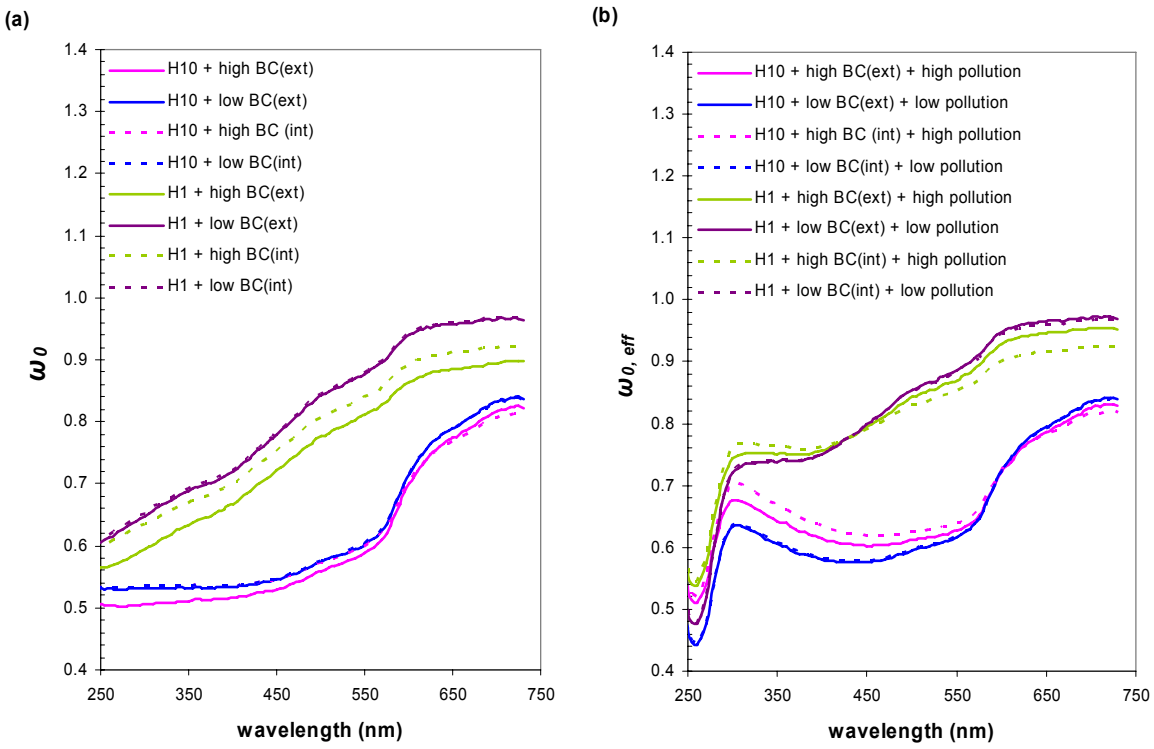

Figure 2.5: (a) Single scattering albedo, ω_0, of the dust-BC internal and external mixtures, and (b) the effective single scattering albedo, $\omega_{0,\,eff}$, in a 1-2 km layer in which external or internal dust-BC mixtures are mixed externally with low or high pollution. Mixing state of dust and BC is shown in the parentheses.

Apparent in Figure 2.5(b) is that each group has a flip point in which the magnitude of $\omega_{0,eff}$ is reversed due to mixing state. At λ smaller than the flip point, $\omega_{0,eff}$ of the internal mixtures are higher than those of the external ones. The H1 group has a flip point around 430 nm, and H10 group has one at about 600 nm for the mixture with high BC. Therefore the internal mixture of H10 dust with a high concentration of BC results in the reduction of the shortwave absorption in a wider range of wavelengths than the internal mixture of H1 dust does.

2.5 Analysis of the Diurnal Cycle and Vertical Profile of Photolysis Rates

We have carried out extensive TUV simulations considering five dust size distributions, three mineralogical compositions of dust aggregates, and the internal and external mixtures of BC and dust in the presence of other aerosols according to selected loading scenarios. In each case, the spectral actinic fluxes, vertical profiles of J-values, and their diurnal variations, as well as changes in these quantities relative to the aerosol-free condition were examined. The changes in the spectral actinic flux, $\Delta F(\lambda)$, changes in J-values of each considered photolysis reaction, ΔJ, and the fractional changes in J-values, FCJ, were calculated as follows:

$$\Delta F(\lambda) = F(\lambda)_{aerosol} - F(\lambda)_{aerosol-free} \tag{2.4}$$

$$\Delta J = J_{aerosol} - J_{aerosol-free} \tag{2.5}$$

$$FCJ = \frac{J_{aerosol} - J_{aerosol-free}}{J_{aerosol-free}} = \frac{\Delta J}{J_{aerosol-free}} \tag{2.6}$$

To help in delineating the effect of spectral aerosol optical characteristics, 13 photolysis reactions were classified into three groups according to their photolytic wavelength ranges and the shapes of vertical profile of J-values in the molecular (aerosol-free) atmosphere (see Table 2.1). Group I consists of the reactions having photolytic wavelengths in the UV (210-380 nm), group II at the shorter visible wavelengths (310-420 nm), and group III at the longer visible wavelengths (410-730 nm). Each group has a specific vertical profile of J-values, resulting from distinct differences of the J-values at 4 km and those at the surface in the molecular atmosphere. These differences are more than 20% in group I, 10-20% in group II, and less than 10% in group III. Although the photolytic wavelengths of $J[NO_2]$ fall into groups I and II, and those of $J[O_3(O^3P)]$ fall into groups I and III, differences between the J-values at 4 km and the surface are 17% for $J[NO_2]$ and 6% for $J[O_3(O^3P)]$. Therefore $J[NO_2]$ and $J[O_3(O^3P)]$ were assigned to

groups II and III, respectively. The $J[O_3(O^1D)]$, $J[NO_2]$, and $J[NO_3]$ were selected as representative photolysis reactions of groups I, II, and III, respectively.

The presence of dust in the atmosphere causes distinct changes in spectral actinic fluxes. Absolute values of $\Delta F(\lambda)$ in dust-laden cases are larger than those in dust-free cases by a factor of 5 to 10. To illustrate, Figure 2.6 shows $\Delta F(\lambda)$ calculated for different aerosol loadings (cases 1-6 from Table 2.4) at an altitude of 2 km and at 1200z and 1700z. The H1 dust with the C04 size distribution was considered in these calculations. In clean and low pollution (cases 1-2), $\Delta F(\lambda)$ has small but positive values (i.e., surplus), indicating that light scattering by aerosols dominates over the light absorption. In dust-laden conditions at local noon, there is a transitional point at the wavelength λ_{tp} at which $\Delta F(\lambda_{tp}) = 0$. Below λ_{tp} down to about 290 nm where the aerosol effect becomes negligible, $\Delta F(\lambda)$ has negative values (i.e., deficit). Conversely, there is a surplus in the

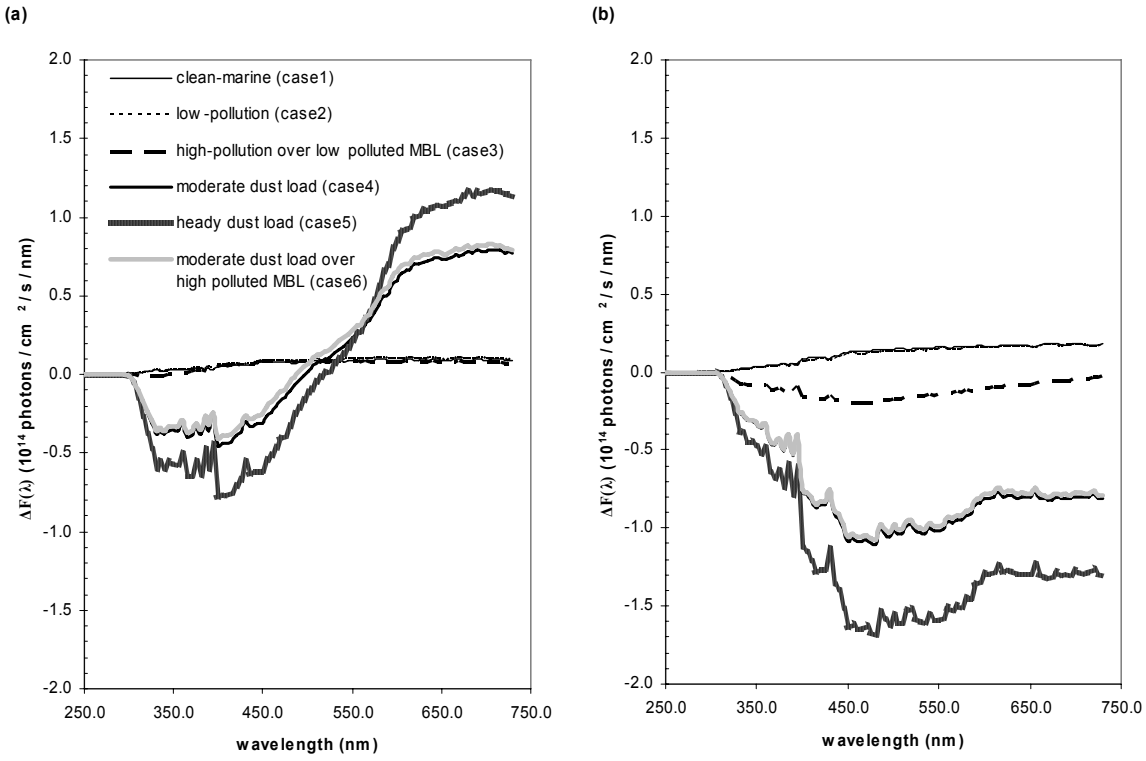

Figure 2.6: Changes in spectral actinic fluxes, $\Delta F(\lambda)$, due to different aerosol loading conditions at an altitude of 2 km at (a) 1200z and (b) 1700z for H1 dust and C04 size distribution.

actinic flux (i.e., $\Delta F(\lambda) > 0$) at λ larger than λ_{tp}. Similar behavior of $\Delta F(\lambda)$ was observed at other altitudes, although the position of the transition point λ_{tp} moves to the longer wavelengths with decreasing altitude. With time the sun angle decreases. This shifts λ_{tp} towards the longer wavelengths until no transitional point is being observed in the photolytic spectral range (see Figure 2.6(b)).

These changes in the actinic flux can be understood by considering the changes of its direct and diffuse components. The direct radiation always decreases in the presence of aerosols, depending on the optical depth and path length. The increased diffuse radiation compensates some losses in the direct component, except in the case of the long path and when values of $\omega_{0,eff}$ are low. The existence of the transition point λ_{tp} implies that the presence of dust may result either in a decrease or in an increase of J-values that would depend on whether the photolytic wavelength range of a particular gas is below or above λ_{tp}. For a given sun position, our modeling results indicate that $\Delta F(\lambda)$ values as well as the position of the transition point λ_{tp} depend on the effective spectral optical properties, including dust properties themselves, tied to aerosol loading conditions.

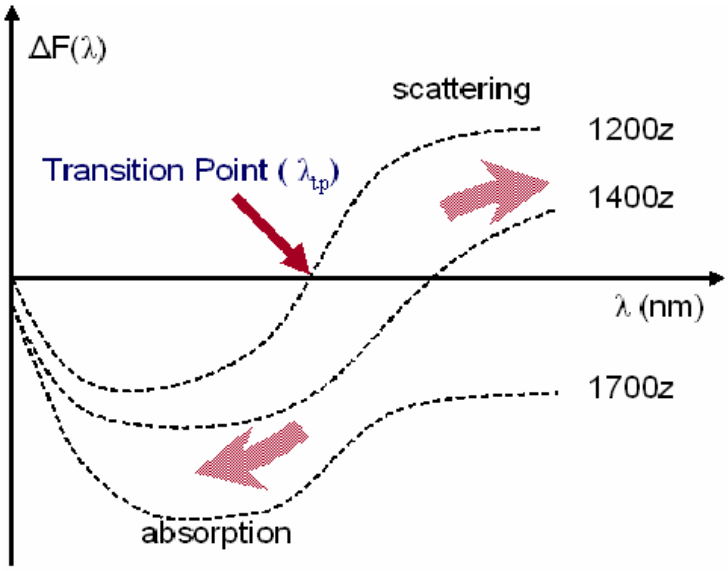

Figure 2.7: schematic diagram of the changes in actinic spectral actinic fluxes, $\Delta F(\lambda)$ and transition point, λ_{tp} .

The effect of differing dust size distributions are shown in Figures 2.8 - 2.10. Figure 2.8 presents $\Delta F(\lambda)$ calculated at an altitude of 2 km at 1200z and 1700z for H1 dust of moderate load (case 4 in Table 4). Notice that at local noon the transition point λ_{tp} moves to the longer wavelength as the size distribution of dust shifts to the coarse mode. At this altitude the deficit in $F(\lambda)$ in the UV-short visible is the largest for the C04 size distribution and the smallest for B02. However, below the dust layer, absolute values of $\Delta F(\lambda)$ corresponding to C04 are the smallest (not shown). Implications for photolysis rates are illustrated in Figures 2.9 and 2.10. They show the vertical profile at local noon and diurnal variation of ΔJ, respectively, for the reactions representative of three groups. The dust models are the same as in Figure 2.8. It is apparent that ΔJs at 2 km reflect the spectral changes in actinic fluxes shown in Figure 2.8(a). $J[O_3(O^1D)]$ has the shortest photolytic wavelengths (210-340 nm) at which $\Delta F(\lambda)$ values are negative, and thus

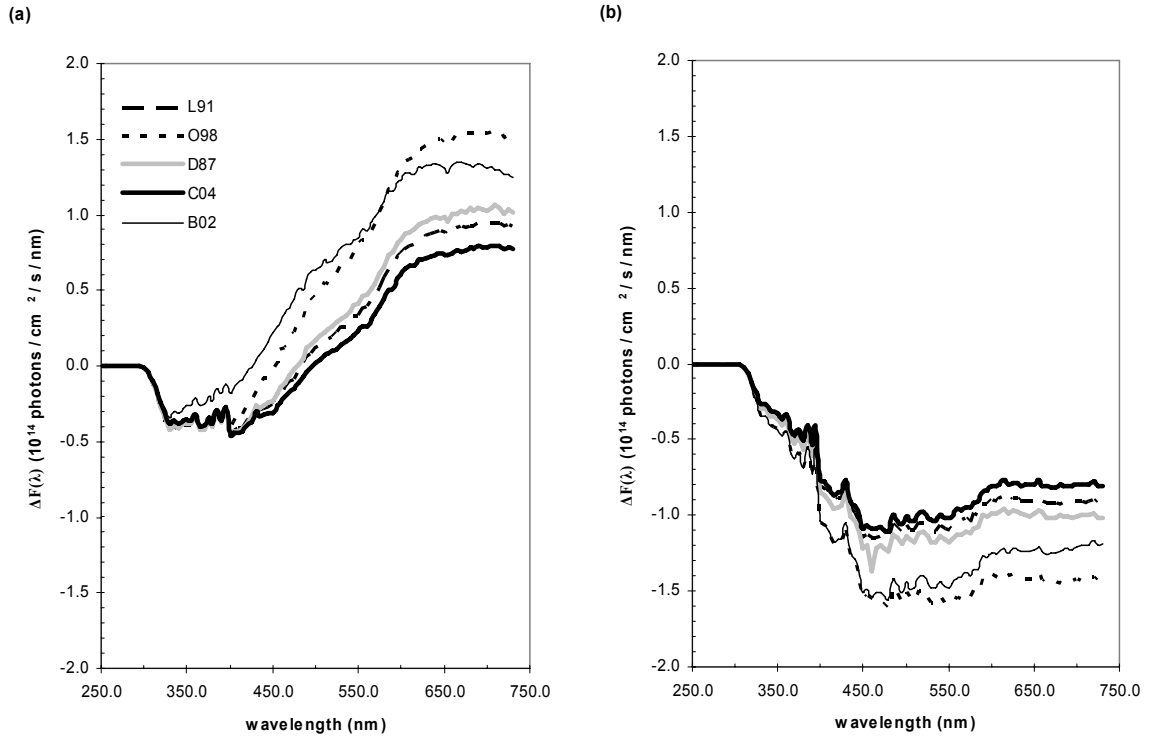

Figure 2.8: Changes in spectral actinic fluxes, $\Delta F(\lambda)$, due to dust size distributions at an altitude of 2 km at (a) 1200z and (b) 1700z for H1 dust and moderate dust loading (case 4).

$\Delta J[O_3(O^1D)]$ values are also negative at 2 km. Similarly, $\Delta F(\lambda)$ values are negative in the 210-420 nm wavelength range resulting in a decrease of $J[NO_2]$ at 2 km relative to the aerosol-free conditions. In contrast, $\Delta J[NO_3]$ values are positive because of positive $\Delta F(\lambda)$ values in the 585-635 nm spectral range. Thus dust-induced spectral changes in the actinic fluxes in this case result in a decrease of J-values in groups I and II while J-values of group III are increased.

One can also notice in Figure 2.9 that ΔJ values in the upper and lower dust layers differ significantly among the three groups of photolysis reactions. J-values in groups I and II decrease below the dust layer (below 1 km), so that FCJs are 30-46% and 25-37%, respectively, depending on dust size distribution. Above the dust layer (above 3 km) ΔJ values differ little between dust size distributions, with the exception of B02. In turn, the J-values in group III increase above the dust layer, FCJs are 10-25% depending on dust size distribution, but they differ only slightly below the dust layer. In all groups, B02 causes the distinct differences compared to other size distributions.

The diurnal variations of ΔJ also differ between the three groups. For instance, Figure 2.10 shows the behavior of ΔJ at the surface as a function of time from local noon to 1900z (local sunset). Although the effect of size distribution on ΔJ values is apparent, the temporal behavior of ΔJ of a given group is similar among the differing size distributions. In all cases the largest changes in ΔJ are caused by the B02 or O98, which are both shifted to the fine size mode. The similar diurnal cycle is found in the dust layer (not shown), though ΔJs of groups I and II become less negative, and ΔJs of groups III remain positive over the longer time period and are higher than those at the surface. Regardless of the size distribution, the lowest values of ΔJ in groups I, II, and III appear at about noon, 4 pm, and 6 pm, respectively.

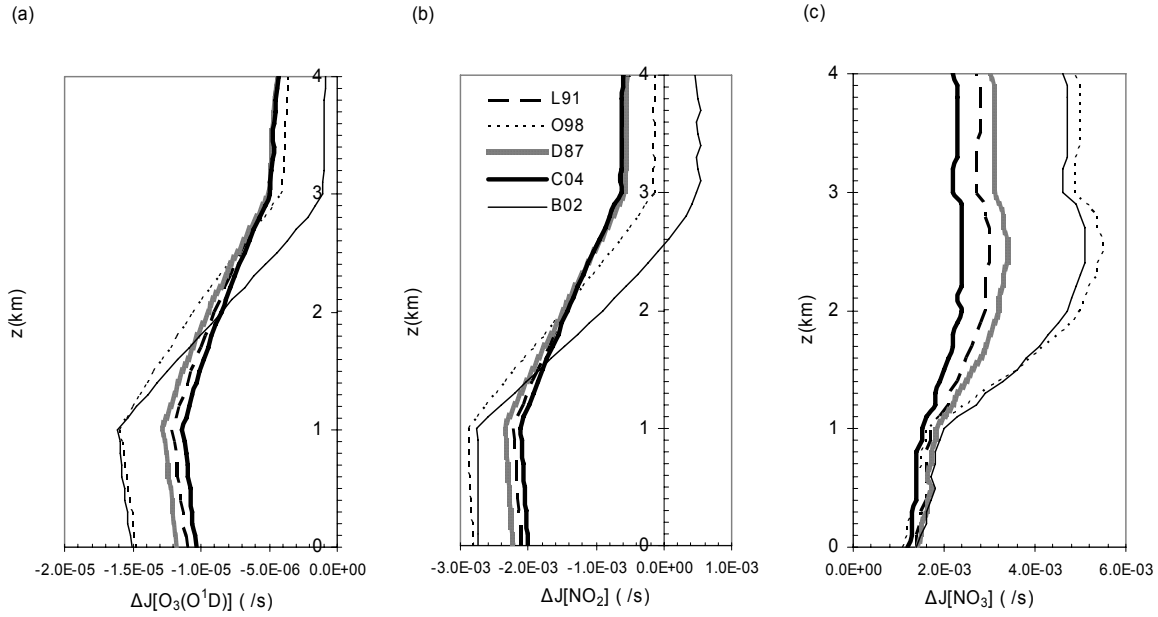

Figure 2.9: The vertical profiles of (a) $\Delta J[O_3 (O^1D)]$, (b) $\Delta J[NO_2]$, and (c) $\Delta J[NO_3]$ at 1200z due to the different dust size distributions for H1 dust and moderate dust loading (case 4).

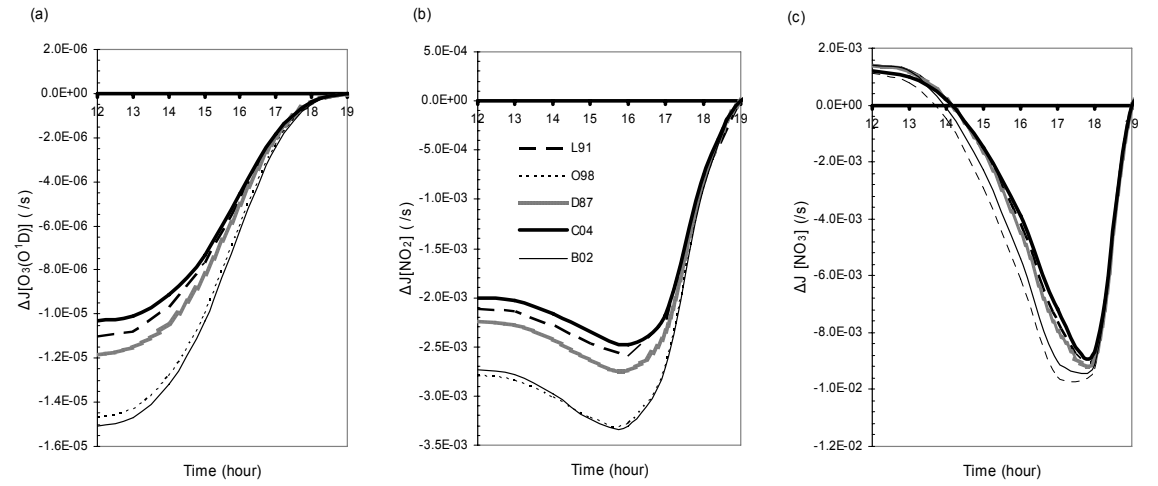

Figure 2.10: Figure 2.10: The diurnal variation of (a) $\Delta J[O_3 (O^1D)]$, (b) $\Delta J[NO_2]$, and (c) $\Delta J[NO_3]$ at the surface due to the different dust size distributions for H1 dust and moderate dust loading (case 4).

The effect of the mineralogical composition is illustrated in Figures 2.11 – 2.13. Figure 2.11 presents $\Delta F(\lambda)$ at 2 km calculated for H1, H5, and H10 dust aggregates, the C04 size distribution, and moderate dust load (case 4). As the amount of hematite in aggregates increases, the transition point λ_{tp} moves to the longer visible wavelength, and the actinic flux decreases over the broader spectral region. Apparent are larger differences between H1 and H5 than between H5 and H10, although in the latter case differences become noticeable at longer visible wavelengths. This behavior of $\Delta F(\lambda)$ can be expected given the spectral dependence of effective optical properties shown in Figure 2.4. Because τ_{eff} does not depend on the amount of iron oxides, the differences in $\Delta F(\lambda)$ in this case are caused by the differing effect of the varying light absorption on the diffuse radiation.

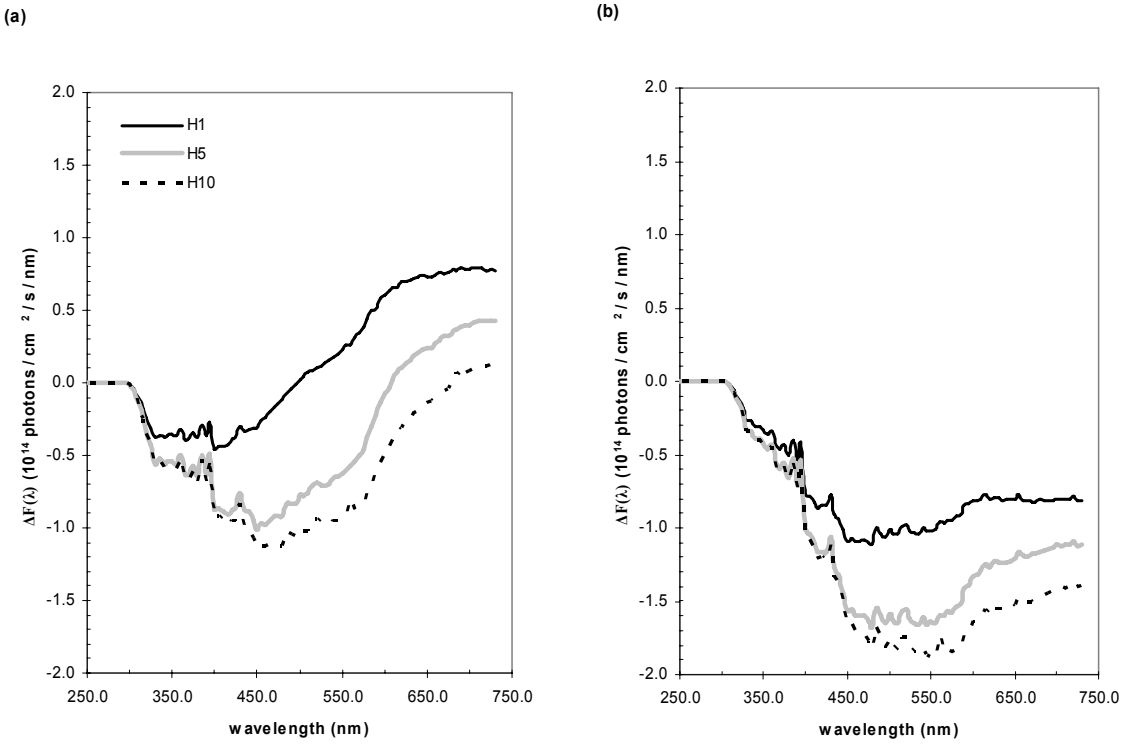

Figure 2.11: Changes in spectral actinic fluxes, $\Delta F(\lambda)$, due to different mineralogical compositions at an altitude of 2 km at (a) 1200z and (b) 1700z for the C04 size distribution and moderate dust loading (case 4).

Figure 2.12 shows how the mineralogical composition affects the vertical profiles of ΔJ at local noon. Again, the behavior of ΔJ values at 2 km of three groups is related directly to the spectral changes in actinic fluxes caused by different dust absorption as shown in Figure 2.11(a). ΔJ of groups I and II are both negative because of the negative ΔF(λ) values in the corresponding photolytic ranges. Unlike those groups, group III has either positive or negative values of ΔJ. Clearly, spectral absorption of dust is a key parameter in controlling the sign of ΔJ of group III.

Figure 2.12 also shows that the vertical profiles of $\Delta J[O_3(O^1D)]$ and $\Delta J[NO_2]$ of H5 dust are similar to those of H10 dust because the spectral light absorption at photolytic wavelengths of $J[O_3(O^1D)]$ and $J[NO_2]$ is similar between H5 and H10 dust. However, the vertical profiles of $\Delta J[NO_3]$ differ among the dust layers containing H1, H5, and H10. In particular, while H1 dust increases J-values throughout the lower atmosphere, H10 dust decreases them in and below the dust layer relative to the aerosol-free atmosphere.

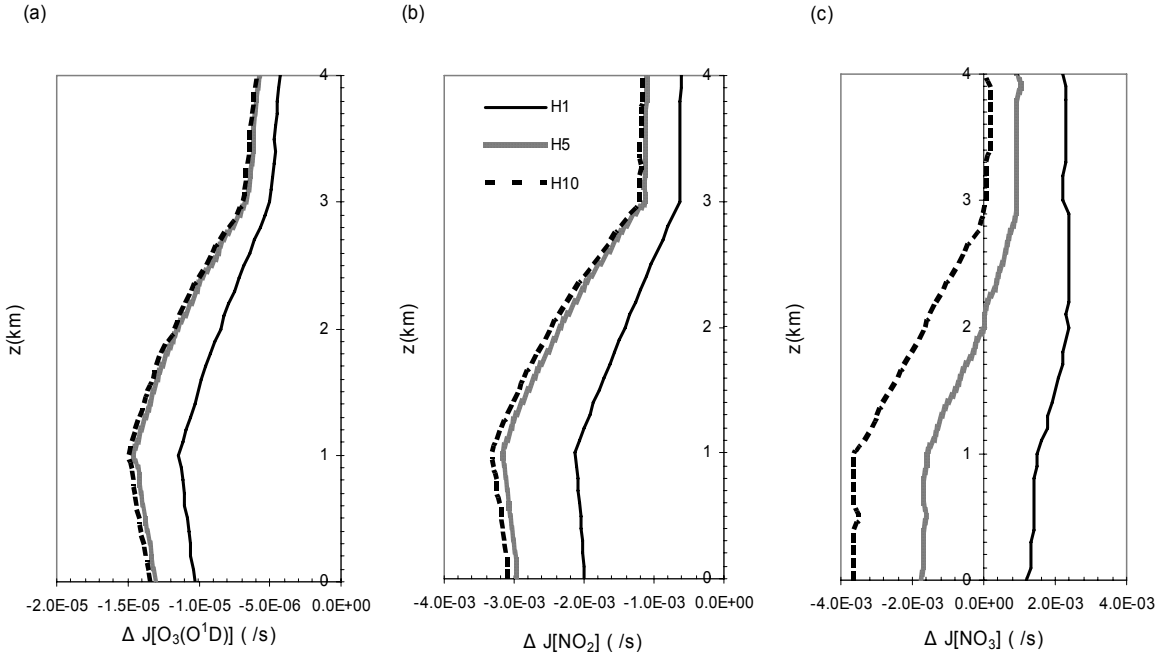

Figure 2.12: The vertical profiles of (a) $\Delta J[O_3\ (O^1D)]$, (b) $\Delta J[NO_2]$, and (c) $\Delta J[NO_3]$ at 1200z due to the different mineralogical compositions for the C04 size distribution and moderate dust loading (case 4).

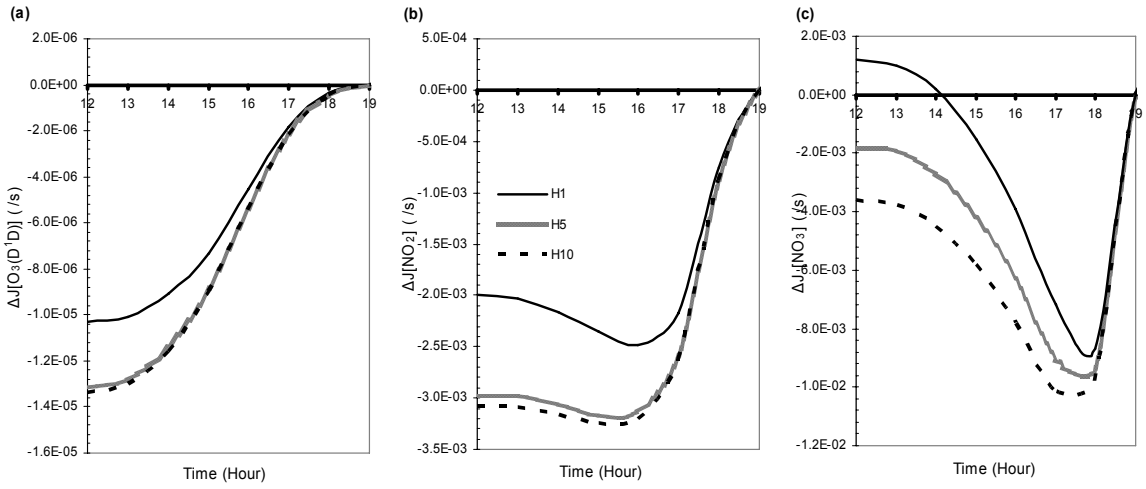

Figure 2.13: The diurnal variation of (a) $\Delta J[O_3 (O^1D)]$, (b) $\Delta J[NO_2]$, and (c) $\Delta J[NO_3]$ at the surface due to the different mineralogical compositions for the C04 size distribution and moderate dust loading (case 4).

Finally, Figure 2.13 shows how the mineralogical composition affects the diurnal variation of ΔJ at the surface. As in the case of differing dust size distributions, changes in the amount of iron oxides do not affect the temporal behavior of ΔJs but do affect their values. The lowest values of ΔJs in group I, II and III appear at about the same times in Figures 2.10 and 2.13. The similar diurnal cycle is found within the dust layer (not shown).

Overall, Figures 2.11 - 2.13 clearly show the importance of the iron oxide amount in dust aggregates for modeling the actinic fluxes and J-values. Taking into account the regional differences in the dust composition not only will be needed to accurately model a decrease in J-values of groups I and II but also to determine a correct sign and value of ΔJ of group III. Our results also demonstrate that previous studies that used the "dust-like" model from *d'Almeida et al*. [1991], which has too low ω_0 (see Figure 2.3), have computed too low negative values of ΔJ for all three groups, resulting in an erroneous assessment of the dust impact on the photolysis rates.

Table 2.5: Fractional Changes in J-values, FCJ (%), Calculated at the Surface and at Local Noon for Considered Mixtures of BC and Dust

	Mixing state	FCJ(%) of Group I	FCJ(%) of Group II	FCJ(%) of Group III
Dust: C04 dust size distribution, Moderate dust loading over low polluted MBL (case 7)				
H10/high BC/high pol	External	-47.3 (6.23E-3)	-42.7 (7.21E-3)	-24.5 (3.96E-2)
H10/high BC/high pol	Internal	-42.6 (3.74E-3)	-38.8 (7.49E-3)	-23.2 (3.76E-2)
H10/low BC/low pol	External	-41.3 (3.06E-3)	-38.3 (7.04E-3)	-22.4 (3.90E-2)
H10/low BC/low pol	Internal	-41.4 (2.46E-3)	-38.4 (6.19E-3)	-22.5 (3.94E-2)
H1/high BC/high pol	External	-38.7 (1.21E-2)	-31.3 (1.36E-2)	-2.3 (4.17E-2)
H1/high BC/high pol	Internal	-34.6 (9.24E-3)	-28.3 (9.23E-3)	-4.9 (3.46E-2)
H1/low BC/low pol	External	-31.7 (8.19E-3)	-25.6 (8.69E-3)	0.7 (4.05E-2)
H1/low BC/low pol	Internal	-31.3 (7.98E-3)	-25.5 (1.04E-2)	0.4 (3.95E-2)
Dust: C04 dust size distribution, Case 7, except for light dust loading				
H10/high BC/high pol	External	-23.4 (6.66E-3)	-18.7 (6.29E-3)	-7.7 (2.20E-2)
H10/high BC/high pol	Internal	-16.3 (3.91E-3)	-13.2 (6.08E-3)	-5.0 (1.79E-2)
H10/low BC/low pol	External	-15.4 (2.76E-3)	-13.0 (2.21E-3)	-5.5 (1.84E-2)
H10/low BC/low pol	Internal	-15.0 (2.66E-3)	-12.8 (4.77E-3)	-5.1 (1.51E-2)
H1/high BC/high pol	External	-19.0 (9.52E-3)	-13.1 (7.78E-3)	0.9 (1.97E-2)
H1/high BC/high pol	Internal	-11.4 (6.92E-3)	-7.2 (6.27E-3)	4.1 (1.59E-2)
H1/low BC/low pol	External	-10.5 (4.78E-3)	-7.2 (6.27E-3)	3.4 (1.34E-2)
H1/low BC/low pol	Internal	-9.6 (4.25E-3)	-6.3 (3.67E-3)	3.7 (1.51E-2)

The numbers in parenthesis give standard deviations of FCJ in each group.
High and low pol means high and low pollution.

We also investigated the effect of the mixing state of dust and BC on the actinic fluxes and photolysis rates. Examining Figure 2.5 one can expect that the mixing state would have only a small effect in the case of the low BC concentration. This was confirmed by our calculations. To illustrate, Table 2.5 presents FCJs calculated for considered dust-BC mixtures when moderate or light dust loading is mixed with low or

high pollution (case 7). The mixtures of dust with low BC result in very similar FCJs for the internal and external mixing states, although somewhat large differences are observed in group III. Also, FCJs of this group become positive for some dust-BC mixtures (see table 2.5). Relatively larger differences in FCJs are found for the high concentration of BC, still they remain within a few percent in most cases. For the high BC, we found that the external mixing state causes more negative values of FCJs in groups I and II. This is true for group III in the case of H10 dust but not for H1 dust. Nevertheless, it is apparent that the varying amount of iron oxides is a more important factor in controlling the values of FCJs than the mixing state of dust and BC.

To connect the wavelength-dependence of aerosol absorption and FCJs, we introduce the Angstrom exponent of the absorption aerosol optical depth, $Å_{abs}$. The $Å_{abs}$ values were calculated using the wavelength pairs of 210 and 380 nm, 310 and 420 nm, and 410 and 730 nm, which are the shortest and the longest photolytic wavelengths of groups I, II, and III, respectively. Figure 2.14 shows FCJs at the surface (open symbols) and within the dust layer at 2 km (filled symbols) and $Å_{abs}$ for the varying size distribution and mineralogical composition of dust. The diamonds denote FCJ and $Å_{abs}$ due to the size distribution, considering H1 dust. The squares indicate FCJ and $Å_{abs}$ due to the mineralogical composition of dust aggregates, considering the C04 size distribution. Shown FCJs are for 1200z and case 4 moderate dust loading. The lines are drawn only for illustration purposes. When the dust size distribution shifts to the fine size mode (e.g., B02 and O98), $Å_{abs}$ increases, and FCJs of groups I and II become more negative, as low as -44% for group I at the surface. At 2 km FCJs of these groups are less negative that at the surface. In turn, FCJs of group III remain positive, showing lower sensitivity to differing size distributions compared to groups I and II.

As the amount of iron oxide in dust aggregates increases, $Å_{abs}$ decreases, and FCJs become more negative in all three groups. Clearly, FCJs of groups I and II are the most sensitive to the varying amount of iron oxides in the range from 1% (H1 dust) to 5%

(H5 dust), whereas group III is sensitive to the entire range considered. Given that the regional variability in the iron oxide amount is likely to be in the range from 1 to 10%, our results stress the need to include the source-dependent mineralogical composition into calculations of the photolysis rates to make assessments of the dust impact on the photochemistry more accurate. Furthermore, using globally uniform data on the size distribution and refractive indices of dust in the global models is likely to cause large errors in J-values. *Martin et al.* [2003] showed that the surface $J[O_3(O^1D)]$ decreased by 5-20% in the Northern Hemisphere in the presence of mineral dust and biomass burning aerosol plumes. These changes in $J[O_3(O^1D)]$ were estimated by using the temporal (seasonal) and spatial (geographical) variability of atmospheric abundance of aerosols but neglecting the variations of the size distribution and spectral refractive indices (or composition) of mineral dust. If we consider the spectral light absorption of atmospheric mineral dust at a certain geographical location and at local noon, $J[O_3(O^1D)]$ might decrease by 30.5% in the case of less absorbing dust (C04 size distribution and H1 dust composition) and up to 44.2% in the case of more absorbing dust (H10 dust composition and O98 or D91 size distribution). Thus variability of light absorption of dust itself can decrease $J[O_3(O^1D)]$ by 8.6-13.7%.

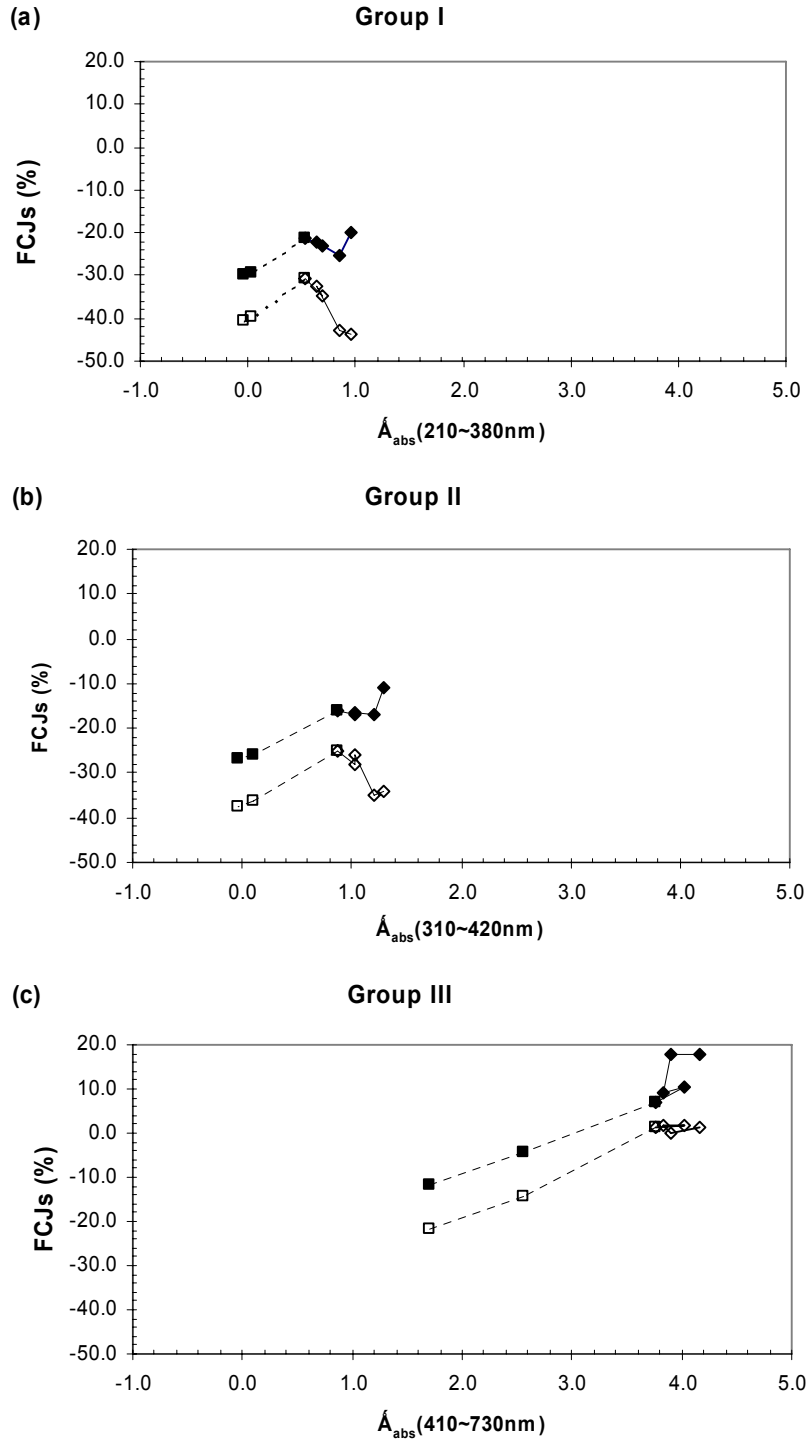

Figure 2.14: The relationship between FCJs and Angstrom exponent of absorption aerosol optical depth $\acute{A}_{abs}$ in (a) groups I, (b) group II, and (c) group III, at 1200z at surface (open symbols) and 2 km (filled symbols) due to the size distribution (diamonds) and mineralogical composition (boxes) of dust particles. Lines are for illustrative purposes only.

2.6 Conclusions

In this Chapter we explored the effect of mineral dust aerosols on photolysis rates in clean and polluted marine environments by investigating the spectral optical properties of dust according to its size, composition, and mixing states with other types of aerosols. The spectral optical properties in several representative aerosol scenarios were calculated with Mie theory and the data from recent field and laboratory studies. The new aerosol block was incorporated into the TUV code that enables us to calculate the spectral actinic fluxes and photolysis rates. The 13 photolysis reactions considered were grouped according to their photolytic wavelengths and the shape of vertical profile of J-values in the cloud- and aerosol-free atmosphere (see Table 2.1). Specific differences and similarities were found between these groups in the way that they were affected by aerosol spectral optical properties. A brief summary of our main findings is as follows.

1. Considering common size distributions and the varying amount of iron oxides that is likely to represent the regional variability of dust composition, we demonstrate that, because of its specific spectral optical characteristics, the presence of dust results in distinct changes of spectral actinic fluxes in both clean and polluted marine environments. These changes $\Delta F(\lambda)$ (see Eq.2.4) can be either negative or positive. The transition point λ_{tp}, at which the sign of $\Delta F(\lambda)$ changes, moves to the longer wavelengths as the amount of dust load increases, a dust size distribution is shifted to coarse size mode, and the iron oxide content in dust aggregates increases. For a given dust-laden condition, λ_{tp} also changes with the sun position (i.e., time of the day) and altitudes.

2. We found that dust-induced changes in actinic fluxes affect J-values differently, depending on the photolytic wavelength range of a given gas. For gases in group I, ΔJ are negative through the lower atmosphere. Group II has negative ΔJs in and below the dust layer, but ΔJs become positive above the dust layer with the B02 particle size distribution and low absorbing dust (H1). In contrast, ΔJs of group III are positive for

all size distributions considered for H1 dust, and they become negative as the iron oxide content increases. These results indicate that the region-specific dust composition not only will be needed to accurately model a decrease in J-values of groups I and II but also to determine a correct sign and value of ΔJ of group III. The changes in the vertical profiles of ΔJ values are the largest in group I for any changes in microphysical and chemical properties of mineral dust. The FCJs (see Eq.6) in group I at the surface were between about -31% and -47.3%.

3. The temporal behavior of ΔJ of a given group is similar among the differing size distributions and composition of dust. The lowest values of ΔJ in groups I, II, and III appear at about noon, 4 pm, and 6 pm, respectively. However, values of ΔJ vary by a factor 1.5-2 depending on dust properties. In all cases the largest changes in ΔJ are caused by the B02 or O98 size distributions, which are both shifted to the fine size mode. J-values of groups I and II are the most sensitive to the varying amount of iron oxides in the range from 1% (H1 dust) to 5% (H5 dust), whereas group III is sensitive to the entire range considered (1-10%). The similar diurnal cycles of ΔJ are found below and in the dust layer, though in the latter case ΔJs of groups I and II become less negative, and ΔJs of groups III remain positive over the longer time period and are higher than those at the surface.

4. The mixing state of dust and BC (external or internal) causes very similar changes in ΔJs when the BC concentration is low. For the high BC, the external mixing state causes more negative values of FCJs in groups I and II. This is true for group III in the case of H10 dust but not for H1 dust. However, it is important to keep in mind that this modeling was carried out based on a very simplified treatment of dust-BC aggregates.

We believe that more realistic representation of the physiochemical and optical properties of mineral dust will be required in order to improve calculations of the vertical profiles and diurnal cycles of J-values in dust- or dust/pollution-laden conditions. In

particular, new data on the mineralogical composition, especially the iron oxide content, that have recently become available and will become available from the ongoing field experiments offer an opportunity to develop the region-specific dust models instead of the globally-uniform generic dust model, which is commonly used in the regional and climate models. This will be required to advance the understanding of not only the influence of dust on photochemistry but also to assess more reliably the impact of dust on regional and global climate.

CHAPTER III

THE EFFECTS OF SIZE-RESOLVED MINERALOGICAL COMPOSITION ON HETEROGENEOUS CHEMISTRY ON DUST PARTICLE SURFACES

3.1 Introduction

The surface area of mineral dust amounts to half of those of all aerosols in the atmosphere [*Penner et. al.*, 2001] and its distinct mineral species show unique reactions with gaseous species [*Claquin et al.,* 1999; *Usher et al.*, 2003]. The heterogeneous reactions on the dust particles cause the gaseous loss of such gases as O_3, SO_2, NO_2, and HNO_3, in the atmosphere. These reactions cause dust particles to neutralize the acidity of atmospheric gases and to oxidize substances or associated anions [*Beilke and Gravenhorst,* 1978], resulting in a direct effect on the budget of atmospheric gases, in particular, a reduction in ozone concentration [*Dentener and Crutzen,* 1993; *Dentener et al.,* 1996; *de Reus, et al.,* 2000; *Bauer et al,* 2004; *Tang et al.,* 2004b]. The heterogeneous reactions may also change the optical and hygroscopic properties of mineral dust, leading to an influence on radiative fluxes and a role as CCN [*Parungo,* 1995; *Levin* et al., 1996, *Dentener et al.,* 1996].

A decrease in ozone concentration was observed in dust plumes, with the heterogeneous ozone destruction being proportional to the amount of dust concentrations [*de Reus et al.*, 2000]. Chemistry modeling studies also showed that ozone concentration decreases in the heavy dust load conditions due to heterogeneous loss on dust particle surfaces [*Dentener and Crutzen,* 1993; *Dentener et al.*, 1996; *Tie et al.*, 2001; *Martin et*

al., 2003; *Tang et al.*, 2004b; *Bauer et al.*, 2004]. However, a number of simplified assumptions on the size and composition of dust particles were made in calculations of heterogeneous loss rates. Each research model used a fixed size distribution and one value of uptake coefficients. For instance, the dust size distribution was chosen from among commonly-known dust size distributions such as the *D'Almeida*'s model [*D'Almeida*, 1987; *Dentenr et al.*, 1996; *Bian and Zender*, 2003], the *Jaenicke*'s model [*Jaenicke et al.*, 1993; *Song and Carmichael*, 2001], a single mode size distribution [*Zhang et al.*, 1999; *Liao et al.*, 2003], or calculated using a few size bins in the regional or global climate models [*Bian and Zender*, 2003; *Tang et al.*, 2004b; *Bauer et al.*, 2004, 2005; *Martin et al.*, 2003]. However, the differences in the heterogeneous loss rates due to differing dust size distributions were not investigated in detail. The results of Chapter 2 of this thesis demonstrated that dust size distribution is as important as the mineralogical composition of dust particles in controlling the photolysis rates. Thus it is important to examine the role of the dust size distribution in heterogeneous chemistry.

In terms of the mineralogical composition of dust particles, past studies used the one-value to represent the uptake coefficients by dust particle aerosols. For instance, O_3 uptake coefficient were most popularly used with 1.0×10^{-5} - 2.0×10^{-4} that *Dentener et al.*[1996] estimated from O_3 deposition measurements on iron, organic, and calcarious soil [*Liao et al.*, 2003; *Martin et al.*, 2003]. Some recent studies,used the upper and lower limits as well as a "best guess" among the values of O_3 uptake coefficients by authentic dust, mineral species, or metal oxides [*Tang et al., 2004b; Bian and Zender*, 2003]. Other studies adopted simply the values of authentic dust samples [*Bauer et al.*, 2004]. For HNO_3 and SO_2 uptakes, the uptake coefficients of calcium carbonate were often used as

those of dust particle aerosols [*Dentener et al., 1996; Tang et al., 2004b; Bauer et al.*, 2004; *Liao et al.*, 2003; *Song and Carmichael,* 2001; *Bian and Zender,* 2003]. In spite of efforts to supply the right values of uptake coefficients to a heterogeneous chemistry model, one kinetic constant is not enough to represent the uptake coefficient of dust particles, which are multi-component aerosols.

In contrast to models, laboratory studies have more thoroughly addressed mineralogical composition in understanding heterogeneous reactions on dust particles. These laboratory studies deal with uptake of metal oxides, mineral species, and authentic dust samples [*Usher et al.*, 2003 (reference therein)]; RH dependence of the uptake coefficients [*Vlasenko et al.*, 2006; *Chang et al.*, 2005; *Martin et al.*, 2001; *Mashburn et al.*, 2006]; deliquescent products [*Gibson et al.*, 2006]; and the morphological changes of dust particles [*Krueger et al.*, 2003; *Laskin et al.*, 2005]. However, few of the results of these laboratory studies on the individual mineral species have been considered in previous model studies.

The goal of this chapter is to investigate how the size and mineralogical composition of dust affect the heterogeneous loss rates ($\boldsymbol{k_{loss,\ j}}$) of gaseous species on particle surfaces and the implications for tropospheric photochemistry. The size-resolved mineralogical mixtures of dust particles are constructed by selecting a range of mass fractions of the three main mineral species, considering the alkalinity from carbonate-containing species and the light absorption from iron oxide-containing clay, and by pursuing consistent treatment of mineral dust aerosols in both the chemical and radiative modeling. The calculations of heterogeneous loss rates are conducted by using the *Fuchs-Sutugin* approximation in the transition regime. Recent data on uptake coefficients of

individual minerals and authentic dust and on several dust size distributions reported from field and laboratory experiments are used.

3.2 Approach

3.2.1 *Fuchs-Sutugin* approximation

The mass transfer on the surface of non-volatile inorganic compounds can be described as the gas-to-particle diffusion which depends on the particle size relative to the mean free path of air molecule in the surrounding environment. In order to calculate the mass transfer on the highly dispersive aerosols ($0.1<K_n<10.0$, where $K_n(l/r)$ is the Knudsen number which is defined as the ratio of mean free path of a gas molecule in air, l to a particle radius, r), *Fuchs and Sutugin* (1970) used the effective mean free path satisfying the flux matching at the transition regime. In the *Fuchs-Sutugin* approximation, a heterogeneous loss rate on dust particles can be calculated by integrating the product of the gas-to-particle diffusion constant and the number concentration over the particle size range [*Dentener et al.*, 1996; *Zhang et al.*, 1999; *Song and Carmichael*, 2001; *Tang et al.*, 2004b; *Bauer et al*., 2004]. This study uses maximum radius of 7.5 μm which is the size-cutoff radius.

The overall heterogeneous loss rate, $k_{loss,j}$, of the reactive gaseous species j on the dust particles is

$$k_{loss,j} = \int_{r_1}^{r_2} k_{d,j}(r, \gamma) n(r) dr \tag{3.1}$$

$$n_m(r) = \frac{dn_m}{dr} = \frac{dN_m(r)}{d\log r} = \sum_{i=1}^{3} \frac{N_{i,m}}{\log \sigma_{g,i} (2\pi)^{1/2}} \exp\left(-\frac{[(\log r) - (\log r_{g,i})]^2}{2(\log \sigma_{g,i})^2}\right) \tag{3.2}$$

$$k_{d,j} = \frac{4\pi r D_j V}{1 + K_n[\lambda + 4(1-\gamma)/3\gamma]} \tag{3.3}$$

where n(r) is the number size distribution (cm^{-4}); r_i is the median radius of size mode i; and σ_i is standard deviation of size mode i; $k_{d,j}$ is the gas-to-particle diffusion rate constant of species j for a particle of radius r ($cm^3 s^{-1}$); $\mathbf{D_j}$ is the molecular diffusion coefficient of species j in the air ($cm^2 s^{-1}$); V is ventilation factor (≈1); and γ is uptake coefficient by aerosol particles. The changes in gaseous concentration,

$$\boldsymbol{k_{loss,j}} = \frac{\partial \mathbf{C}}{\partial \mathbf{t}} = \int_{r_2}^{r_1} \frac{4\pi r_j (C_j - C_j^e)}{1 + K_n[\lambda + \frac{4(1-\gamma)}{3\gamma}]} \mathbf{n(r)dr} \tag{3.4}$$

where, C_j and C^e_j are the gas-phase concentration of the absorbing species j and the equilibrium gas-phase concentration of species j that would be in equilibrium with the surface-adsorbed species, respectively. $\frac{\partial \mathbf{C}}{\partial \mathbf{t}}$ is a function of particle size distribution n(r) and uptake coefficient γ.

Figure 3.1(a) and (b) show the gas-to-particle diffusion rate constant of species, j, $k_{d,j}$ (or mass transfer coefficient) and overall heterogeneous loss rates, $k_{loss,j}$ as a function of particle radius and uptake coefficients. The $k_{d,j}$ is linearly proportional to uptake coefficients, γ and particle radius, r. However, when uptake coefficient, larger than 2×10^{-3} and particle radius larger than 5.0 μm, the changes in $k_{d,j}$ become small. In turn, $k_{loss,j}$ have strong nonlinear relationship with uptake coefficients, γ and particle radius, r.

In Figure 3.1(b), the $k_{loss,j}$ are calculated by integrating $k_{d,j}$ with the dust size distribution of D87. The heterogeneous loss rates, $k_{loss,j}$ remarkably increase in the

particle radius of 0.4 to 2.0 μm which belongs to the transition regime ($0.1<K_n<10.0$). The values of $k_{loss,j}$ are the largest in the particle radius of 2.0 μm when uptake coefficient

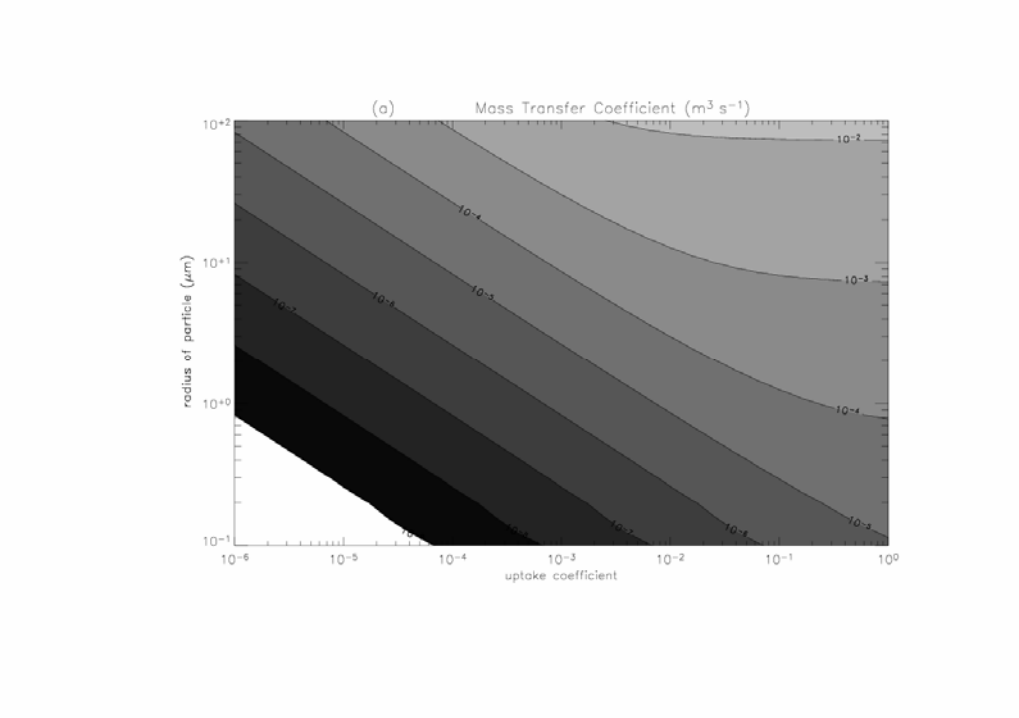

Figure 3.1 (a) The gas-to-particle diffusion rate constants

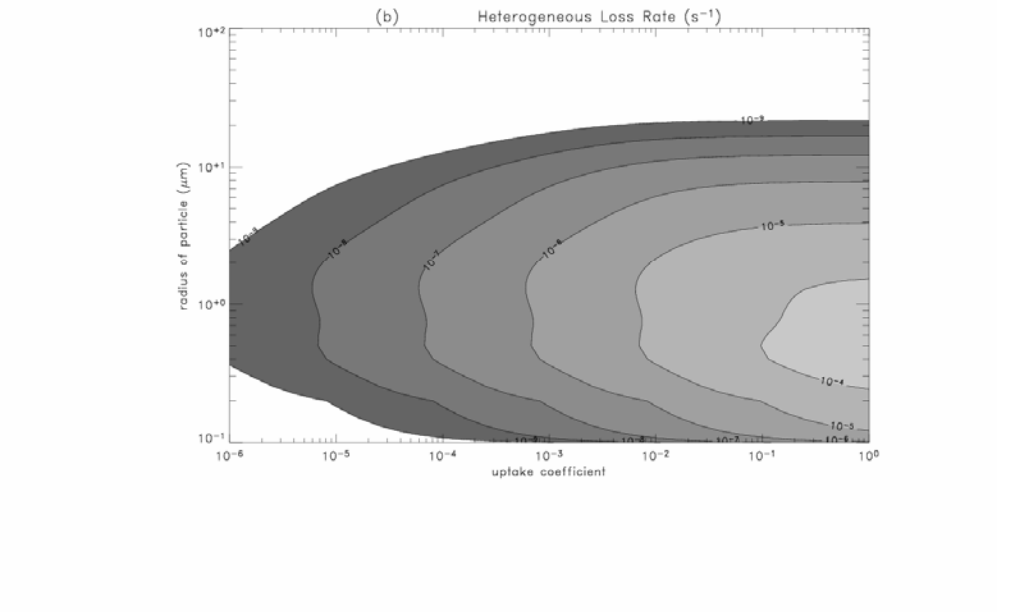

Figure 3.1 (b) Overall heterogeneous loss rates

is less than 0.1. However, the largest values move to the smaller particles such as a particle radius of 0.5 μm when uptake coefficient is larger than 0.1. This tendency is consistent to $k_{loss,j}$ used with the other size distribution although the shape of contour of $k_{loss,j}$ changes. Therefore, Figure 3.1(b) implies that the strong dependency of $k_{loss,j}$ on composition and size distribution of dust aerosols. The following sensitivities of $k_{loss,j}$ to dust size distribution and the fraction of mineralogical composition, and partitioning between fine and coarse mode are expected.

In this study, the value of $k_{loss,j}$ is calculated by the summation of heterogeneous loss rate $k_{loss,j,m}$ by individual mineral species which compose the dust mixtures. The $k_{loss,j,m}$ depends on particle size distribution $n_m(r)$ and uptake coefficient $\gamma_{m,j}$ of mineral species m:

$$k_{loss,j} = \sum_{m}^{3} k_{loss,j,m} \tag{3.5}$$

$$k_{loss,,j,\ m} = \int_{r_1}^{r_2} k_{d,j,m}(r) n_m(r) dr \tag{3.6}$$

$$k_{d,j,m} = \frac{4\pi r D_j V}{1 + K_n[\lambda + 4(1-\gamma_m)/3\gamma_m]} \tag{3.7}$$

The number size distributions of individual mineral species have the same size parameters as those of dust size distributions; however, the total number concentrations of individual mineral species, $N_{i,m}$ are converted from the mass concentration of individual mineral species. The conversion between the number concentration and mass concentration of a mineral species *m* in a size mode *i* is made using the third moment of the log-normal distribution function.

$$MW_{tot,m} = \int_0^{r_{cutoff}} \rho_m \frac{4}{3}\pi r^3 \frac{dN_m(r)}{dr} dr \quad (3.8)$$

where $MW_{tot,\ m}$ is the total mass concentration of mineral m and ρ_m is the density of a mineral m.

3.2.2 Dust size distribution

Table 3.1 shows similarities and differences among four dust size distributions used in this study. The fine and coarse modes are defined according to surface median diameter (SMD) of 2.5 μm [*Whitby and Cantrell,* 1976] since surface area is important in the heterogeneous loss on the dust particles. The first two size modes belong to a fine mode that is less than 2.5 μm of SMD. The last three modes belong to a coarse mode that is larger than 2.5 μm of SMD.

The size distributions shown in Table 3.1 were introduced in Chapter 2. Briefly, C04 denotes the dust size distribution measured by *Clarke* et al. [2004] during the ACE-Asia campaign. D87 denotes the size distribution of Saharan dust from d*'Almeida* [1987]. These two trimodal dust size distributions are shifted to the coarse mode because two modes (98.2% and 99.0% out of total mass) belong to the coarse mode. The dust model in the OPAC (Optical Properties of Aerosols and Clouds) was built based on Saharan dust [*Hess et al.*, 1998, hereafter O98]. It is relatively shifted to the fine mode because two modes (70.5% out of total mass) belong to the fine mode. B02 denotes that the size distribution was retrieved from the AERONET site at Bahrain [*Dubovik et al.*, 2002].

Table 3.1 The Log-normal Size Parameters, Median radius $r_{g,i}$, Geometric Standard Deviation $\sigma_{g,i}$, Surface Medium Diameter, SMD, and Mass Fraction of Dust Size distributions

				2.5 μm SMD		
Dust Size Distribution / Reference	Size mode	Mode1	Mode2	Mode3	Mode4	Mode5
		Fine mode		Coarse mode		
C04	$r_{g,i}$ (μm)		0.345	0.885		4.335
Clarke et al.	$\sigma_{g,i}$		1.46	1.85		1.50
[2004]	Mass fraction (%)		1.80	69.40		28.80
	SMD		0.92	3.77		12.05
D87	$r_{g,i}$ (μm)	0.08		0.70		4.99
D'Almeida	$\sigma_{g,i}$	2.10		1.90		1.60
[1987]	Mass fraction (%)	1.00		95.30		3.70
	SMD	0.48		3.19		15.52
O98	$r_{g,i}$ (μm)	0.07	0.39		1.90	
Hess et al.	$\sigma_{g,i}$	1.95	2.00		2.15	
[1998]	Mass fraction (%)	3.40	76.10		20.50	
	SMD	0.34	2.04		12.27	
B02	$r_{g,i}$ (μm)	0.088		0.832		
Dubovik et al.	$\sigma_{g,i}$	1.52		1.84		
[2002]	Mass fraction (%)	9.10		90.90		
	SMD	0.25		3.50		

3.2.3 Uptake coefficients of individual minerals

The uptake coefficients of O_3, SO_2, NO_2, and HNO_3 by minerals and metal oxides and the uptake coefficients reported in the literature are summarized in Tables 3.2 (a - d), respectively. In this study three main mineralogical species were selected based on their reactivity to atmospheric gaseous species, light absorption, and atmospheric abundance (see figure 3.2). The calcite is active to react with acidic gases. Iron oxide-clay aggregates are important to light absorption. Quartz is relatively inactive to either reactions with gaseous species or light-absorption; however, it is abundant in dust mixtures.

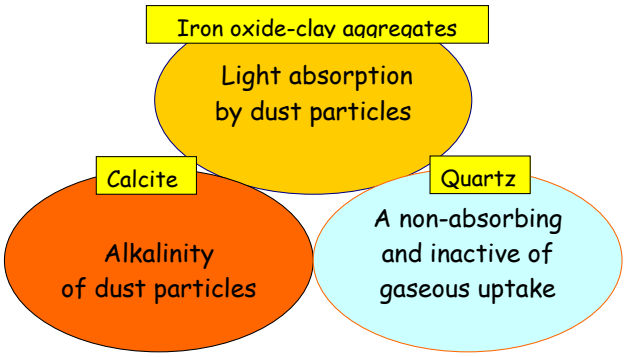

Figure 3.2 Three main mineral species used in size-resolved mineral composition of dust particles.

In order to determine the representative uptake coefficients of three main mineralogical species, the values of uptake coefficients by minerals and metal oxides were averaged over those reported by different measurement studies. The uptake coefficients of iron oxide-clay aggregates were used with those of mineralogical species such as kaolinite, illite, or montrollinite. In the absence of the uptake coefficients of the mineral species, the uptake coefficients of α-Al_2O_3 and α-Fe_2O_3 were substituted for those of iron oxide-clay aggregates. In the same manner, the uptake coefficients by calcite or dolomite were preferred to those of CaO and MgO. The uptake coefficients by quartz were relatively easy to obtain.

Table 3.2 Summary of Uptake Coefficients by Mineral Species, Metal Oxide, and Authentic Dust. **(a)** $\mathbf{O_3} \xrightarrow{dust} \mathbf{1.5\ O_2}$

Three main mineral groups/ γ used in this study	Mineral species or alternative chemical elements	Measuring type of γ	γ	References
Clay aggregates	Kaolinite Illite Montrollinite α-Al_2O_3 α-Fe_2O_3			
	Kaolinite	γ_0^{geom}	$3.0 \pm 1.0 \times 10^{-5}$	*Hanisch and Crowley, 2003 (Atmos. Chem. Phys.)*
Calcite	Calcite Dolomite $CaCO_3$ CaO MgO			
	$CaCO_3$	γ_0	4.3×10^{-7} ($k = 1.9 \times 10^{-3}$ /s)	*Hanisch and Crowley, 2003 (Atmos. Chem. Phys.) referred to Alebic-Juretic et al., 2000 (Chemosphere)*
	$CaCO_3$	γ derived		*Dentener et al., 1996 refer to Garland, 1976 using deposition velocity, $\gamma = 4\upsilon_{dep}/c$*
Quartz	SiO_2			
	SiO_2	γ_{BET}	$5.0 \pm 3.0 \times 10^{-5}$	*Mtchel et al., 2002 (GRL)*
Authentic dust				
	Saharan sand	γ_{BET}	$6.0 \pm 3.0 \times 10^{-5}$	*Mtchel et al., 2002 (GRL)* *Michel et al., 2003 (Atmos. Environ)*
	Chinese loess	γ_{BET}	$2.7 \pm 0.9 \times 10^{-5}$	*Mtchel et al., 2002 (GRL)* *Michel et al., 2003 (Atmos. Environ)*
Past studies				
	Calcite		$1.0 \times 10^{-5} \sim 2.0 \times 10^{-4}$ (5.0×10^{-5}) best guess 5.0×10^{-5} 1.0×10^{-5} $(3.0 \times 10^{-5} \sim 3.0 \times 10^{-6})$ 1.1×10^{-3} 5.0×10^{-5} $(3.0 \times 10^{-5} \sim 3.0 \times 10^{-6})$ $1.0 \times 10^{-4} \sim 1.0 \times 10^{-5}$	*Dentener et al., 1996* *Tang et al., 2004b* *Bauer et al., 2004* *Bian and Zender, 2003* *Liao et al., 2003* *Martin et al., 2003*

Table 3.2 Continued. **(b)** $SO_2 \xrightarrow{dust} SO_4^{-2}$

Three main mineral groups/ γ used in this study	Mineral species or alternative chemical elements	Measuring type of γ	γ	References
Clay aggregates	Kaolinite Illite Montrollinite α-Al_2O_3 α-Fe_2O_3			
	α-Al_2O_3	$\gamma_{0,BET}$	$1.6 \pm 0.5 \times 10^{-4}$	*Usher et al., 2002 (JGR)*
	α-Al_2O_3		$9.5 \pm 0.3 \times 10^{-5}$	
		γ_0	$\sim 1.0 \times 10^{-4}$	*Goodman et al., 2001 (J. Phys. Chem.)*
Calcite	Calcite Dolomite $CaCO_3$ CaO MgO			
	$CaCO_3$	$\gamma_{0,BET}$	$1.4 \pm 0.7 \times 10^{-4}$	*Usher et al., 2002 (JGR)*
Quartz	SiO_2			
	SiO_2	$\gamma_{0,BET}$	$< 1 \times 10^{-7}$	*Usher et al., 2002 (JGR)*
Authentic dust				
	Saharan dust	γ_0^{geom}	$(3.9\sim4.6) \times 10^{-3}$	
		γ_{BET}	$(4.1\sim5.0) \times 10^{-7}$	*Ullerstam et al., 2002 (Phys. Che. Chem. Phys.)*
	Chinese loess	$\gamma_{0,BET}$	$3.0 \pm 1 \times 10^{-5}$	*Usher et al., 2002 (JGR)*
Past studies				
			$5.0 \times 10^{-5} \sim 3.0 \times 10^{-4}$	*Dentener et al., 1996*
			$5.0 \times 10^{-3} \sim 5.0 \times 10^{-2}$	*(Song and Carmichael, 2001)*
			1.0×10^{-4}	*Tang et al., 2004b*
			$1.0 \times 10^{-7} \sim 1.0 \times 10^{-4}$	*Bauer et al., 2004*
			$3.0 \times 10^{-4} \sim 1.0 \times 10^{-1}$	*Liao et al., 2003*

Table 3.2 Continued. **(c)** $NO_2 \xrightarrow{dust} NO_3^-$

Three main mineral groups/ γ used in this study	Mineral species or alternative chemical elements	Measuring type of γ	γ	References
Clay aggregates	Kaolinite Illite Montrollinite α-Al_2O_3 α-Fe_2O_3			
	α-Al_2O_3	$\gamma_{0,t}$	9.1×10^{-6}	
		γ*	8.5×10^{-5}	*Underwood et al., 2001 (JGR)*
Calcite	Calcite Dolomite $CaCO_3$ CaO MgO			
	CaO	$\gamma_{0,t}$	2.2×10^{-5}	
		γ*	5.4×10^{-5}	*Underwood et al., 2001 (JGR)*
Quartz	SiO_2			
	SiO_2	$\gamma_{0,t}$	Too low (4.0×10^{-10})	
		γ*	-	*Underwood et al., 2001 (JGR)*
Authentic dust				
	Saharan dust	$\gamma_{0,t}$	R_G*1.0×10^{-6}	
		γ*	~ 2.0×10^{-5}	*Underwood et al., 2001 (JGR)*
	Chinese loess	$\gamma_{0,t}$	2.1×10^{-6}	
		γ*	4.4×10^{-5}	*Underwood et al., 2001 (JGR)*
Past studies				
			1.0×10^{-4}	*Dentener et al., 1996*
			1.0×10^{-4}	*Tang et al., 2004b*
			4.4×10^{-5}	*Bian and Zender, 2003*
			1.0×10^{-4}	*Liao et al., 2003*
			1.0×10^{-4}	*Martin et al., 2003*

Table 3.2 Continued. **(d)** $\mathbf{HNO_3} \xrightarrow{dust} \mathbf{NO_3^-}$

Three main mineral groups/ γ used in this study	Mineral species or alternative chemical elements	Measuring type of γ	γ	References
Clay aggregates	Kaolinite Illite Montrollinite α-Al_2O_3 α-Fe_2O_3			
	Kaolinite	γ_{init}	$(11 \pm 1.6) \times 10^{-2}$	*Hanisch and Crowley, 2001 (Phys. Chem.Chem.Phys.)*
Calcite	Calcite Dolomite $CaCO_3$ CaO MgO			
	$CaCO_3$	$\gamma_{init}^{geom.}$	$(18 \pm 4.5) \times 10^{-2}$	*Hanish and Crowley, 2001 (J. Phys. Chem.)v*
Quartz	SiO_2			
	SiO_2	$\gamma_{0,t}$	$(2.9 \pm 0.2) \times 10^{-5}$	*Underwood et al., 2001 (JPC)*
Authentic dust				
	Saharan sand	γ_{init}	1.36×10^{-1}	*Hanisch and Crowley, 2001 (Phys. Chem.Chem.Phys.)*
	Chinese loess	γ_{init}	1.71×10^{-1}	*Hanisch and Crowley, 2001 (Phys. Chem.Chem.Phys.)*
Past studies				
			1.0×10^{-3}	*Dentener et al., 1996*
			1.0×10^{-2}	*Tang et al., 2004b*
			1.0×10^{-1}	*Bauer et al., 2004*
			1.1×10^{-3}	*Bian and Zender, 2003*
			1.0×10^{-1}	*Liao et al., 2003*

Table 3.2 (a - d) also shows the uptake coefficients of dust samples from desert areas. X-ray microanalysis shows that Saharan sand that was used has a chemical composition of 80% Si, 1% Ca, 7% Fe, 10%Al, 8% K, 2% Mg, 1% Ti (*C. Galy-Lacaux* at the Laboratory of Aerology observatory Midi-Pyrenes in Toulouse, France, x-ray analysis) and China loess that was used has a chemical composition of 48% Si, 22% Ca, 10% Fe, 10%Al, 7% K, 2% Mg, 1% Ti (*M. Nishikawa* at the National Institute for Environmental studies in Tsukuba, Ibaraki, Japan, x-ray microanalysis) [*Michel et al.*, 2003]. Therefore, the dust samples from different source regions have differing chemical composition. In particular, amounts of Si, Ca, and Fe show large differences. It also indicates the difference in the mineralogical composition between two dust samples.

The direct measurement of O_3 uptake by calcite is not available even though first order loss rates (k = 1.9 × 10^{-3} /s) were measured by *Alebic-Juretic et al*. [2000]. It was converted to an uptake coefficient of 4.3 × 10^{-7} using k=(c/4) γ A_{dust} [O_3] where, c is molecular speed and the surface area density (cm^2/cm^3) of the substrate equals the product of BET surface area of the substrate (cm^2/g), A_{dust} and sample mass per reactor volume (g/cm^3), [O_3] *(Hanisch and Crowley*, 2003). Using the $\upsilon_{dep}=c\gamma/4$ (where, O_3 deposition velocity υ_{dep} and uptake coefficient γ), O_3 uptakes by calcareous soil or calcium carbonate were estimated in the range from 1.0 x 10^{-5} to 3.3 x 10^{-4} [*Galbally and Roy,* 1980; *Garland,* 1976]. This study uses the O_3 uptake coefficient by calcite of 2.0 x 10^{-4}. The O_3 uptakes by clay-aggregates were used with those by kaolinite (3.0 x 10^{-5}) which are lower than those by iron-oxides Fe_2O_3 (1.0 ~ 2.0 x 10^{-4}) by one order of magnitude. The O_3 uptakes by quartz were used as 5.65 x 10^{-5}.

The mechanism for SO_2 uptake is somewhat complicated. The SO_2 reaction with mineral aerosols is pH dependent. The sorption of SO_2 is followed by an oxidation of SO_2 or associated anion. The reaction of sulfide ion with O_3 is very fast in the aqueous phase. Compared with γ of individual mineral oxides or mineral compounds, the values of γ of calcite and clay are relatively high.

For the uptake of NO_2, the values of γ of kaolinite and dolomite are as large as 1.0×10^{-5}, whereas the values of γ of SiO_2 are negligibly small (1.0×10^{-10}). The HNO_3 uptake by kaolinite and dolomite is very high (10^{-3}~10^{-1}). The RH dependence of γ causes one order of difference in uptake coefficients [*Vlasenko et al.*, 2006]. It also causes the changes in morphology, as well as in hygroscopicity. Through the simple neutralization of the HNO_3 uptake on dust particles, the new nitrates are formed only on the carbonate-containing minerals shown in reactions (R3.1) and (R3.2)

$$HNO_3 + CaCO_3 \rightarrow Ca^{2+}CO_3^- + HNO_3^- \quad \text{(R3.1)}$$

$$HNO_3 + Ca_2NO_3^- + HCO_3^- \rightarrow Ca(NO_3)_2 + H_2O + CO_2 \quad \text{(R3.2)}$$

Because this is very fast reactions and the amount of HNO_3 is small (about 0.5 ppbv, I*ntex-NA*, 2004), the heterogeneous reaction occurs before the photolysis of HNO_3. It prevents NO or NO_2 from being provided for O_3 production.

3.2.4 Size-resolved mineralogical composition of dust particle aerosols

Three types of the compositional mixtures were built in terms of dust size distribution and uptake coefficients of dust particle aerosols. These three models are depicted in Figure 3.3. In Model 1, a single uptake coefficient and the four different dust

size distributions were used in order to examine the effect of dust size distribution on $k_{loss,j}$. The reference case used in this study is the D87 size distribution and the uptake coefficients from *Dentener et al.* [1996]. The uptake coefficients of two different authentic dust sample, China loess and Saharan soil, are used in calculation of $k_{loss,j}$ of the Model 1.

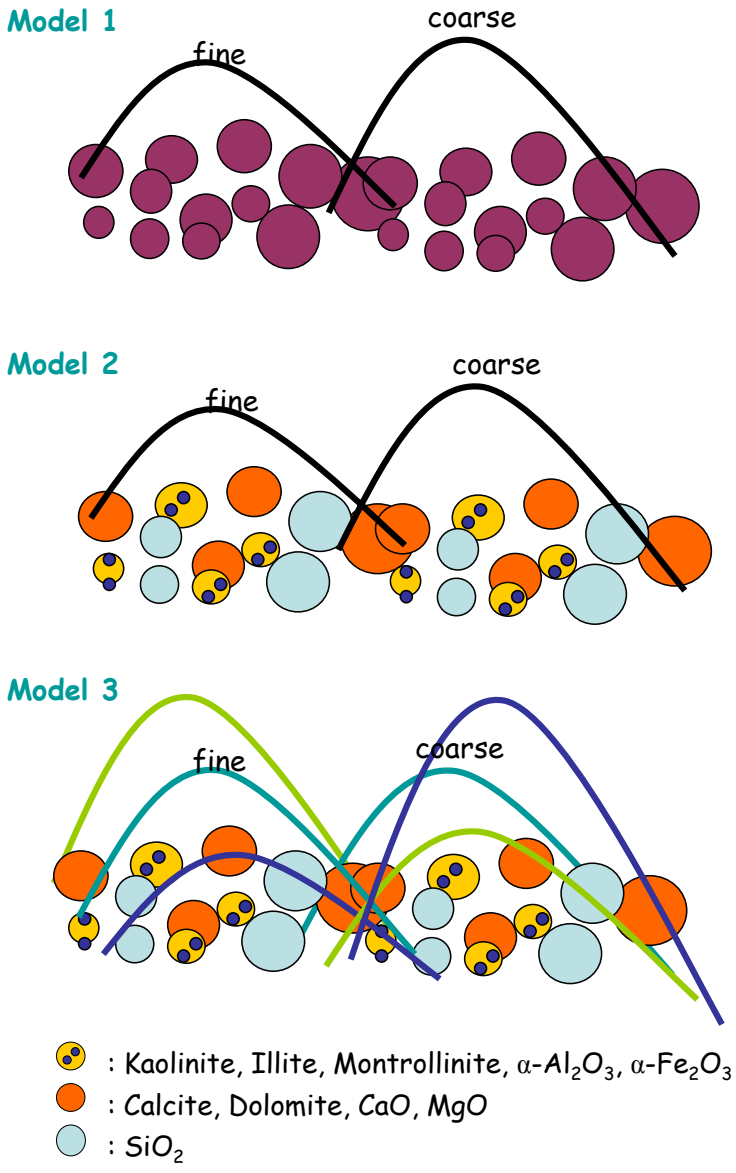

Figure 3.3 Three types of size-resolved mineralogical composition models.

The Model 2 consists of a mixture of three mineral species with their own uptake coefficients and mass fraction. The mass fraction of individual mineral species was selected according to the amount of calcite present. The mass fractions of calcite reported in the literature vary from a few percent to more than 40%. The African dust contains 1-15% of calcite [*Avila et al*., 1997; *Gomes and Gillette,* 1993; *Caquineau et al.*, 1998; *Claquin et al.*, 1999]. Downwind of Africa, dust contains 4-9% of calcites [*Glaccum and Prospero*, 1980], while it contains more than 20% in the Sahel region [*Sharif*, 1995]. For Asian dust, *Trochkine et al.* [2003] reported about 13 - 41% of Ca-rich particles in dust sampled in Dunhuang, China. The amount of CO_3^{-2} comprises 8% over Xi'an near Asian dust source region [*Cao et al.*, 2005]. *Shen et al.*[2006] reported that Asian dust contains 10% of calcite, 20% of quartz, and 70% of clay minerals in Dunhuang. *Shi et al.* [2005] measured 11 - 13% of calcite, 29 - 30% of quartz, and 57 - 60% of clay minerals in Beijing during a severe dust storm episode. Therefore, 0% and 50% of calcite were chosen as the minimum and maximum mass fractions. The rest of the mass was made up of either iron oxide-clay aggregates or quartz, or both. The 100% of calcite was chosen as an extreme case. Table 3.3 (a) shows the mass fractions of the three main mineral species for a mixture used in this study. This mineralogical composition of a dust mixture is applied to each size mode of dust size distributions. Hence three main mineral species have the same size distributions for a given dust size distribution.

In Model 3, a mixture of three mineral species with the mass partitioning between fine and coarse modes was used as shown in Table 3.3 (b). The mass partitioning was done by increasing fine mode mass fractions such as 10%, 50%, and 90% for the five

mass fractions used Model 2. This experiment was designed to examine the importance of the differing mineralogical composition in fine and coarse modes on the value of $k_{loss,j}$.

Table 3.3 (a) Mass Fraction of the Mineralogical Species for Model 2

Size-resolved	m_{cal}	m_{agg}	m_{qtz}
Ca0A50Q50	0	50	50
Ca50A50Q0	50	50	0
Ca50A0Q50	50	0	50
Ca50A25Q25	50	25	25
Ca100A0Q0	100	0	0

m_{cal}, m_{agg}, and m_{qtz} denote the mass fraction of calcites, clay aggregates, and quartz, respectively.

Table 3.3 (b) Mass Fraction of the Mineralogical Species for Model 3

Size-resolved	Fine			Coarse		
	$m_{agg,f}$	$m_{cal,f}$	$m_{qtz,f}$	$m_{agg,c}$	$m_{cal,c}$	$m_{qtz,c}$
Ca0A50Q50_F10	5	0	5	45	0	45
Ca0A50Q50_F50	25	0	25	25	0	25
Ca0A50Q50_F90	45	0	45	5	0	5
Ca50A50Q0_F10	5	5	0	45	45	0
Ca50A50Q0_F50	25	25	0	25	25	0
Ca50A50Q0 _F90	45	45	0	5	5	0
Ca50A0Q50_F10	0	5	5	0	45	45
Ca50A0Q50_F50	0	25	25	0	25	25
Ca50A0Q50_F90	0	45	45	0	5	5
Ca50A25Q25_F10	2.5	5	2.5	22.5	45	22.5
Ca50A25Q25_F50	12.5	25	12.5	12.5	25	12.5
Ca50A25Q25_F90	22.5	45	22.5	2.5	5	2.5
Ca100A0Q0_F10	0	10	0	0	90	0
Ca100A0Q0_F50	0	50	0	0	50	0
Ca100A0Q0_F90	0	90	0	0	10	0

$m_{cal,f}$, $m_{agg,f}$, and $m_{qtz,f}$ denote the mass fraction in fine mode of calcites, clay aggregates, and quartz, respectively.

$m_{cal,c}$, $m_{agg,c}$, and $m_{qtz,c}$ denote the mass fraction in coarse mode of calcites, clay aggregates, and quartz, respectively.

3.3 Results

The above three models were used to investigate the range of $k_{loss,j}$, the effect of dust size distribution, the relative contribution of individual mineral species to $k_{loss,j}$, and the sensitivity of $k_{loss,j}$ to mass partitioning between fine and coarse modes. The heterogeneous reactions of O_3, SO_2, NO_2, and HNO_3 on the dust particle surfaces were considered. In the same dust loading condition, two first order loss rates of those gases, $k_{loss,j}$ and J-values, were compared.

Figure 3.4 shows the effect of dust size distribution on $k_{loss,j}$ calculated with Model 1. The values of $k_{loss,j}$ were calculated with a single uptake coefficient, $\gamma^*_{j,}$ and four different dust size distributions (C04, D87, O98, and B02). Open symbols denote $k_{loss,j}$ calculated with γ_j^* of the reference case. The filled squares and the filled triangles show the values of $k_{loss,j}$ calculated with γ^*_j of Saharan soil and China loess, respectively. The $k_{loss,j}$ using γ^*_j of authentic dust samples is smaller than $k^{ref}_{loss,j}$ for the O_3, SO_2, and NO_2 loss while it is larger than $k^{ref}_{loss,j}$ for the HNO_3 loss. The B02 size distribution and C04 size distribution give the smallest and largest values of $k_{loss,j}$, respectively. The difference between maximum and minimum values of $k_{loss,j}$ is a factor of 5. However, it is a factor of 10 for the HNO_3 loss reaction using γ^*_j of authentic dust samples. The differences between the values of $k_{loss,j}$ using γ^*_j of two authentic dust samples indicate that the mineralogical composition of the two dust samples is different.

Figure 3.5 shows the relative contribution of individual mineral species to $k_{loss,j}$ calculated with Model 2. The heterogeneous loss rates on the mineral species, m is called $k_{loss,j,m}$. The behavior of $k_{loss,j,m}$ due to the mass fraction of mineral species are similar for the four dust size distributions. The difference between maximum and minimum values

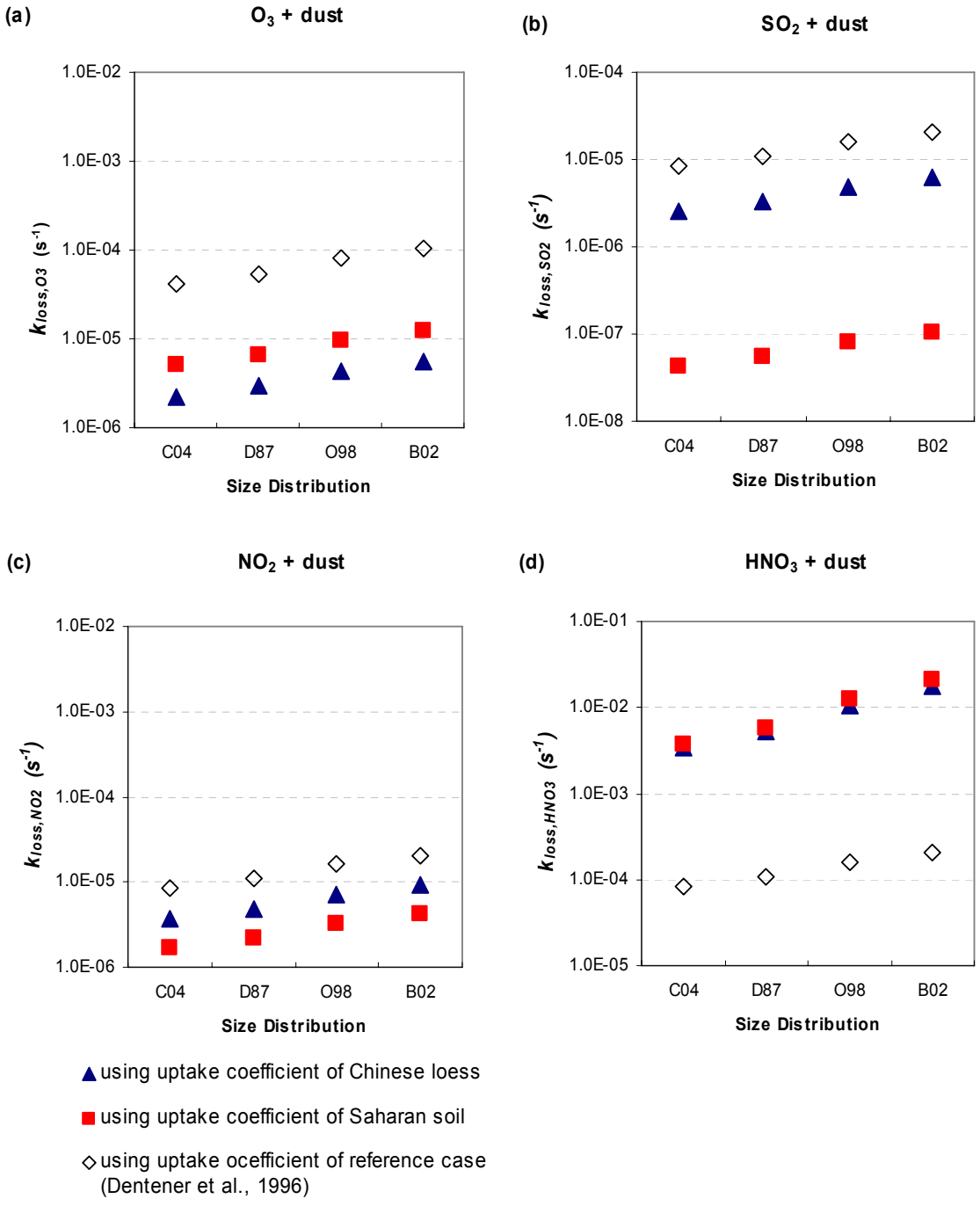

Figure 3.4 The values of $k_{loss,j}$ of O_3, SO_2, NO_2, and HNO_3 using the uptake coefficients of authentic dust sample and reference case for four different dust size distributions for Model 1.

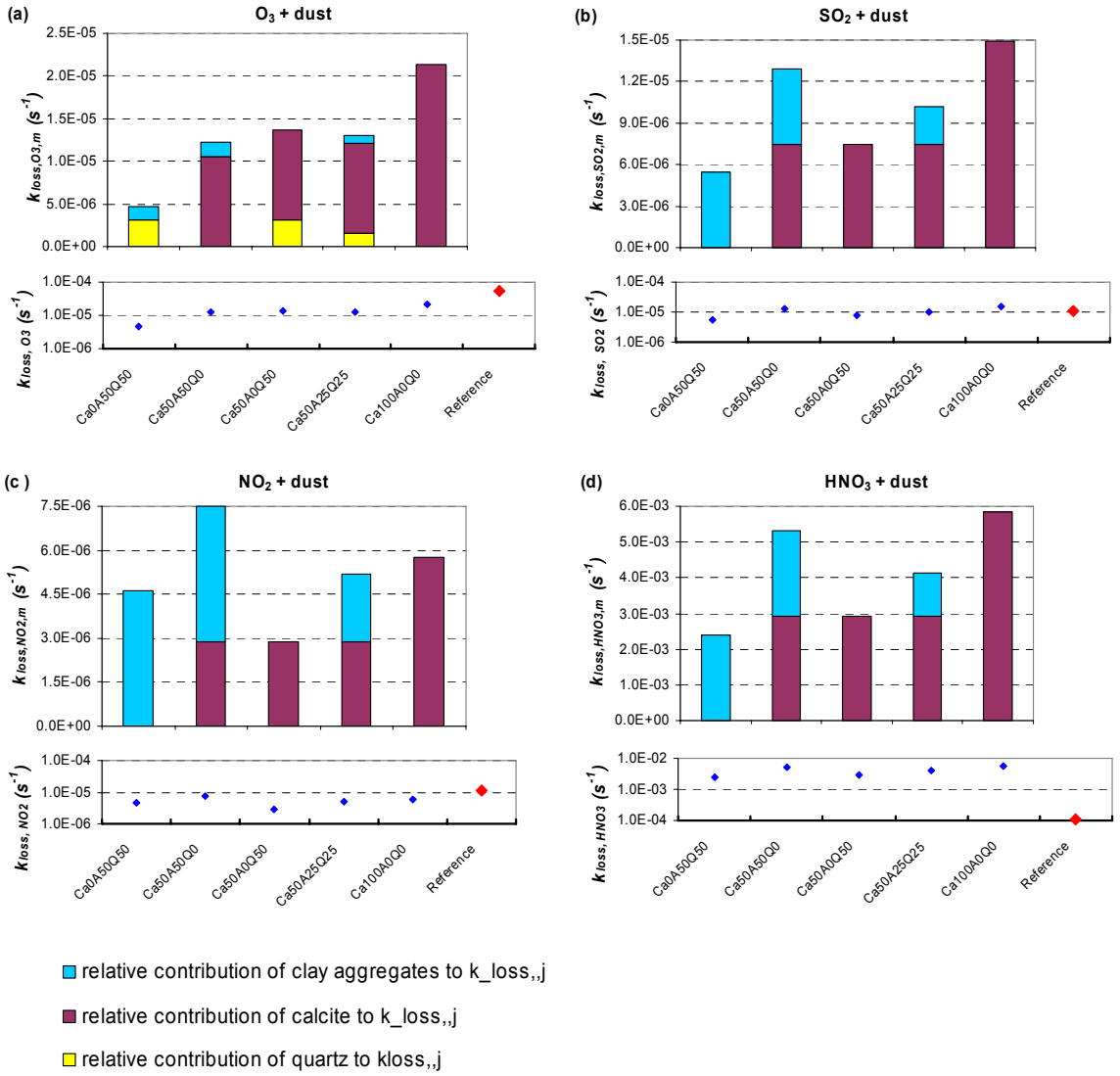

Figure 3.5 The values of $k_{loss,,j,\ m}$ of O_3, SO_2, NO_2, and HNO_3 for the selected mass fractions of three mineral species using D87 dust size distribution for Model2.

of $k_{loss,j}$ is a factor of 4.5 in the O_3 loss reaction. The values of $k_{loss,j}$ are less than the values of $k^{ref}_{loss,j}$ for the O_3 and NO_2 loss reactions, while they are larger than the values of $k^{ref}_{loss,j}$ for the HNO_3 loss reaction. The $k_{loss,j}$ is similar to $k^{ref}_{loss,j}$ for the SO_2 loss reaction.

The $k_{loss,j}$ of Model 2 is determined by the relative values of $k_{loss,j,m}$ of individual minerals with respect to the values of $k_{loss,j,m}$ of other minerals in a mixture. The $k_{loss,j,m}$ is controlled mainly by the values of $\gamma_{j,m}$ rather than by the mass fraction of mineral species, m. The values of $k_{loss,j}$ do not follow an amount of calcite except in an O_3 loss. For O_3 loss, calcite is the most important species in determining $k_{loss,j}$. Clay aggregates are as important as calcite in $k_{loss,j}$ for SO_2 and HNO_3 loss and the most important species in $k_{loss,j}$ for NO_2. In turn, quartz reduces the value of $k_{loss,j}$ of SO_2, NO_2, and HNO_3 when it is included in a dust mixture.

Figure 3.6 shows the effect of mass partitioning on $k_{loss,j}$ for Model 3. We examined the values of $k_{loss,j}$ for the differing mineralogical composition between fine and coarse mode. The mass partitioning was taken by increasing mass fraction in fine mode such as 10%, 50%, and 90%. The behaviors of $k_{loss,j}$ with respect to mass partitioning are similar among different dust size distributions. For O_3 loss, the values of $k_{loss,j}$ are controlled by the amount of calcites. For NO_2, the uptake coefficient of clay aggregates is the largest and that of the calcites is the second largest. Hence $k_{loss,j}$ of the dust mixture of Ca50A50Q0 is the largest and $k_{loss,j}$ of the dust mixture of Ca50A0Q5is the smallest. For SO_2 and HNO_3, the mass fraction of calcites is the most important in the values of $k_{loss,j}$, however, a sum of mass fractions of clay aggregates and calcite is also important to the

values of $k_{loss,j}$. Hence, the ratio of the values $k_{loss,j}$ to fine mode mass fractions is unique over five mass fractions of mineral species.

The larger the fine mode mass fraction is the larger $k_{loss,j}$. In other words, the smaller the coarse mode mass fraction is the larger $k_{loss,j}$. The rate of change in $k_{loss,j}$ against the fine mode mass fraction is proportional to the magnitude of $k_{loss,j}$, which is determined mainly by mineral species with large uptake coefficients. Therefore, the HNO_3 loss is most favorable in the fine mode among four gaseous loss reactions, which is the distinct effect of size-resolved mineral species on the heterogeneous loss rates. This is compatible to the contour plot of $k_{loss,j}$ in Figure 3.1(b). The largest values of $k_{loss,j}$ appear when the uptake coefficient is larger than 0.1 and the radius of particles is between 0.1 to 1.0μm. If the RH dependence of the uptake coefficient is considered, the HNO_3 uptake coefficients by calcite are higher than 1.0×10^{-1} [*Vlasenko et al.*, 2006]. It is possible that the formation and growth of soluble mineral species such as $Ca(NO_3)_2$ in the fine mode lead to act as dust CCN.

Figure 3.7 shows the comparison between the values of $k_{loss,j}$ for Model 3 and J-values. For the 1-2 km dust layer with the C04 size distribution and a moderate dust loading of 1500 μg/m^3 as used in Chapter 2, the difference in J-values due to mineralogical composition is much less (by more than a factor of 3) than that in $k_{loss,j}$. $J[NO_2]$ is larger than $k_{loss,NO2}$ by 2-3 orders of magnitude. $J[HNO_3]$ is less than $k_{loss,HNO3}$ by 3~5 orders of magnitude. The $k_{loss,O3}$ is comparable to $J[O_3(^1D)]$ in the morning and afternoon. Even though the tropospheric ozone concentration is not determined simply by a single process, the direct ozone uptake by mineral dust is as important as its photo-dissociation.

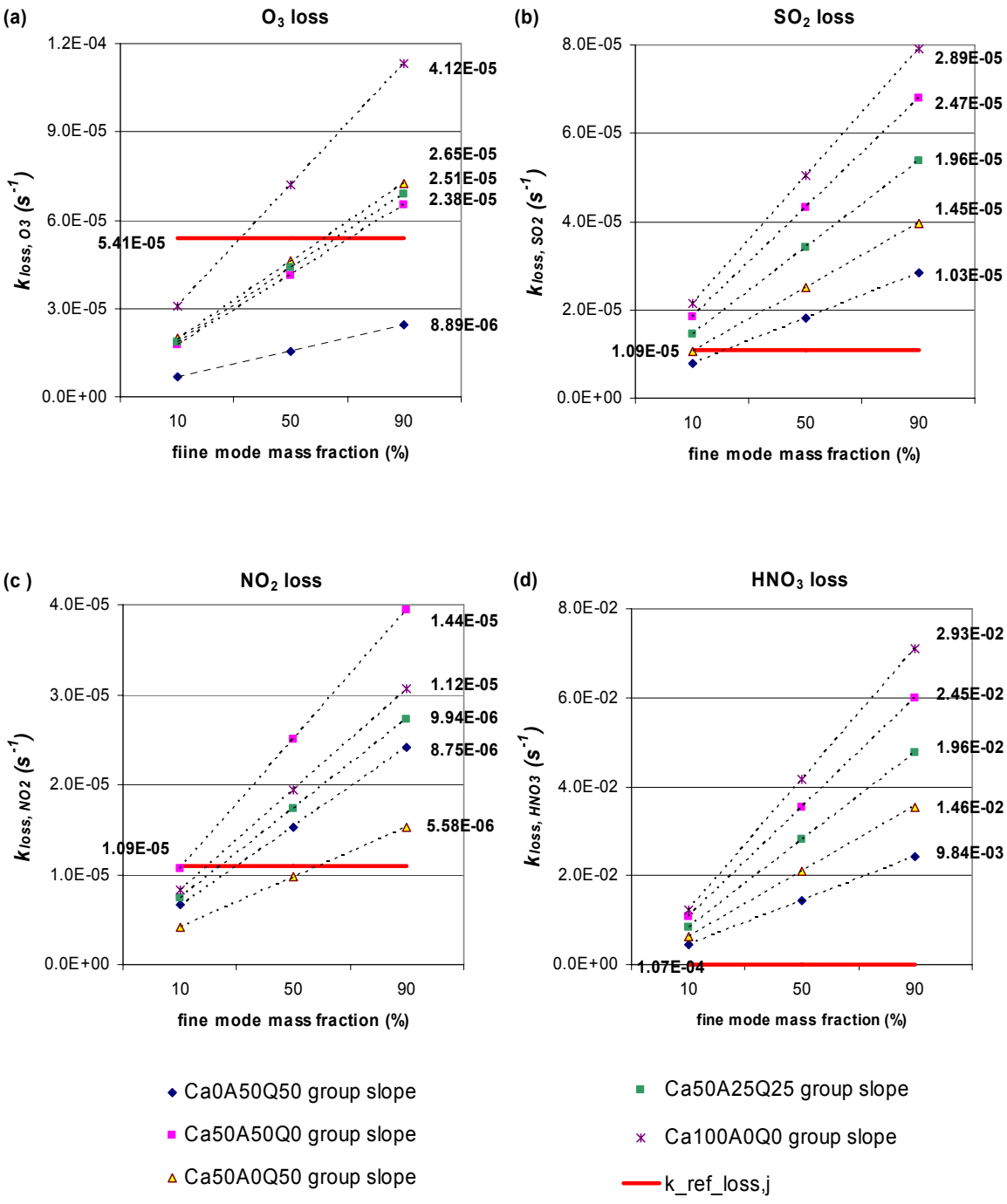

Figure 3.6 The values of $k_{loss,j}$ calculated with Model 3.

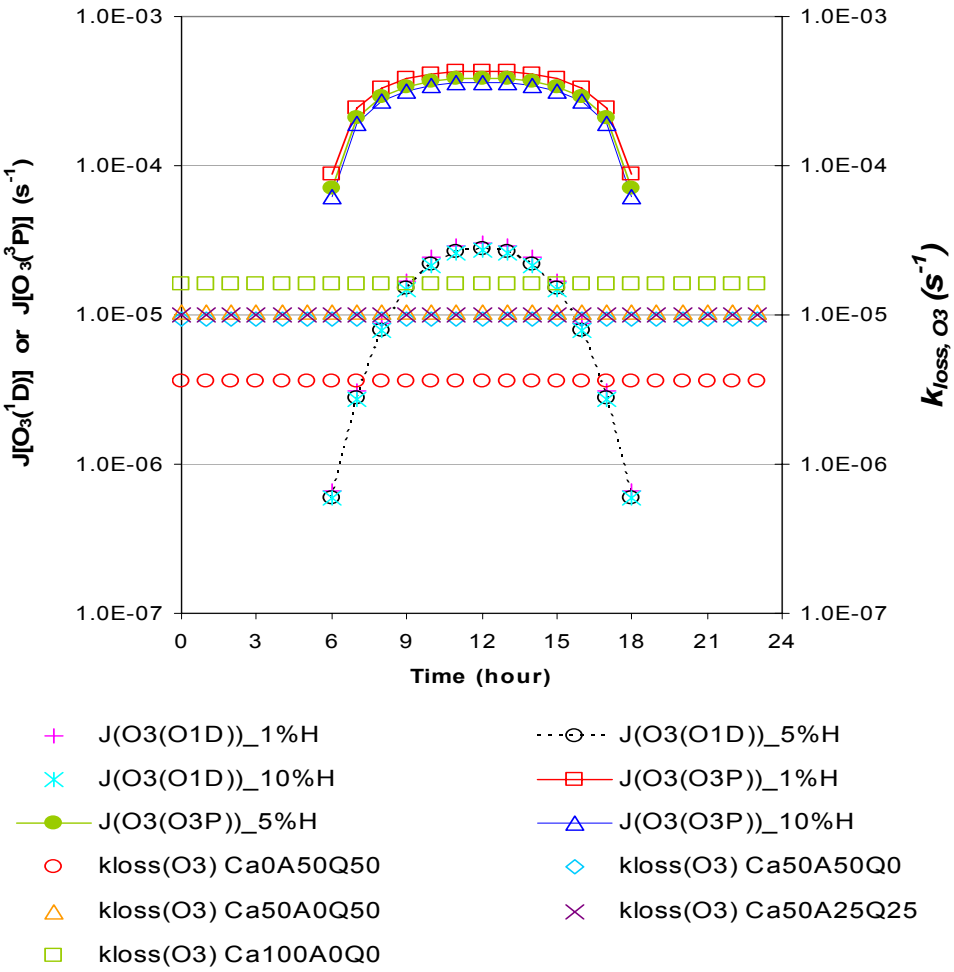

Figure 3.7 Comparison between the values of $k_{loss,O3}$ and $J[O_3(O^1D)]$ and $J[O_3(O^3P)]$ (see text for details).

3.4 Conclusions

A conceptual model of the size-resolved mineralogical composition was built in order to study how the size and composition of dust particles affect heterogeneous loss rates. The new findings of this chapter are as follows:

1. For dust particles with one fixed uptake coefficient, the $k_{loss,j}$ changes by a factor of five to ten between maximum and minimum values due to the four different dust size distributions. The values of $k_{loss,j}$ are larger when the dust size distribution is shifted to the fine mode.

2. For dust particles as a mixture of three mineral species, the $k_{loss,j}$ is determined by the relative contribution of individual mineral species. The $k_{loss,j}$ strongly depends on the relative magnitude of the uptake coefficients rather than on mass fraction of mineral species in a mixture. In only a heterogeneous loss of O_3, the mass fraction of calcites is decisive to $k_{loss,j}$.

3. As the fine mode mass fraction of mineral dust increases, the $k_{loss,j}$ increases because the reaction site for heterogeneous loss increases. The larger the $k_{loss,j}$, the larger the rate of change in $k_{loss,j}$ over fine mode mass fractions. The distinct effect of size-resolved mineral species on the heterogeneous loss rates is proportional to the fine mode mass fractions of mineral species with high uptake coefficients.

4. Due to different mineralogical composition, the ranges of $k_{loss,j}$ are much larger than those of J-values by a factor of three in the same aerosol(dust) loading conditions. It is noteworthy that the direct O_3 uptake by dust particles has a significant effect on tropospheric ozone reduction.

The results of $k_{loss,\ j}$ and J-values that take a consideration of the size and composition of mineral dust aerosols can be used to estimate more adequately the relative roles of mineral dust aerosols in the tropospheric photochemistry through both photolysis and heterogeneous reactions. This is discussed next in Chapter IV.

Chapter IV

THE EFFECTS OF THE SIZE-RESOLVED MINERALOGICAL COMPOSITION OF DUST PARTICLES ON PHOTOCHEMICAL SPECIES IN MARINE ENVIRONMENTS

4.1 Introduction

The effects of the size and the composition of mineral dust aerosols on photolysis rates and heterogeneous loss rates were thoroughly examined in Chapters 2 and 3, respectively. In this chapter, we investigate the combined effect of these processes as well as their relative importance through a series of modeling experiments performed with the newly developed DUST-CHEM model.

Currently, there is a high uncertainty in the relative importance of photolysis and heterogeneous loss rates caused by dust. *Tang et al.* [2004b] showed that O_3 heterogeneous uptake decreased background O_3 by 20 ppbv and NO_2 production during ACE-Asia and that most chemical species were affected more by the heterogeneous reaction than by photolysis. However, OH decreases by 20%, mainly through photolysis. Some studies show a 60% decrease in global OH due to the radiative effects of mineral dust, twice as much as the decrease due to chemical effects on the Sahara Desert [*Martin et al.*, 2003]. *Bian and Zender* [2003] demonstrated that the coupling of heterogeneous reactions and photolysis weakened the impact of dust (i.e., a reduction of 20% of the ozone) because ozone and odd-nitrogen concentration were perturbed in opposite directions. They also estimated that although heterogeneous effects were four times as large as radiative effects, their estimation involved many uncertainties such as the dust burden, the dust size distribution, refractive indices, and the gaseous uptake coefficients of mineral dust aerosols. Therefore, estimations of the impact of dust on photochemistry

spanned a wide range, between 5% and 40% of ozone reduction; it has also been suggested that the effect of the heterogeneous reaction is larger than that of photolysis by a factor of 0.5 to 4. However, because of an inconsistent treatment of size distributions and composition of dust particles, the roles of photolysis and heterogeneous loss were not adequately compared.

The results presented in Chapters 2 and 3 demonstrated that photolysis rates and heterogeneous loss rates are strongly controlled by size-resolved mineralogical composition through spectral light absorption and alkalinity. We found that differences in the size and the composition of mineral dust alter the vertical profile and the diurnal cycle of J-values and that the dust size distribution is as important as the mineralogical composition of dust particles in the reduction of J-values at the surface. Therefore, J-values may increase or decrease due to the position of the dust layers. For heterogeneous reactions, the overall heterogeneous loss rate, $k_{loss,j}$ is larger when the dust size distribution shifts to the fine mode. Because of the different mineralogical compositions, the ranges of $k_{loss,j}$ are much larger than those of the J-values by a factor of three in the same aerosol (dust) loading conditions. In particular, the $k_{loss,O3}$ is as significant as $J[O_3(O^1D)]$. If the microphysical and chemical characteristics of mineral dust aerosols produce such significant changes in photolysis and heterogeneous reaction rates, we need to re-examine the effects of mineral dust aerosols on tropospheric photochemistry with a consistent treatment of dust particles in these two mechanisms.

The goals of this chapter are to investigate how the size-resolved mineralogical composition of dust aerosols affects tropospheric photochemistry and to determine their relative roles. We consider dust aerosols as an external mixture of main mineral species such as iron oxide-clay aggregates, calcite, and quartz. The size distributions, ranges in the amount of iron oxide in clay minerals, and the amount of carbonate compounds are the same as those we used in the photolysis and heterogeneous studies (Chapters 2 and 3).

A new photochemistry model, DUST-CHEM, was developed to meet the goals of this study. Section 4.2 provides a brief description of the structure of the DUST-CHEM, Section 4.3 discusses the selection of aerosol and gas phase species and dust loading scenarios, and Section 4.4 presents the main results of this study. Section 4.5 summarizes the findings of this chapter.

4.2 Approach

4.2.1 One-dimensional photochemistry model DUST-CHEM

In this study, we have designed the DUST-CHEM model that enables the examination of the impact of mineral dust aerosols on the atmospheric photochemical system through photolysis and heterogeneous loss. DUST-CHEM is a one-dimensional chemical model that includes emission, deposition, vertical transport, and chemistry processes. Each of the chemical species in the model satisfies mass conservation. The time rate of concentration changes of gaseous species is the sum of the vertical transport, the chemical production, and loss:

$$\frac{\partial \boldsymbol{C}}{\partial \boldsymbol{t}} = \frac{\partial}{\partial \boldsymbol{t}}\left(\boldsymbol{K}_z \frac{\partial \boldsymbol{C}}{\partial \boldsymbol{z}} \right) + \boldsymbol{E} + \boldsymbol{P} - \boldsymbol{L}\boldsymbol{C}\,, \tag{4.1}$$

where C is the concentration, K_z is the vertical eddy diffusion coefficient for mass transport, E is the emission term, and P and L are the chemical production and loss terms, respectively. The profile of the eddy diffusion coefficients was borrowed from *Thompson and Lenschow* [1984]: 1.0×10^3 cm^2/s in the surface marine boundary layer (0 to 50m), 7.0×10^5 cm^2/s in the marine boundary (mixed) layer (50m to 500m), and 1.7×10^4 cm^2/s in the free atmosphere (above 500m). The boundary conditions in the equation are top fluxes through the upper boundary at a height of 4km; at the lower boundary, the vertical flux equals deposition

$$\mathbf{K_Z}\frac{\partial \mathbf{C}}{\partial \mathbf{z}} = \mathbf{v_d C} \quad , \tag{4.2}$$

where v_d is the dry deposition coefficient.

Chemical mechanisms contained 77 species, 145 gas-phase reactions, thirteen photolysis reactions, and four heterogeneous reactions. The numerical method used for solving the chemical reactions was the Sparse-Matrix-Vectorized (SMV) Gear code [*Jacobson*, 1994]. The SMV Gear code computes a stiff system of reaction equations by reordering a predictor matrix, eliminating multiplication by zero, and vectorizing the inner-nested loop. The chemical reactions include O_3-NO_x-HO_x-CH_4 chemistry as well as sulfur chemistry. Gaseous kinetic rate constants are taken from *Sander et al.* [2006] and *Lucas* [2004]. The chemical reaction list is shown in Appendix B. Initial gaseous concentrations (taken from *Thompson et al*., 1993), deposition velocities, emission rates, and the top fluxes of several important species are presented in Appendix C. The fluxes of NO, NO_2, NO_3, and HNO_3 from the top are supplied during the day, and the fluxes of DMS from the sea surface were considered. NO sea-to-air fluxes are prescribed. The major source of boundary layer NO is the weak oceanic outgassing of dissolved NO formed from the photodissociation of the nitrite (NO_2^-) radical [*Treinin and Hayon*, 1970; *Bonneau*, 1987]. Thus, nitrite is assumed to be of photochemical origin:

$$NO_2^- + H_2O + h\nu \rightarrow NO + OH + OH^- \, . \tag{4.3}$$

The DUST-CHEM incorporates the J-values and heterogeneous loss rates that reflect mineral dust aerosols in the photochemistry models. The physics block includes interfaces that incorporate J-values and heterogeneous loss rates according to the position of the sun and altitude. The thirteen photolysis rates are $J[O_3(O^3P)]$, $J[O_3(O^1D)]$, $J[NO_2]$,

$J[NO_3(NO_2)]$, $J[NO_3(NO)]$, J[HONO], $J[N_2O_5]$, $J[HNO_3]$, $J[HO_2NO_2]$, $J[H_2O_2]$, $J[CH_3OOH]$, $J[CH_2O(HCO)]$, and $J[CH_2O(CO)]$. The photolysis rates are computed in each layer as a function of time. The heterogeneous loss rates of O_3, SO_2, NO_2, and HNO_3 are computed in each vertical in the presence of dust.

The DUST-CHEM model was set up for April 17, 2001, in the northwestern Pacific Ocean (132ºE and 34ºN) to simulate a representative diurnal sun cycle for the ACE-Asia time period. The 1976 US standard atmosphere is used. The vertical domain is 0km to 4km, and the vertical resolution is 500m. The time step for chemistry is fifteen minutes, and the total integrated time is seven days. Appendix D presents the diurnal variation of important photochemical species such as O_3, OH, $O(^1D)$, $O(^3P)$, CH_3OOH, H_2O_2, NO, NO_2, NO_3, HNO_3, HNO, HO_2NO_2, DMS, MSA, SO_2, and H_2SO_4 at the surface layer in the clean marine and polluted marine (dust-free) atmosphere.

4.3 Selection of aerosol- and gas-loading scenarios for the DUST-CHEM modeling experiments

4.3.1 Selection of dust mixtures

To investigate the relative importance of the dust properties in dust-chemistry interactions, we perform sensitivity tests by selecting the upper and lower values of the size distribution, light absorption, and the alkalinity of mineral dust aerosols. We select the C04 and B02 size distributions (see Chapter 2). The C04 is shifted to a coarse mode whereas the B02 is shifted to a fine mode. We found (see Chapter 2) that most of the J-values considered in this study were the smallest in the case of B02 and the largest for C04. However, heterogeneous loss rates, $k_{loss,j}$ were the smallest for C04 and the largest for B02.

We consider low-absorbing dust (H1) composed of 99% kaolinite and 1% hematite (by volume mixing in clay aggregates) and strong absorbing dust (H10)

composed of 90% kaolinite and 10% hematite. As demonstrated in Chapter 2, changes in the J-values relative to those of aerosol-free conditions are much larger for H10 dust than for H1 dust, while the J-values are the smallest for H10 dust and the largest for H1 dust. The H1 and H10 dusts are also used for the sensitivity of photochemical species to the mixing state of dust-BC mixtures.

Furthermore, we consider a low alkali dust composed of 0% calcite and a high alkali dust composed of 50% calcite. These values represent the lower and upper values of calcite reported in the literature [*Avila et al*., 1997; *Caquineau et al.*, 1998; *Claquin et al.*, 1999; *Sharif*, 1995; *Trochkine et al.,* 2003; *Shi et al.,* 2005; *Shen et al.,* 2006]. For the heterogeneous reactions analyzed in this study, the values of $k_{loss,j}$ are smallest in low (no) alkali dust and the largest in high alkali dust (see Chapter 3).

In order to characterize the low/high values of the light absorption and alkalinity of dust aerosols, we construct several dust mixtures by varying the mass fraction of the three mineral species and iron oxide contents in clay aggregates. Table 4.1 shows the composition and size distribution of considered dust mixtures as well as their mixing state with other aerosols. We use the dust mixture with the C04 size distribution and the Ca0A50(H1)Q50 composition as a reference case. In all the cases, the mass fraction of clay aggregates was fixed at 50%, which is a representative mass fraction of clay aggregates in mineral dust [*Shi et al.*, 2005; *Lafon et al.*, 2006].

In addition to the reference case, four types of dust mixtures were constructed and tested. They were built by varying the amount of iron oxides in the clay aggregates and the mass fraction of calcite in the mixture, considering the C04 size distribution: low absorbing dust with low alkalinity (Ca0A50(H1)Q50), low absorbing dust with high alkalinity (Ca50A50(H1)Q0), high absorbing dust with low alkalinity (Ca0A50(H10)Q50), and high absorbing dust with high alkalinity (Ca50A50(H10)Q0). Overall, the J-values and $k_{loss,j}$ are the largest for Ca50A50(H1)Q0 and the smallest for

Ca0A50(H10)Q50 (see Chapters 2 and 3). For each type of dust mixture, we investigate the relative importance of photolysis and heterogeneous loss on photochemistry in clean marine conditions by including either photolysis or heterogeneous loss, or both mechanisms.

4.3.2 Selection of aerosol and gas loading scenarios

We built several cases of vertical distributions (loading scenarios) of aerosol and gases considering two types of marine environments: clean and polluted. The two marine environments have differing vertical distributions of aerosols and gas species from 0 to 4km.

In the clean marine environment, gaseous concentrations were constrained using the observation data of *Thompson et al.* [1993]. The aerosol species in this condition consists of sea salt with a concentration of 68.87 $\mu g/m^3$ and WSA with a concentration of 3.0$\mu g/m^3$. Sea salt is assumed to be present only in the MBL while WSA is assumed to be present up to 4km with its concentration decreasing exponentially with altitude. In the clean marine environment, we consider two scenarios, NO_DUST and DUST_ONLY, as shown in Table 4.2. We consider NO_DUST the reference case. In the DUST_ONLY case, a dust layer from 1 to 3km is added to the clean marine environment. For the analysis of the sensitivity of photochemical species to dust characteristics, the dust mixtures are assumed to be present in the DUST_ONLY case

Table 4.1.The Size Distribution and Composition of Considered Dust Mixtures

Dust Characteristics	Composition_Size	Light Absorption	Alkalinity	Mixing
Reference dust aerosol	Ca0A50(H1)Q50_C04	Low	Low	×
Size distribution	Ca0A50(H1)Q50_**B02**	Low	Low	×
Light absorption	Ca0A50(**H10**)Q50_C04	**High**	Low	×
Alkalinity	**Ca50**A50(H1)Q0_C04	Low	**High**	×
	Ca50A50(**H10**)Q0_C04	**High**	**High**	×
Mixing state	Ca0A50(**H1**)Q50_C04	Low	Low	○
	Ca0A50(**H1**)Q50_C04	Low	Low	○
	Ca0A50(**H10**)Q50_C04	High	Low	○
	Ca0A50(**H10**)Q50_C04	High	Low	○

× indicates not considered
○ indicates considered

Table 4.2 Aerosol and Gas Species Loading Scenarios

Scenario Name	**NO_DUST**	**ONLY_DUST**	**MIXED_DUST**
Gaseous loading	Clean marine	Clean marine	Polluted marine
Aerosol loading / Vertical layer			
2-3 (km)	WSA	WSA, DUST	WSA, DUST, BC, OC
1-2 (km)	WSA	WSA, DUST	WSA, DUST, BC, OC
0-1 (km)	Sea salt, WSA	Sea salt, WSA	Sea salt, WSA, BC, OC

4.4 Analysis of diurnal cycles and vertical profiles of photochemical species

Using the selected dust mixtures, we investigated how dust properties such as size distribution, light absorption, alkalinity, and mixing state with other aerosol and gaseous species affect photochemical oxidant fields. The diurnal variation of the vertical profiles of several important species was calculated through photolysis, heterogeneous reaction, and both mechanisms. In order to examine the effect of the size and composition of dust particles, gaseous concentration through each process was investigated in the DUST-ONLY. The reference cases were denoted as follows: *(Ca0A50(H1)Q50_C04)*$_p$, relatively low light absorption, relatively low (no) alkalinity, and the size distribution shifted to the coarse mode for the test of the effect of photolysis; *(Ca0A50(H1)Q50_C04)*$_{\boldsymbol{h}}$ for the test of the effect of heterogeneous loss effect; and *(Ca0A50(H1)Q50_C04)*$_{\boldsymbol{b}}$ for the test of both effects. For the sensitivity to the dust size distribution, we use the *(Ca0A50(H1)Q50_**B02**),* which has the same properties as the reference dust mixture, except for the dust size distribution of B02. We also use the *(Ca0A50(**H10**)Q50_C04)*, which has H10 dust for the sensitivity to light absorption and the *(**Ca50**A50(H1)Q50_C04)*, which has the mass fraction of calcites of 50% relative to the reference cases for the sensitivity to alkalinity.

In this chapter, six photochemical species are investigated: O_3, OH, NO, NO_2, HNO_3, and SO_2. They include the major products of photolysis analyzed in Chapter 2 such as OH and NO, and the species related to the heterogeneous uptake discussed in Chapter 3 such as O_3, NO_2, SO_2, and HNO_3. Here, we mainly focus on the shape of the vertical profiles of those species and the variation of profiles due to dust properties. Figures 4.1-4.6 show the vertical profiles of O_3, OH, NO, NO_2, HNO_3, and SO_2, each computed for the clean marine environment both at noon (a-c) and at midnight (d-f), averaged over seven days. Figures (a, d) show the vertical profiles of the gaseous species

considering only photolysis, Figures (b, e) consider only heterogeneous loss, and Figures (c, f) consider both photolysis and heterogeneous loss. The dotted lines indicate the vertical profiles of gaseous species in dust-free conditions (NO_DUST case), and the lines with symbols are for the dust-laden condition (DUST_ONLY case). In DUST_ONLY, the photolysis rates are reduced relative to those in the NO_DUST case. Therefore, the sensitivity tests consider light absorption by dust particles and dust size distribution through photolysis only, alkalinity, and dust size distribution through heterogeneous only, and light absorption, alkalinity, and size distribution through both mechanisms. The blue-filled diamond with a dashed line indicates the vertical profiles of the average concentration from observations during PEM tropics-B.

Figure 4.1 shows that O_3 decreases with altitude in the clean marine condition. The vertical profiles of O_3 between noon and midnight do not significantly differ. Through photolysis, the dust layer increases O_3 concentration relative to the clean marine condition, the largest increase occurring at the surface. Through heterogeneous loss, a reduction in the ozone concentration is distinct in the dust layer, the maximum reduction occurring in the middle of the dust layer. Through both mechanisms, the vertical profiles of the ozone concentration are similar to those in the heterogeneous-only process. Therefore, the direct uptake of O_3 is the dominant process of the two mechanisms even though the magnitude of $J[O_3(O^1D)]$ or $J[O_3(O^3P)]$ such as $10^{-4} \sim 10^{-7}$ s^{-1} are similar to that of $k_{loss,O3}$ such as 10^{-6} s^{-1}. Due to the differences in the dust properties, the average values of the coefficients of variation are 14.27% at midnight and 16.26% at noon. The maximum value is 25% at noon time, which occurs in the middle of the dust layer. The changes in the size distribution relative to the reference case (C04→B02) reduce O_3 concentration by a factor of 1.8 relative to the clean marine condition. Whereas changes in alkalinity (Ca0→Ca50) reduce O_3 concentration the most, light absorption (H1→H10) reduces O_3 concentration the least, compared with the O_3 concentration of the reference case. In the same dust loading condition, the ratio of the contribution of photolysis to

heterogeneous loss is 0.04 to 0.27 for the changes in O_3 concentration. The maximum ratio is the case of the dust mixture with a B02 size distribution.

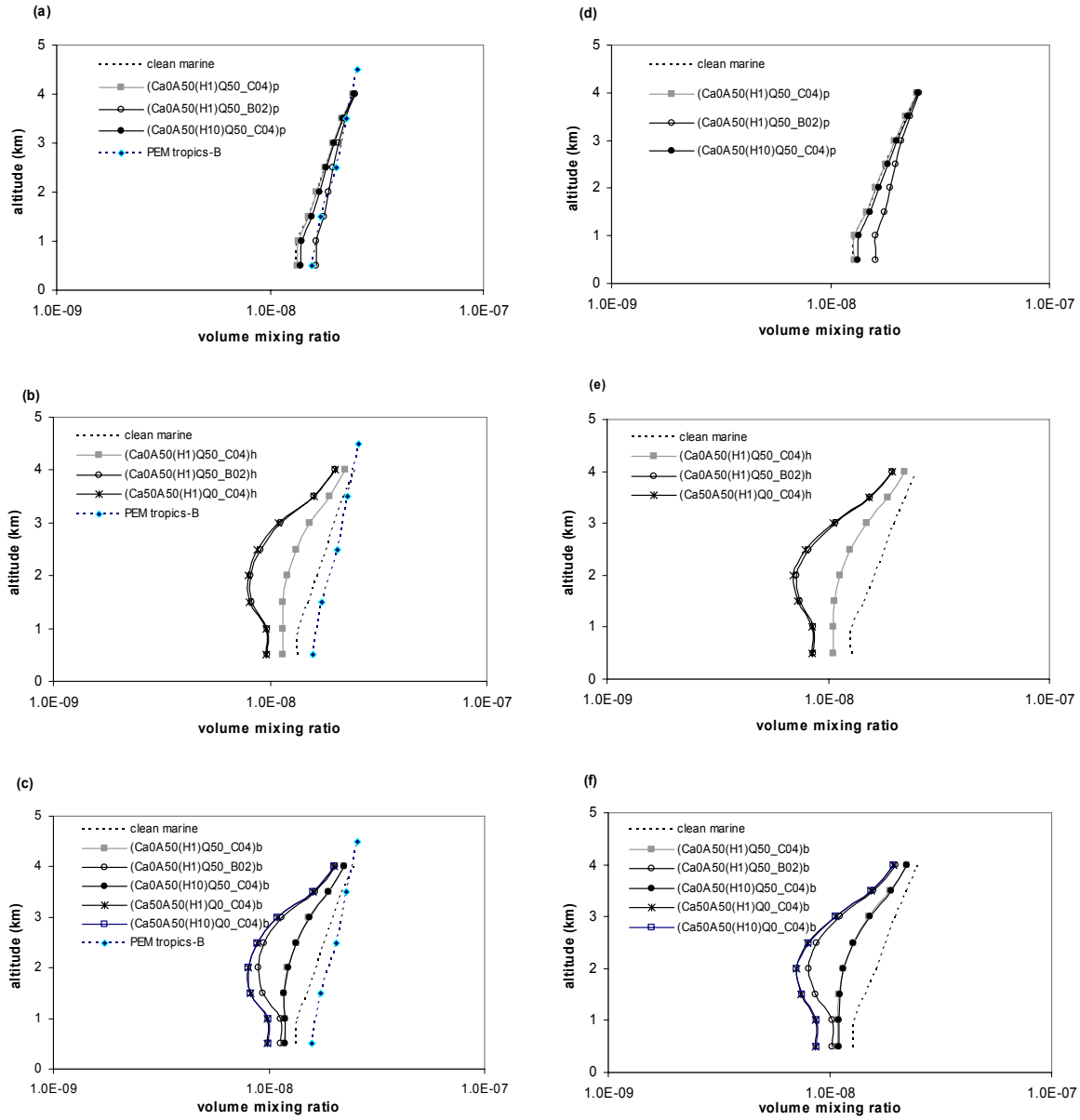

Figure 4.1 The vertical profiles of O_3 at noon (a-c) and at midnight (d-f) averaged over seven days through photolysis (a,d), heterogeneous loss (b,e), and both mechanisms (c,f).

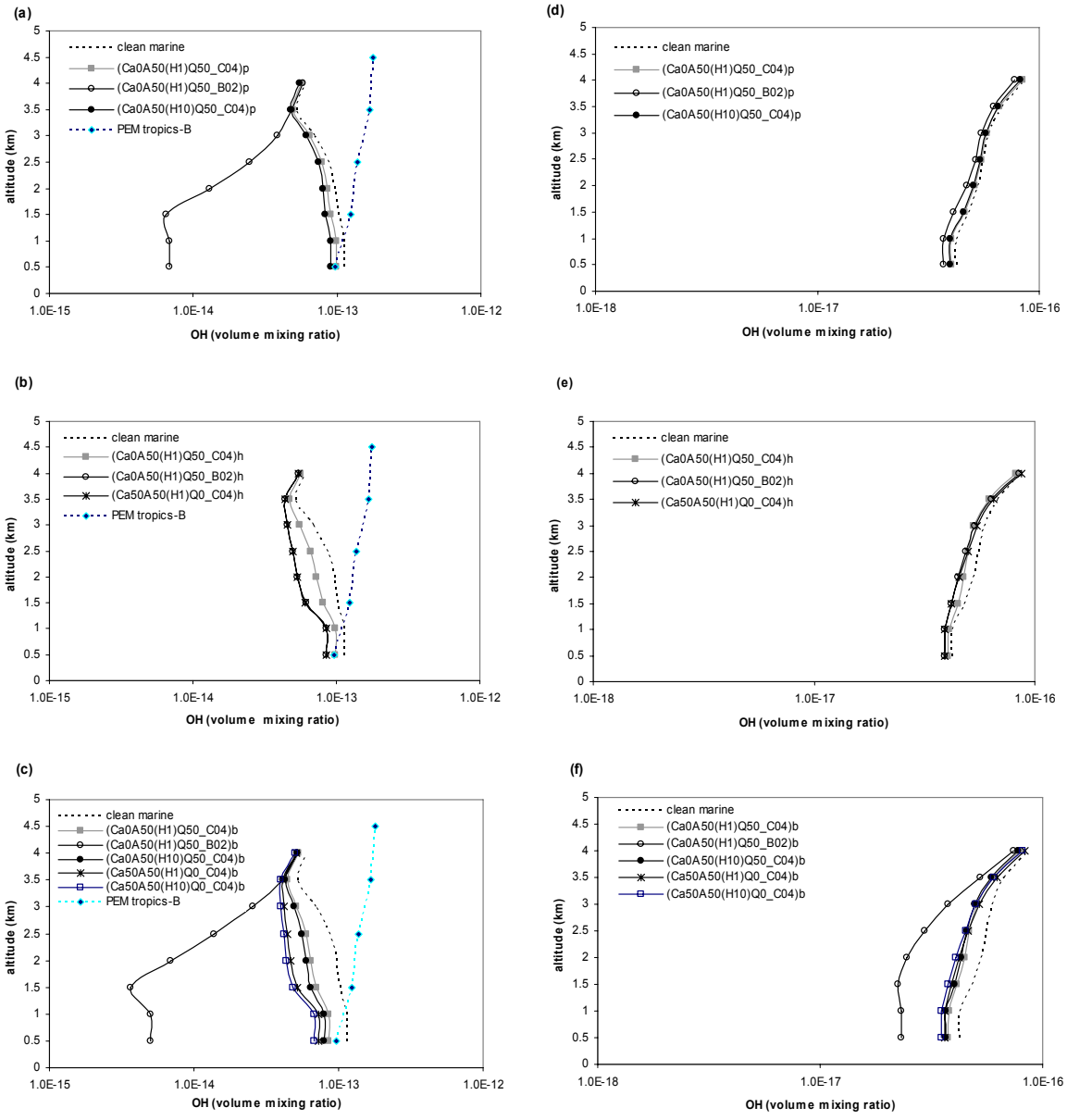

Figure 4.2 The vertical profiles of OH at noon (a-c) and at midnight (d-f) averaged over seven days through photolysis (a,d), heterogeneous loss (b,e), and both mechanisms (c,f).

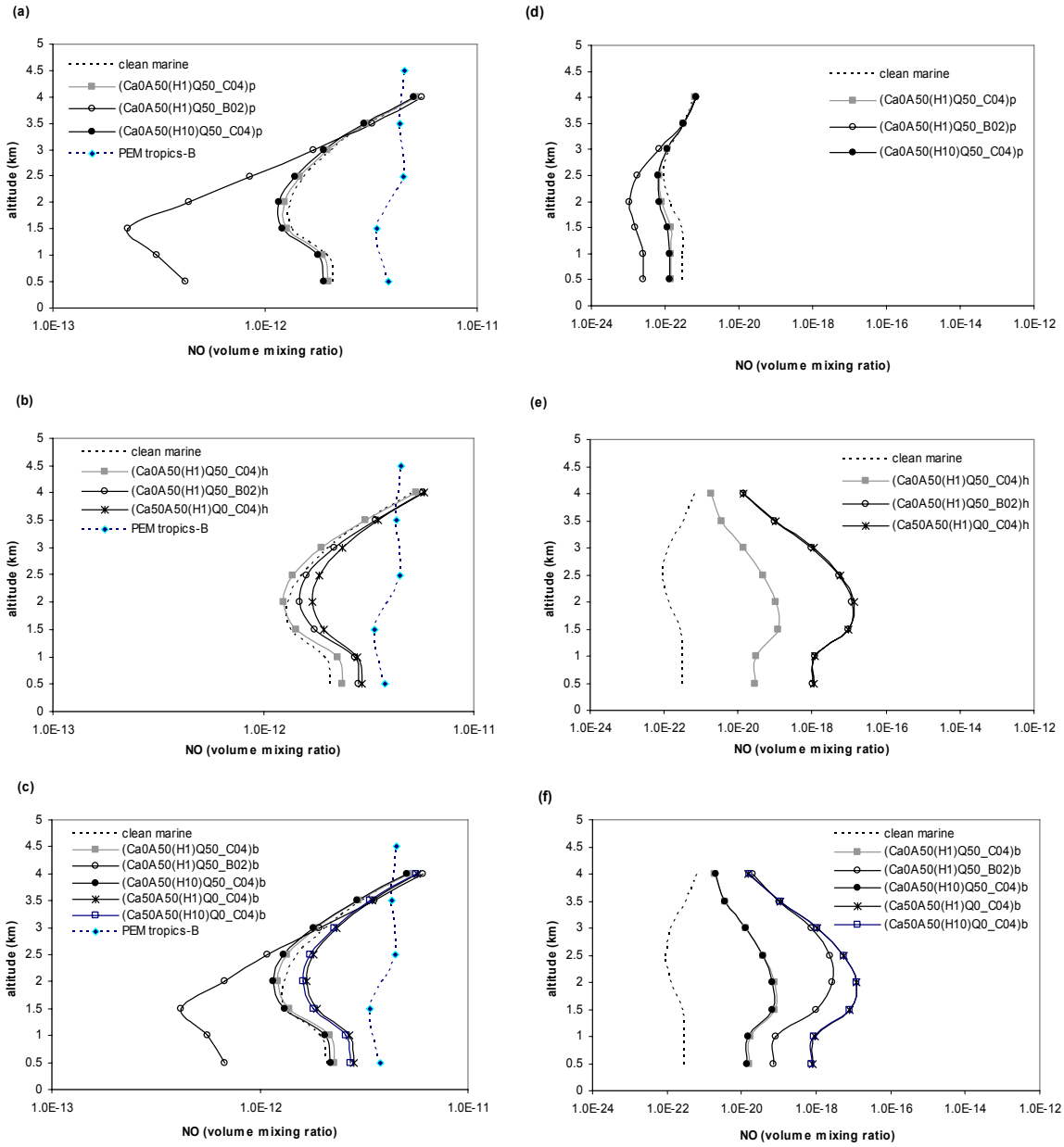

Figure 4.3 The vertical profiles of NO at noon (a-c) and at midnight (d-f) averaged over seven days through photolysis (a,d), heterogeneous loss (b,e), and both mechanisms (c,f).

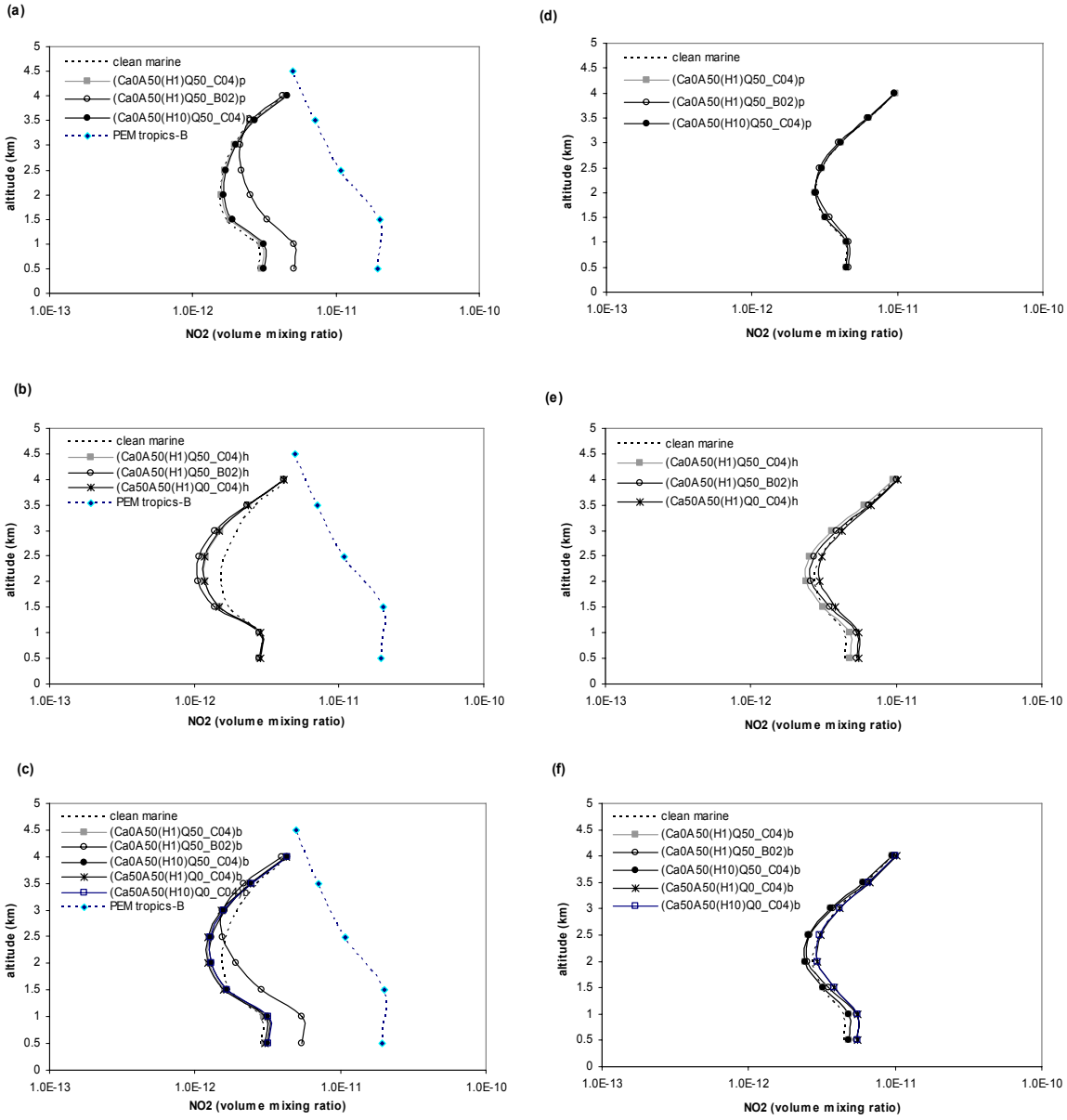

Figure 4.4 The vertical profiles of NO_2 at noon (a-c) and at midnight (d-f) averaged over seven days through photolysis (a,d), heterogeneous loss (b,e), and both mechanisms (c,f).

Figure 4.2 shows that the vertical profiles of OH have a distinct diurnal variation, decreasing with altitude at noon while increasing with altitude at midnight in the clean marine condition. In the presence of the dust layer, OH decreases through both photolysis and heterogeneous loss. The ratio of the contribution of photolysis to heterogeneous loss is 0.7 to 3.8 for the changes in OH concentration. In turn, the B02 size distribution causes drastic changes in the vertical profile of OH. OH concentration decreases in the lower dust layer and below the dust layer by more than one order of magnitude, relative to the clean marine atmosphere. OH concentration changes up to 55% at midday due to differences in the properties of dust mixtures.

The vertical profiles of NO also show a distinct diurnal variation (Figure 4.3). The vertical profile of NO concentration shows the C-shape because of the top flux (4.0×10^7 cm^2/s) and emissions from the surface (8.2×10^7 cm^2/s). NO concentration decreases by a factor of 2 to 5 through photolysis but it increases by a factor of 1 to 1.3 through heterogeneous reactions, relative to the clean marine atmosphere. Light absorption causes few changes in the vertical profiles of NO through photolysis. However, the B02 size distribution drastically decreases the lower dust layer or below the dust layer by a factor of 5 because of a reduction in photolysis rates. Through both mechanisms, the vertical profiles of NO concentration are close to those of heterogeneous loss. The ratio of the contribution of photolysis to heterogeneous loss is 0.7 to 9.8 for the changes in NO concentration.

The vertical profiles of NO_2 also show a distinct diurnal variation (Figure 4.4). The vertical profile of NO_2 exhibits a C-shape similar to that of NO, mainly because of the top flux (4.0×10^7 cm^2/s). The NO_2 concentration at noon is smaller than that at midnight. The dust layer raises the NO_2 concentration relative to the clean marine atmosphere through photolysis while the dust layer reduces the NO_2 concentration through heterogeneous loss like in the case of O_3. However, the magnitude of $J[NO_2]$,

10^{-3} - 10^{-4}, is larger than that of $k_{loss,NO2,}$ 10^{-6} by 2 to 3 orders of magnitude (Chapter 3). Considering both mechanisms, NO_2 concentration increases in the lower dust layer and below the dust layer relative to the clean marine atmosphere through photolysis, and it decreases in the upper dust layer and above the dust layer relative to the clean marine atmosphere through heterogeneous reactions. The ratio of the contribution of photolysis to heterogeneous loss is 0.26 to 2.23 for the changes in NO_2 concentration. In turn, NO_2 increases primarily due to the dust size distribution through photolysis, followed by alkalinity. The effect of light absorption is negligible. The maximum variation of the vertical profiles of NO_2 is 30% and appears in the lower dust layer or below the dust layer at noon time.

Figures 4.5 and 4.6 show the diurnal variations of the vertical profiles of HNO_3 and SO_2, respectively. In the NO_DUST condition, HNO_3 decreases with altitude mainly due to the top flux (4.0×10^7 cm^2/s). HNO_3 concentrations in the clean marine atmosphere are less than those of observations of the PEM tropics by a factor of 2 to 10. The vertical profiles of HNO_3 concentration do not change through photolysis. However, through heterogeneous reaction on the dust mixtures, HNO_3 concentration decreases at noon by four orders of magnitude relative to the clean marine atmosphere. Such a high reduction in HNO_3 concentration is due to both high heterogeneous loss rates and high photolysis rates in the clean marine condition. Thus, at midnight, a reduction in HNO_3 in the dust layer weakens. The ratio of the contribution of photolysis to heterogeneous loss is 0.001 to 0.004 for the changes in HNO_3 concentration. In turn, the heterogeneous loss of HNO_3 occurs according to the amounts of both calcium carbonate and clay aggregates. The dust mixtures used in the test of heterogeneous mechanisms such as (Ca0A50(H1)Q50)_C04 and (Ca50A50(H1)Q0)_C04 are composed of mineralogical species such as calcite and clay aggregate with uptake coefficients as high as 10^{-1}. Considering both mechanisms, HNO_3 decreases mainly due to the change in the dust size distribution (Ca0A50(H1)Q50_B02) through heterogeneous reaction and secondly due to the change

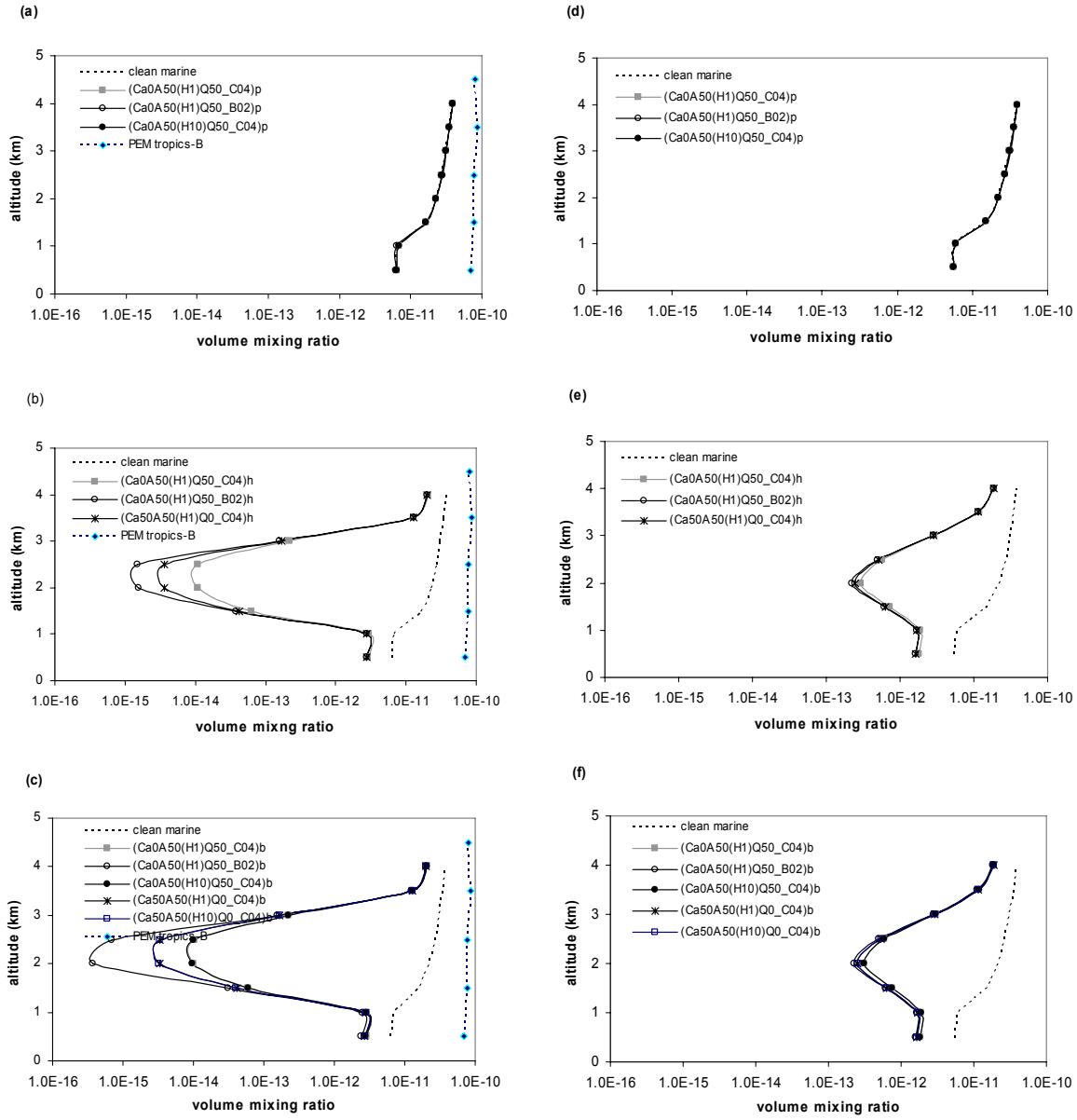

Figure 4.5 The vertical profiles of HNO_3 at noon (a-c) and at midnight (d-f) averaged over seven days through photolysis (a,d), heterogeneous loss (b,e), and both mechanisms (c,f).

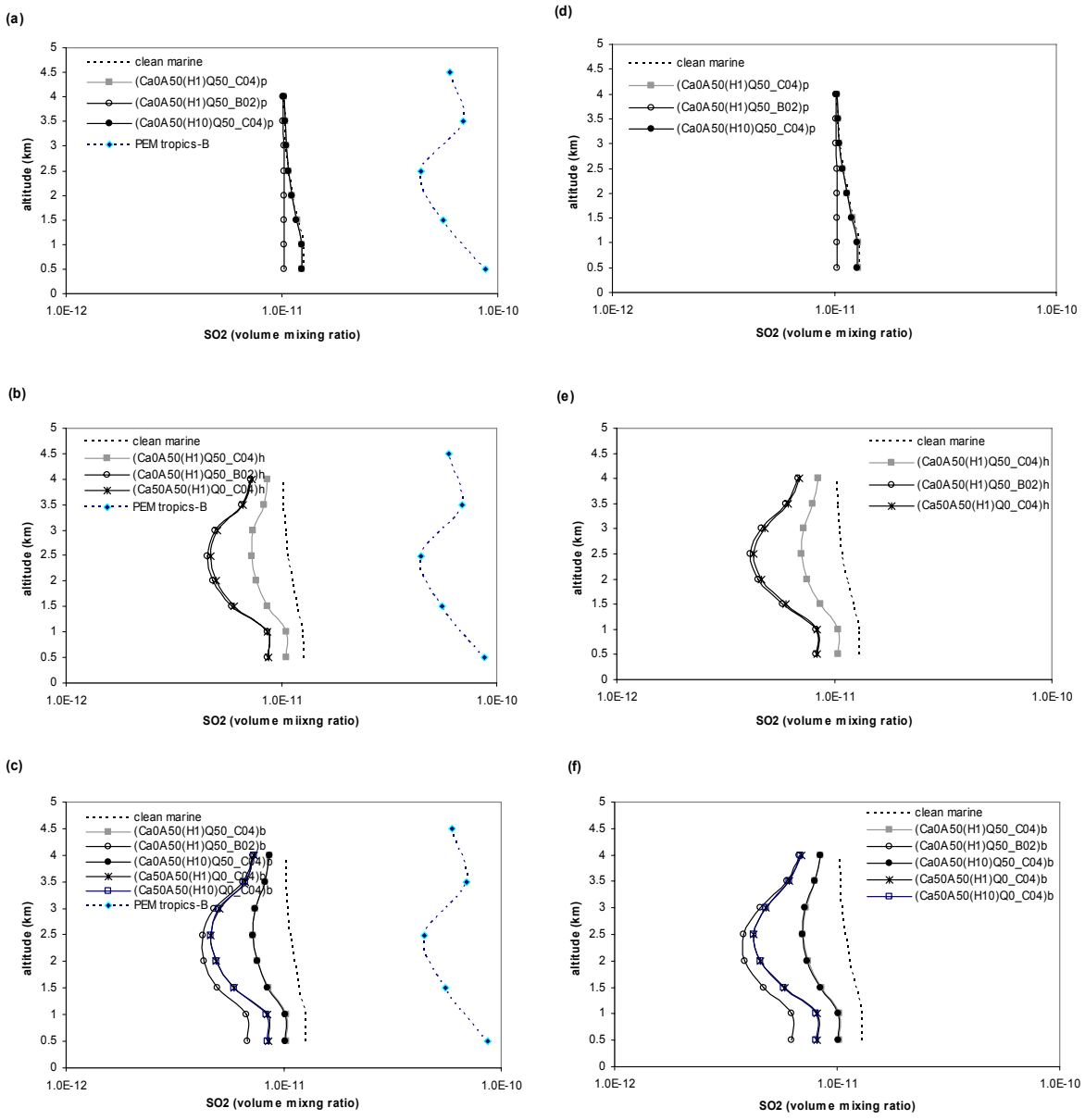

Figure 4.6 The vertical profiles of SO_2 at noon (a-c) and at midnight (d-f) averaged over seven days through photolysis (a,d), heterogeneous loss (b,e), and both mechanisms (c,f).

in alkalinity (Ca50A50(H1)Q50_C04) through a heterogeneous reaction. The effect of light absorption is negligible. The maximum variation of HNO_3 concentration due to the properties of dust is 80% in the middle of the dust layer.

Figure 4.6 shows the vertical profiles of SO_2. SO_2 concentration in the lower atmosphere is higher than that in the upper atmosphere mainly because of the fluxes of SO_2 and H_2S from the sea. The ratio of the contribution of photolysis to heterogeneous loss is 0.02 to 0.2 for the changes in SO_2 concentration relative to the clean marine condition. In the presence of dust, changes in both the size distribution and alkalinity are important to SO_2 concentration through heterogeneous loss. SO_2 concentration decreases due to changes in the dust size distribution (C04→B02) through photolysis, most likely due to the large reduction in the OH radical in the lower atmosphere when dust mixtures have the B02 size distribution. Considering both mechanisms, SO_2 decreases primarily due to differences in the size distribution (C04→B02) followed by differences in alkalinity (Ca0→Ca50). The effect of light absorption on changes in SO_2 concentration is negligible. The maximum variation of SO_2 concentration due to the properties of dust is 27% at noontime and 31% at midnight in the middle of the dust layer.

In short, HNO_3 and SO_2 decrease through photolysis and heterogeneous loss, with heterogeneous loss dominating photolysis. HNO_3 concentration is less than it is in the clean marine condition through both mechanisms by 3 to 4.5 orders of magnitude at noon and by 2 orders of magnitude at midnight. SO_2 concentration decreases relative to the clean marine condition through both mechanisms by a factor of 2 to 2.5 at noon and by a factor of 2 to 3 at midnight. Therefore, the reduction in the concentration of HNO_3 and SO_2 can be considered good indicators of the location of the dust layer. The reduction in the concentration of HNO_3 causes a decrease in the photolysis of HNO_3 which leads to decreases in OH and NO_2, which results in the reduction of O_3.

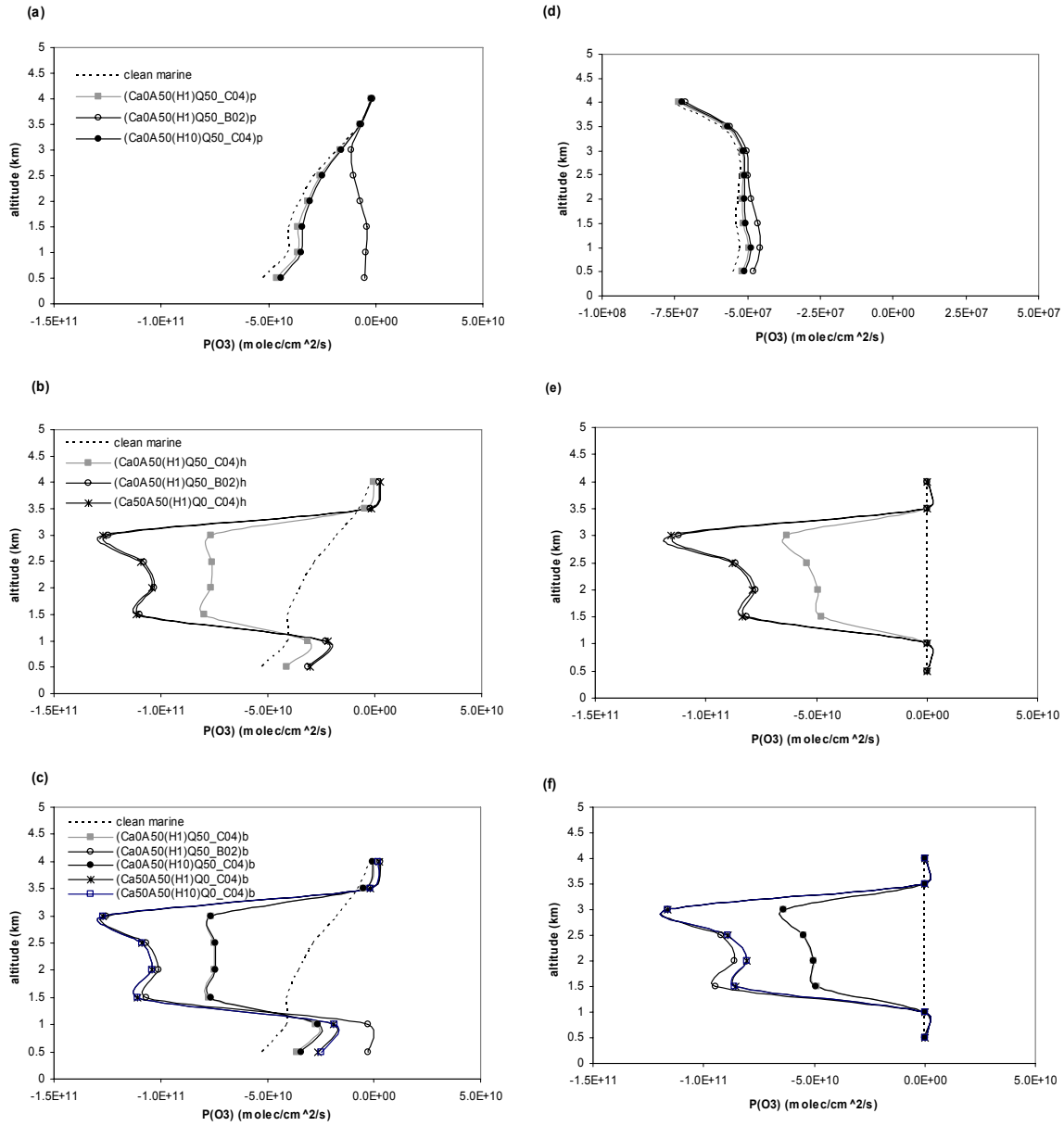

Figure 4.7 The vertical profiles of $P(O_3)$ at noon (a-c) and at midnight (d-f) averaged over seven days through photolysis (a,d), heterogeneous loss (b,e), and both mechanisms (c,f).

In DUST-ONLY cases, ozone production rates were calculated by using the chemical reactions R5, R14, R23, R36, and R63.

$HO_2 + NO \rightarrow OH + NO_2$ (R36)

$CH_3O_2 + NO \rightarrow CH_3O + NO_2$ (R63)

$O(^1D) + H_2O \rightarrow 2OH$ (R5)

$HO_2 + O_3 \rightarrow OH + 2O_2$ (R23)

$OH + O_3 \rightarrow HO_2 + O_2$ (R14)

$$P(O_3) = F(O_3) - D(O_3)$$

$$= k_{R36}[HO_2][NO] + k_{R63}[CH_3O_2][NO] - k_{R5}[O(^1D)][H_2O] - k_{R23}[HO_2][O_3] - k_{R14}[OH][O_3]$$

In the clean marine atmosphere (NO_DUST), the destruction of ozone is greater than the formation of ozone. Figure 4.7 shows that the presence of a dust layer (DUST_ONLY) increases the ozone production rate $P(O_3)$ through photolysis. Even though the reduction of photolysis rates reduces both the formation rates and the destruction rates of ozone, it reduces the latter to a greater extent than it does the former. The $P(O_3)$ in the dust layer embedded with the B02 size distribution is larger than that in the clean marine environment by one order of magnitude. Through heterogeneous reaction, $P(O_3)$ at noon is less than $P(O_3)$ at midnight by a factor of 1.5 because photolysis in the clean maritime condition is added to ozone destruction. However, above and below the dust layer, ozone destruction is still less than one in the clean-marine condition because of other photochemical species, such as NO, perturbed by heterogeneous reactions on dust particles and photolysis in the clean marine environment.

Ozone destruction is much less for (Ca0A50(H1)Q50_B02) than for any other dust mixture through photolysis. Through heterogeneous reaction, $P(O_3)$ is affected by the fine mode dominant dust mixture of (Ca0A50(H1)Q50_B02) as much as it is by the

high alkalinity dust mixture of (Ca50A50(H1)Q0_C04). Considering both mechanisms, $P(O_3)$ in the dust layer decreases primarily in the fine mode dominant dust mixture of (Ca0A50(H1)Q50_B02), followed by the high alkalinity dust mixture of (Ca50A50(H1)Q0_C04).

To summarize, Figure 4.8 shows the fractional changes in the column concentration of species relative to the clean marine atmosphere through a single mechanism: (a) photolysis, (b) heterogeneous reaction, and (c) both mechanisms. The concentrations of O_3 and NO_2 increase while those of OH, NO, HNO_3, and SO_2 decrease through photolysis. In particular, changes in OH through photolysis are from -13.4% to -73.7% due to the difference in the dust size distribution and from -13.4% to -19.3% due to variations in light absorption. Changes in the concentrations of HNO_3 and SO_2 are negligible. Through heterogeneous loss, the concentrations of NO increase in the dust mixture with high alkalinity while those of NO_2, OH, O_3, HNO_3, and SO_2 decrease. In particular, changes in HNO_3 of about -62.8% to -63.2% are due to differences in the size distribution and alkalinity.

Through both photolysis and heterogeneous loss mechanisms, the concentrations of O_3, OH, NO, HNO_3, and SO_2 decrease through photolysis while the concentrations of NO_2 increase or decrease depending on the type of mixture. O_3 concentration is affected primarily by the dust mixture of Ca50A50(H1)Q0_C04, mainly because of alkalinity through heterogeneous loss (-9.9% to -21.8%). The OH concentration is affected primarily by the dust mixture of Ca0A50(H1)Q50_B02, mainly due to the size distribution through photolysis (-22.2% to -77.5%). The concentrations of NO and NO_2 are affected primarily by the dust mixture of Ca0A50(H1)Q50_B02, mainly because of the size distribution through photolysis. Changes in NO and NO_2 concentrations are from -35.1% to 3.4% and from -4.1% to 7.8%, respectively.

On the other hand, the concentrations of HNO_3 and SO_2 are controlled mainly by heterogeneous reaction rather than photolysis. HNO_3 decreases more than 63.8% through

the high uptake coefficients of mineral species. However, the difference in the uptake coefficients between the individual mineral species is not likely to affect the heterogeneous loss rates of HNO_3. SO_2 concentration, which changes from -29.0% to -13.5% relative to the clean marine atmosphere, is affected primarily by the dust mixture of Ca0A50(H1)Q50_B02, which has a fine mode-dominant size distribution through heterogeneous loss.

Our results demonstrate that the size distribution and the composition of dust particles affect the concentration of photochemical species through photolysis or through heterogeneous reactions in the same or opposite directions. Through photolysis-only, O_3 and NO_2 concentrations increase when the size distribution of the dust mixture is dominant in the fine mode (Ca0A50(H1)Q50_B02). However, through heterogeneous loss-only, NO increases in the dust mixture of Ca0A50(H1)Q50_B02 and Ca50A50(H1)Q0_C04. The OH concentration is most effectively reduced by photolysis and O_3, SO_2, and HNO_3 by heterogeneous reactions. As a whole, a dust mixture of the fine mode-dominant dust size distribution (Ca0A50(H1)Q50_B02) is the most effective at controlling the oxidant field through photolysis and heterogeneous loss. The next most effective is alkalinity by the amount of carbonaceous compounds, and the least effective is light absorption.

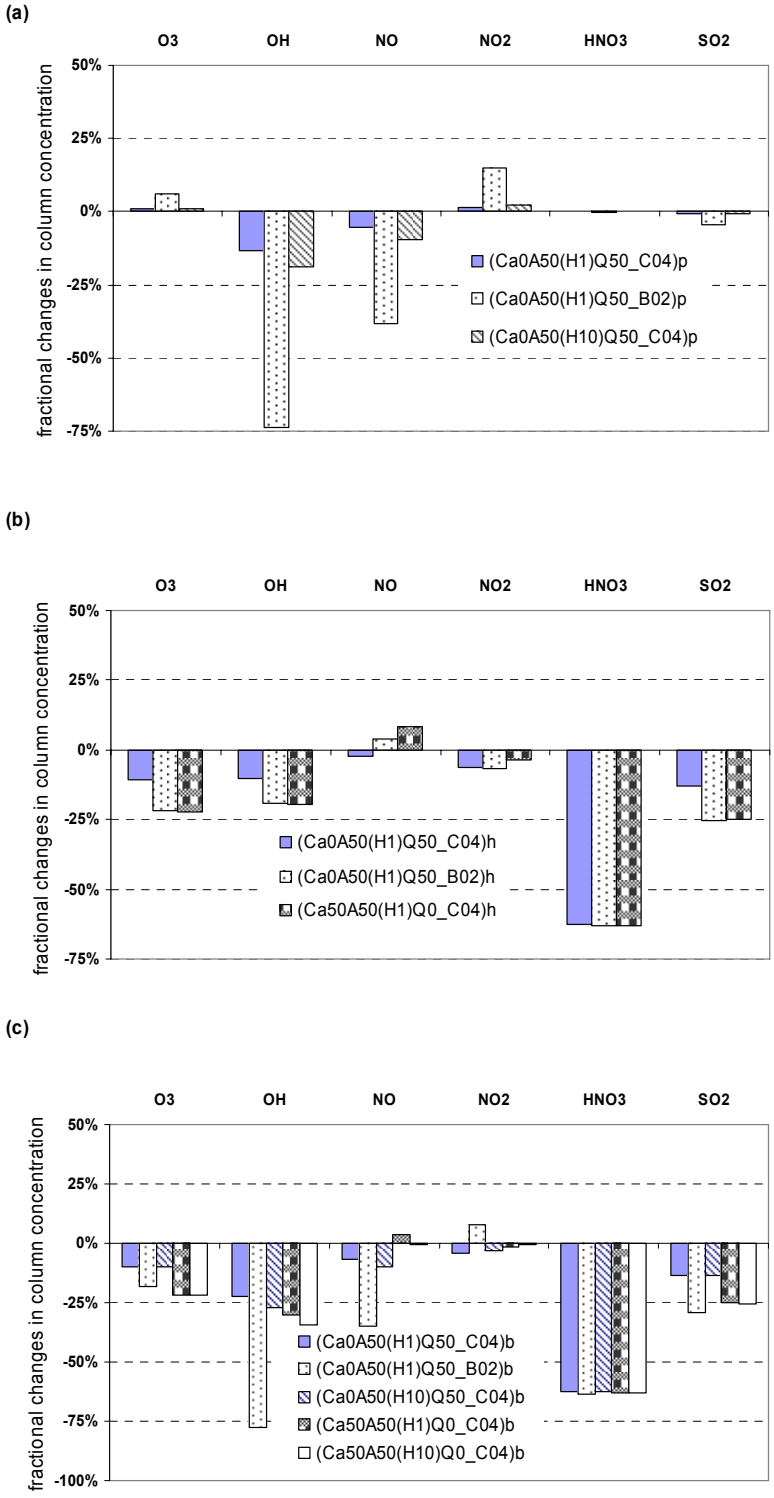

Figure 4.8 Fractional changes in column concentration relative to the marine atmosphere through (a) photolysis, (b) heterogeneous loss, and (c) both mechanisms.

To elucidate the effects of mixing states on photochemical fields, Figures 4.9 through 4.14 (a) at noon and (b) at midnight show differences between the concentration of photochemical species of internal mixing and that of external mixing. The solid line indicates the H10 dust-BC mixture, and the dotted line indicates the H1 dust-BC mixture. Since dust mixtures with different light absorption were used, the photolysis-only mechanism (the open circle) and both mechanisms (the filled circle) were considered. Positive values indicate that the gaseous concentration due to internal mixing is larger than that due to external mixing. The concentrations of O_3 , HNO_3, and SO_2 in internal mixing differ from those in external mixing by less than 10%, shown in Figures 4.9, 4.13, and 4.14, respectively. By contrast, the concentrations of OH, NO, and NO_2 differ by more than 10%.

Figure 4.10 shows how the concentration of OH in internal mixing differs from that in external mixing. The differences are the largest in the lower layer, approximately 20% to 25% at noon, and in the middle dust layer, approximately 20% to 30% at midnight. The OH concentration is larger in internal mixing than in external mixing because the photolysis rates of groups I and II decrease more in external mixing than in internal mixing (Chapter 2). The difference due to the mixing state is larger in the H1 dust-BC mixture than it is in the H10 dust-BC mixture.

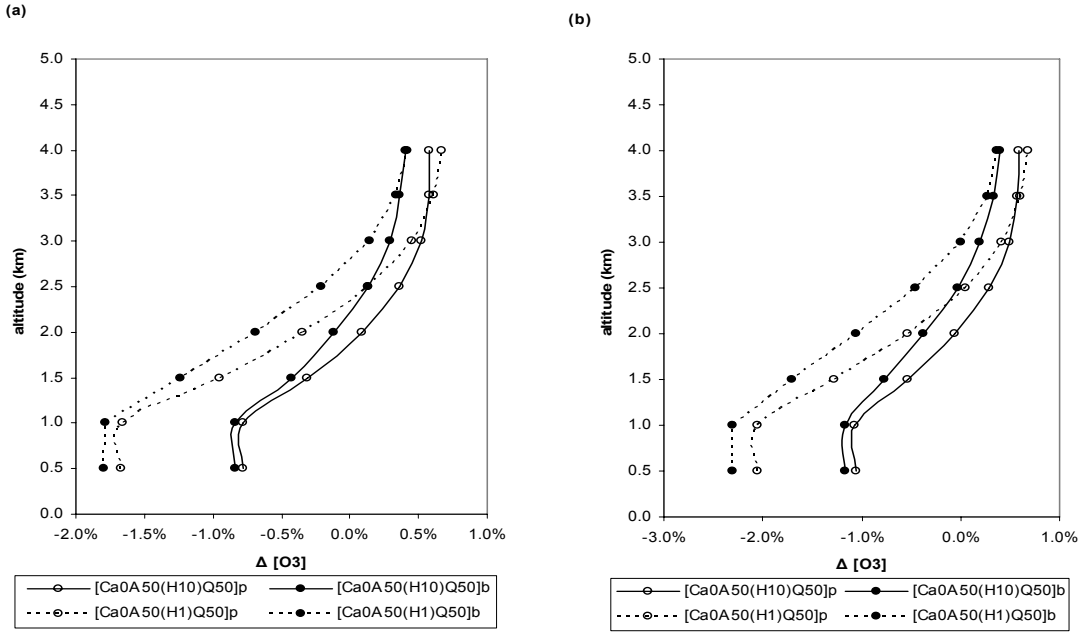

Figure 4.9 The differences between the O_3 concentration in internal mixing and that in external mixing through photolysis and through both mechanisms for the H1 dust-BC mixture and the H10 dust-BC mixture (a) at noon and (b) at midnight.

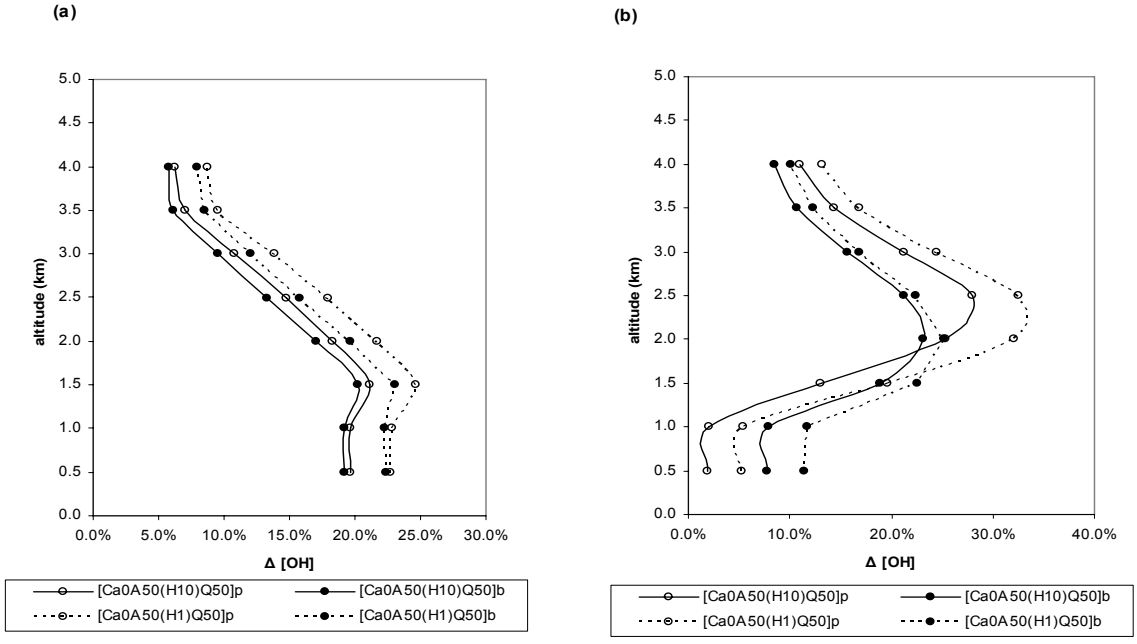

Figure 4.10 The differences between OH concentration in internal mixing and that in external mixing through photolysis and through both photolysis and heterogeneous reaction for the H1 dust-BC mixture and the H10 dust-BC mixture (a) at noon and (b) at midnight.

Figure 4.11 shows the differences between the NO concentrations of the two mixing states, which decrease with height. NO is also greater in internal mixing than it is in external mixing. The difference is larger at midnight than at noon. The difference due to the mixing state is larger in the dust layer and larger in the H10 dust-BC mixture than in the H1 dust-BC mixture. The mixing effect on NO is larger through photolysis rather than through both mechanisms. In turn, NO_2 concentration is larger in external mixing than in internal mixing (see Figure 4.12). The difference between NO_2 concentrations in the lower dust layer is larger than in the upper dust layer. Differences due to the mixing state are larger in the H1 dust-BC mixture than in the H10 dust-BC mixture.

Such differences in photochemical species due to mixing states result in peculiar vertical profiles of the differences in the ozone production rates $P(O_3)$. Figures 4.15 (a) and (b) show the fractional differences in $P(O_3)$ between internal and external mixing against the $P(O_3)$ in external mixing (a) at noon and (b) at midnight. Since $P(O_3)$ is negative in both internal and external mixing, the absolute values of $P(O_3)$ were used for plotting Figure 4.15. Open circles indicate only through photolysis, and filled circles indicate through both photolysis and heterogeneous loss. The amount of iron oxide in the clay aggregates is distinguished using line types: a solid line indicates H10 dust and a dotted line indicates H1 dust.

As shown in Figure 4.15, through photolysis only, the difference shows a maximum amount below the dust layer at noon and maximum amount in the middle of the dust layer at midnight, indicating that the values of $P(O_3)$ are larger in internal mixing than in external mixing. Through both mechanisms, $P(O_3)$ is also larger in internal mixing than in external mixing below the dust layer. In the dust layer, $P(O_3)$ due to the mixing state does not differ. In turn, the light absorption property of dust mixtures is insignificant in $P(O_3)$, as the H1 dust-BC mixtures differ only slightly from the H10 dust-BC mixtures.

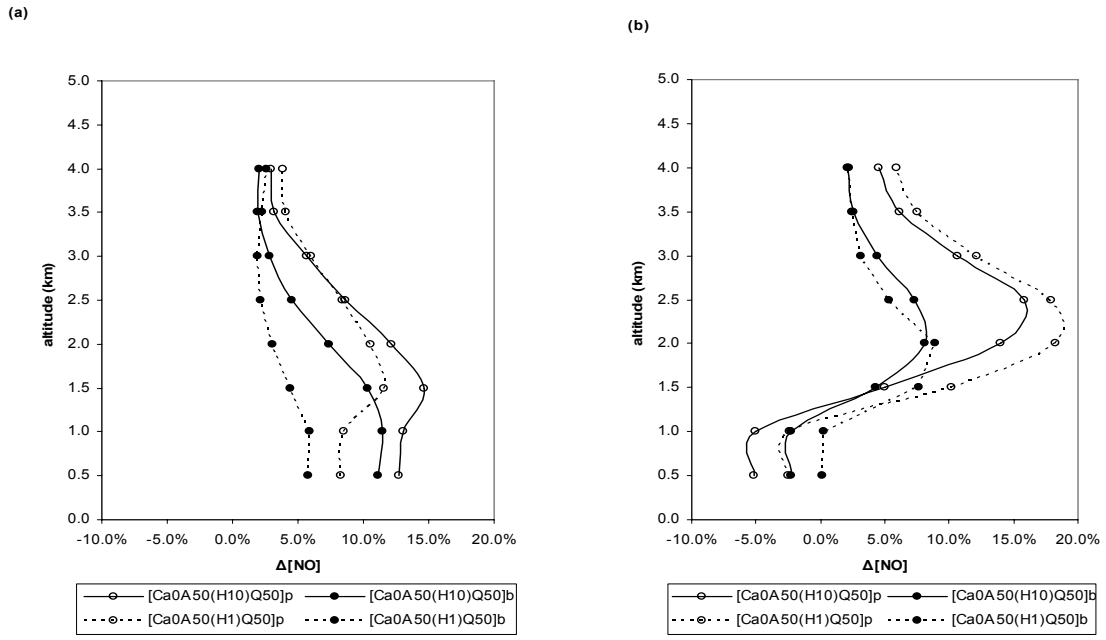

Figure 4.11 The differences between NO concentration in internal mixing and that in external mixing through photolysis and through both photolysis and heterogeneous reaction for the H1 dust-BC mixture and the H10 dust-BC mixture (a) at noon and (b) at midnight.

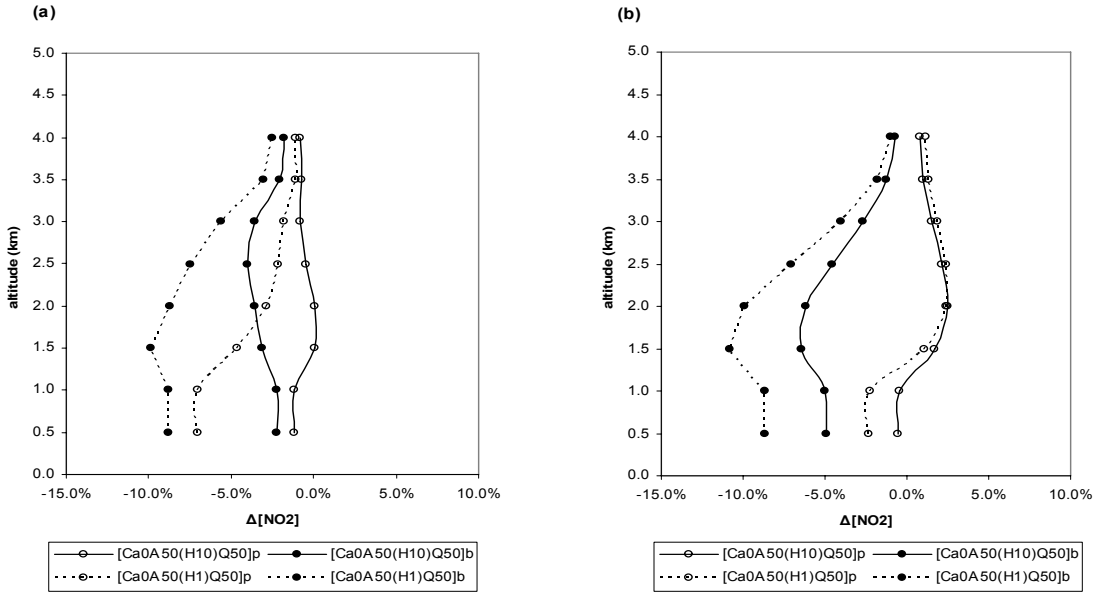

Figure 4.12 The differences between NO_2 concentration in internal mixing and that in external mixing through photolysis and through both photolysis and heterogeneous reaction for the H1 dust-BC mixture and the H10 dust-BC mixture (a) at noon and (b) at midnight.

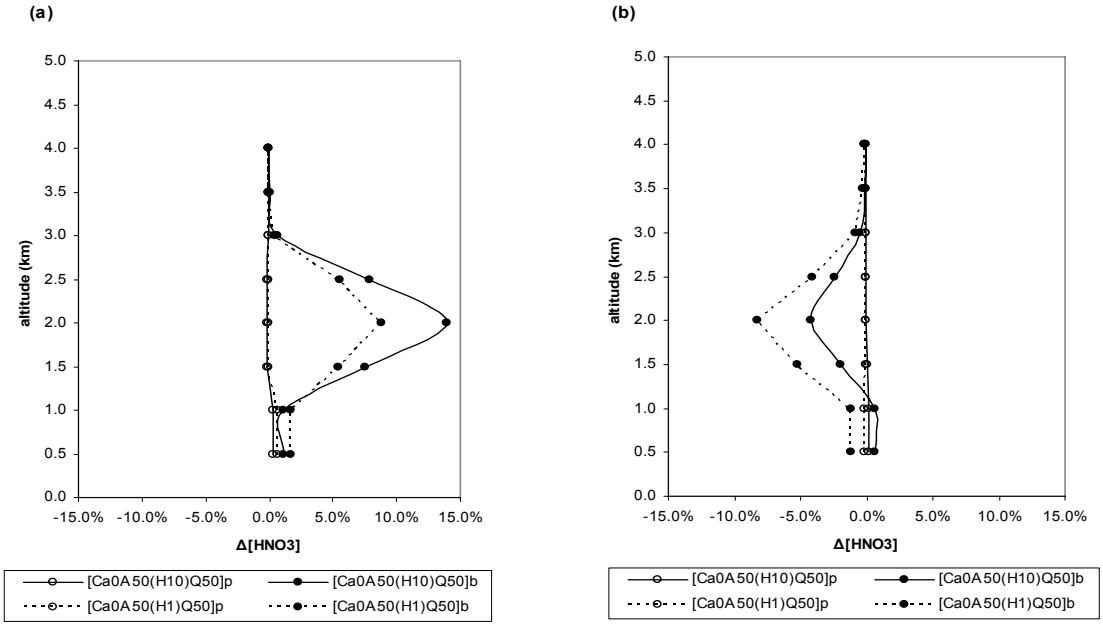

Figure 4.13 The differences between HNO_3 concentration in internal mixing and that in external mixing through photolysis and through both photolysis and heterogeneous reaction for the H1 dust-BC mixture and the H10 dust-BC mixture (a) at noon and (b) at midnight.

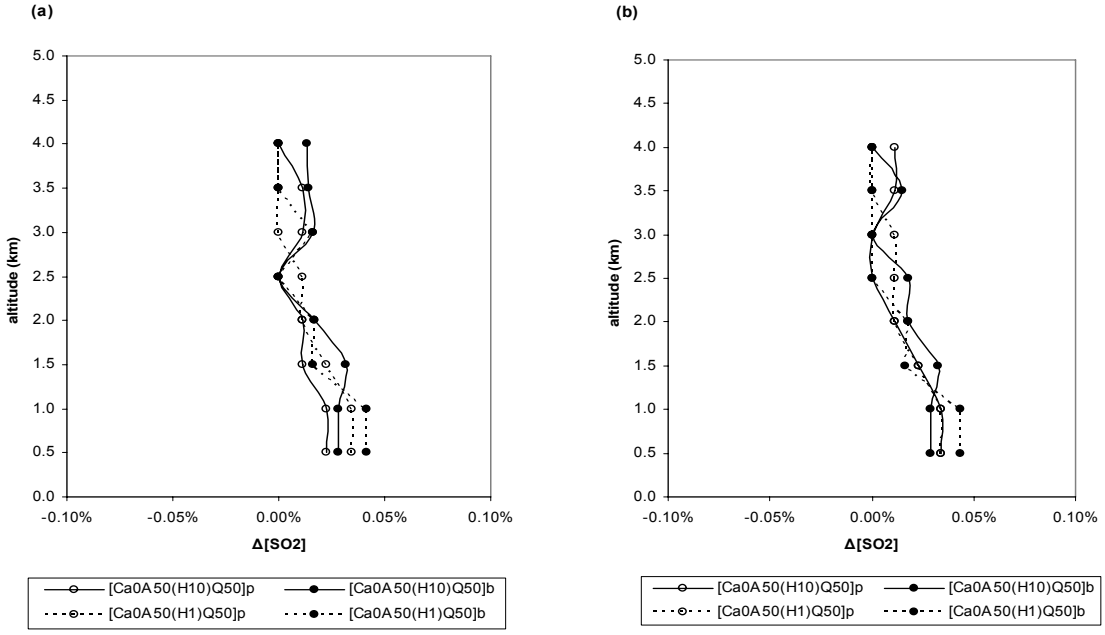

Figure 4.14 The differences between SO_2 concentration in internal mixing and that in external mixing through photolysis and through both photolysis and heterogeneous reaction for the H1 dust-BC mixture and the H10 dust-BC mixture (a) at noon and (b) at midnight.

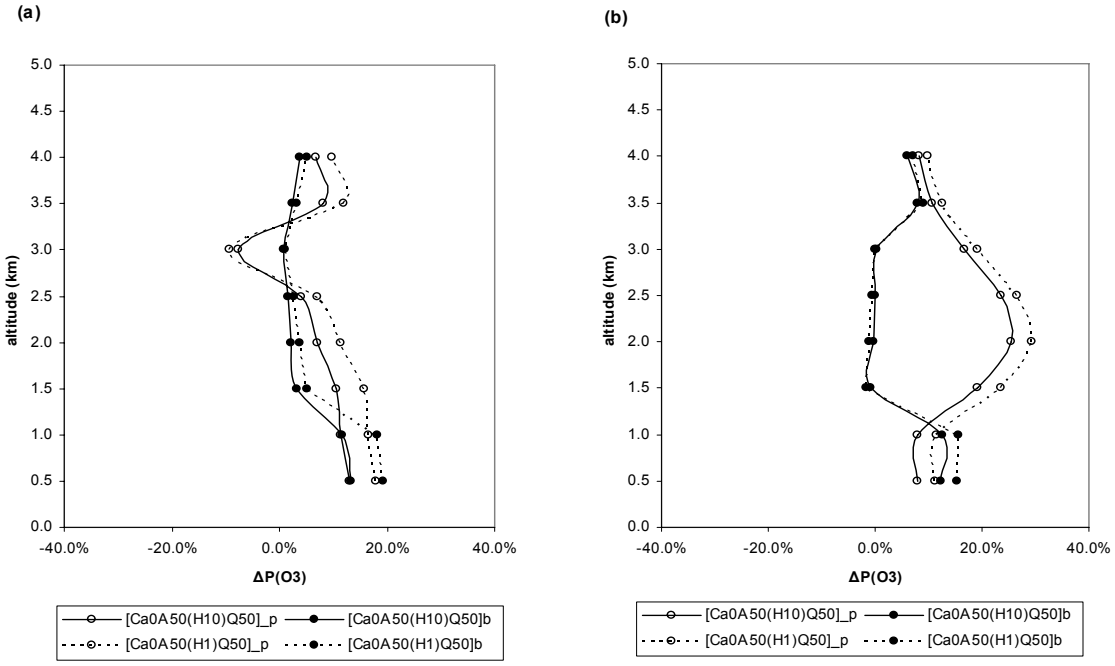

Figure 4.15 The differences between $P(O_3)$ in internal mixing and that in external mixing through photolysis and through both photolysis and heterogeneous reaction for the H1 dust-BC mixture and the H10 dust-BC mixture (a) at noon and (b) at midnight.

Figure 4.16 (a) and (b) show fractional changes in the column concentrations of O_3, OH, NO, NO_2, SO_2, and HNO_3 relative to the polluted marine atmosphere through photolysis only and both mechanisms, respectively. Dust-BC-pollutant mixing decreases the concentration of OH and NO while it increases the concentrations of O_3 and NO_2. Because a flipping point of the H1 dust-BC mixture is closer to a shorter wavelength than that of the H10 dust-BC mixture, the external mixture absorbs more light than the internal mixture. Thus, photolysis in the external mixture is lower than that in the internal mixture, as shown in Chapter 2. The difference in the fractional changes in the column concentration of gaseous species due to the mixing state is the largest in the case of OH: between 1.3% and -15.1% for the H1 dust-BC mixture and between -8.7% and -22% for the H10 dust-BC mixture. NO is the second largest: between -0.2% and -7.5% for the H1 dust-BC mixture and between -5.3% and -12.8% for the H10 dust-BC mixture. The third

is NO_2: between -2.0% and 0.8% for the H1 dust-BC mixture and between 0.4% for the H10 dust-BC mixture. However, the mixing state has a slight effect on O_3, HNO_3, and SO_2.

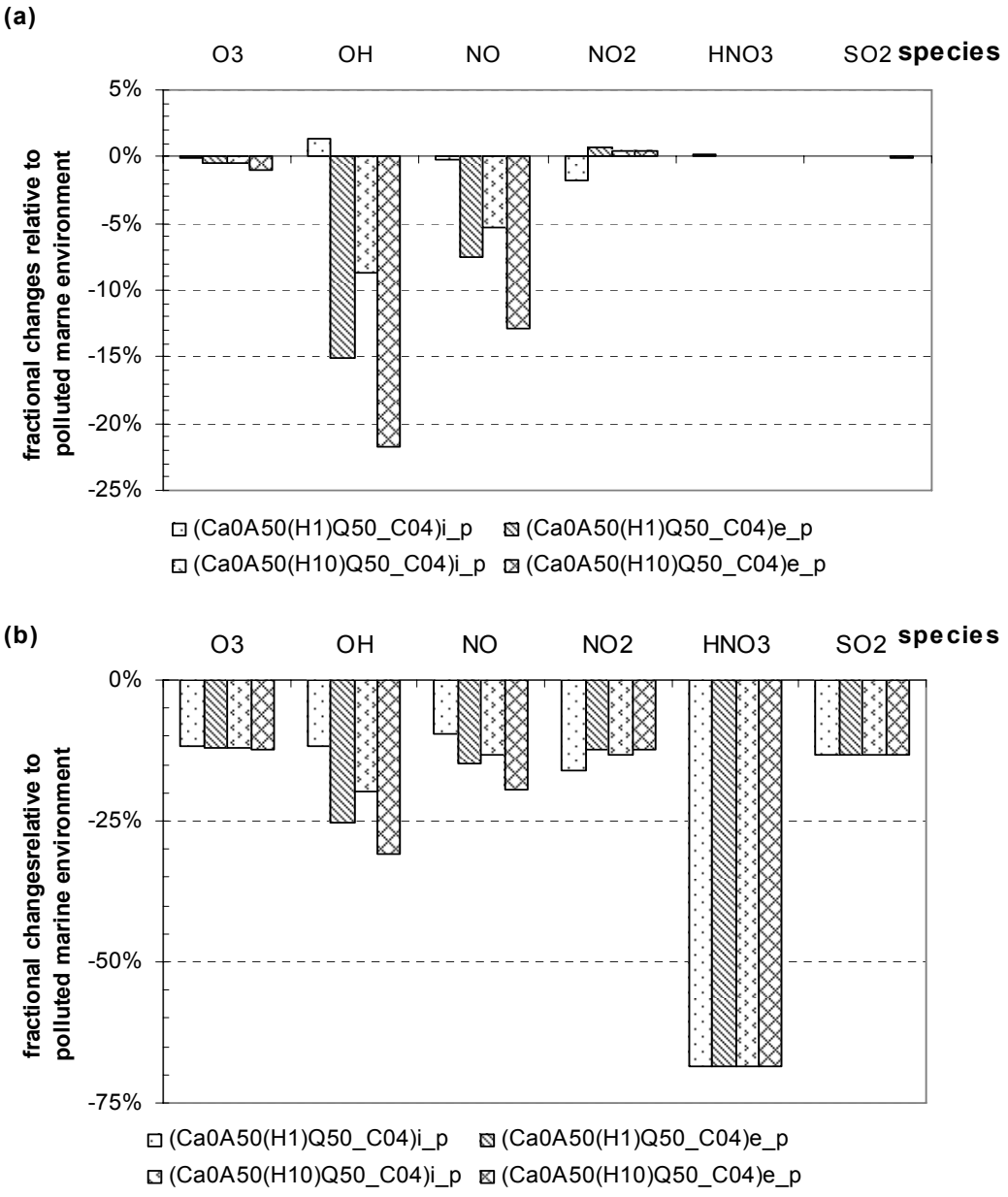

Figure 4.16 The fractional changes in column concentration relative to the polluted marine atmosphere (a) through photolysis and (b) through both mechanisms.

Figure 4.17 shows how the mixing state of a dust-BC mixture affects fractional changes in the column concentration of photochemical species relative to the dust-free polluted atmosphere. The concentrations of OH and NO decrease more in external mixing than they do in internal mixing of dust-BC mixtures. The concentrations of NO_2 decrease more in internal mixing than in external mixing of the dust-BC mixtures. In turn, the difference is larger in the H1 dust-BC mixture than in the H10 dust–BC mixture for OH and NO_2 but it is smaller in the H1 dust-BC mixture than in the H10 dust-BC mixture for NO. Overall, OH is the most sensitive to the mixing state of dust-BC mixtures.

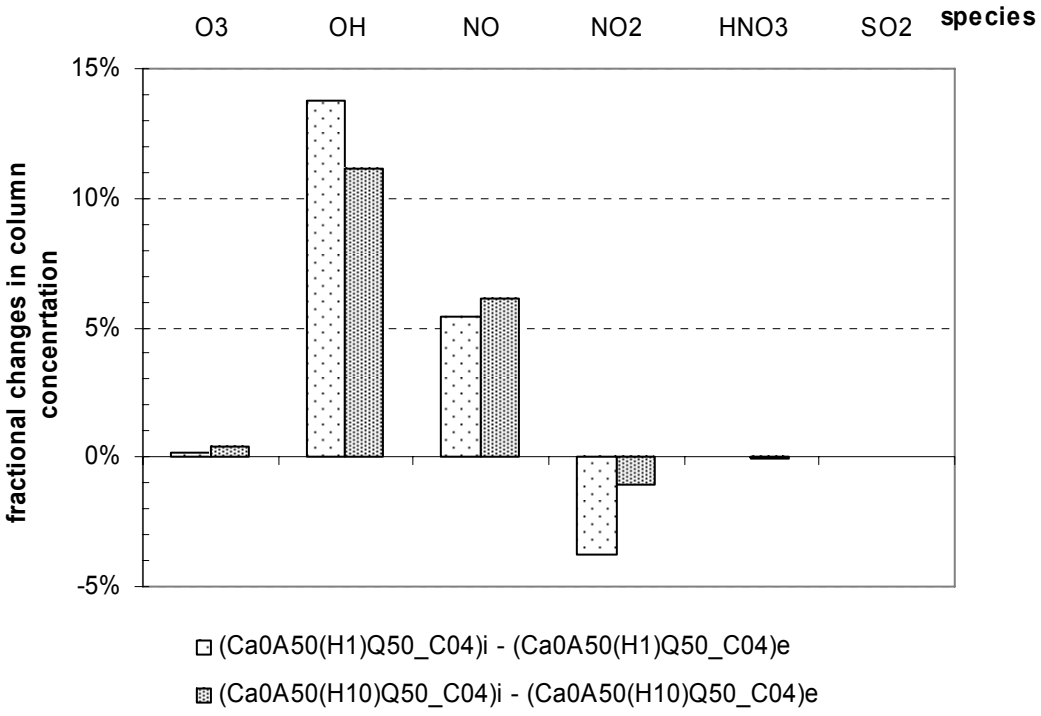

Figure 4.17 The difference between fractional changes in column concentration relative to the polluted marine atmosphere in internal mixing and those in and external mixing.

4.5 Conclusions and Discussion

This chapter described the newly-developed DUST-CHEM model and presented the results of an in-depth investigation of the impact of dust on important photochemical species via photolysis and heterogeneous reactions. The dust-induced changes in the vertical profiles and diurnal variations of O_3, OH, NO, NO_2, HNO_3, and SO_2, as well as ozone production rates $P(O_3)$ through photolysis, heterogeneous loss, and both mechanisms were analyzed. The main findings are as follows:

1. The relative roles of photolysis and heterogeneous loss differ among the photochemical species. For OH, HNO_3, and SO_2, both photolysis and heterogeneous loss enhance the reduction of the concentrations. For O_3, NO_2, and NO, the two mechanisms act in the opposite direction. The ratio of the contribution of photolysis to heterogeneous loss for changes in the concentrations is 0.04 to 0.27 for O_3, 0.001 to 0.004 for HNO_3, 0.02 to 0.2 for SO_2, which are heterogeneous process dominant by one to three orders of magnitude. The ratio of the contribution of photolysis to heterogeneous loss is also 0.7 to 3.8 for OH, 0.7 to 9.8 for NO, and 0.26 to 2.23 for NO_2. The upper bound of the ratio indicates that the B02 size distribution enhances the role of photolysis in atmospheric photochemistry.
2. The vertical profiles of individual species vary with the properties of dust aerosols such as light absorption, alkalinity, and size distribution. The concentration of HNO_3 is the most sensitive to the properties of dust aerosols with a coefficient of variation of 80% in the middle of the dust layer at midday. The coefficients of variation in the vertical profiles of photochemical species are 28% for HNO_3, 19% for SO_2, 36% for OH, 26% for NO, 16% for NO_2, and 14% for O_3 at midday. Through photolysis, the B02 size distribution results in peculiar vertical distributions of species, but light absorption only slightly affects the vertical profiles of the species. Through heterogeneous loss, alkalinity is as important as the dust size distribution.

3. In the presence of dust, the vertical profiles of the ozone production rate, $P(O_3)$, is mainly determined by heterogeneous loss. $P(O_3)$ through photolysis is larger than $P(O_3)$ in the clean marine atmosphere (-7.30×10^{10} molecules /cm^2). Through the heterogeneous reaction, however, the former is smaller than the latter. Through photolysis, $P(O_3)$ varies by a factor of 4 due to the various properties of dust aerosols, mainly because the size distribution shifts to a fine mode. Through heterogeneous loss, $P(O_3)$ varies by a factor of 1.6. Among the five types of dust mixtures considered, the $P(O_3)$ of low (no) alkalinity and the coarse mode-dominant dust mixture $(Ca0A50(H10)Q50\_C04)_b$ are the largest (-2.74×10^{11} molecules /cm^2) and the $P(O_3)$ of high alkalinity and the coarse mode dominant dust mixtures $(Ca50A50(H1)Q0\_C04)_b$ and $(Ca50A50(H10)Q0\_C04)_b$ are the smallest (-4.39×10^{11} molecules /cm^2).
4. While the mixing of dust-BC pollutants decreases the concentration of OH and NO, it increases the concentration of NO_2 relative to that in the polluted (dust-free) environments through photolysis. In addition, while the concentrations of OH and NO are larger in internal mixing than in external mixing, the concentration of NO_2 is larger in external mixing than in internal mixing because the J-values of groups I and II decrease more in external mixing than in internal mixing. The difference between the $P(O_3)$ of the two mixing states is the largest below the dust layer.
5. O_3, OH, NO, HNO_3, SO_2 decrease through both mechanisms. Because of a sudden dip in the vertical profiles of those photochemical species, changes in the concentration of such species are good indicators of the location of the dust layer. Even in in the case of strong vertical turbulent diffusion (kdv = 1.0×10^6 cm^2/s), the sudden dip in the HNO_3 profile can be detected.

This chapter concludes that a size-resolved mineralogical mixture of dust aerosols is required for an adequate assessment of the impact of mineral dust on the

photochemical cycle because the shift in the size distribution to a fine mode enhances both photolysis and heterogeneous loss. In addition, the mass fraction of clay aggregates to the entire dust mixture is important in the light absorption of mineral dust aerosols because the fraction of iron oxide to the entire dust mixture is dependent on the mass fraction of clay aggregates. Therefore, the mass fraction of individual minerals is important in light absorbing properties as well as in gaseous uptake properties by mineral dust aerosols.

Finally, the heterogeneous loss rate is the dominant mechanism in the impact of dust on atmospheric photochemistry. Hence, if the extent of the impact is to be better understood, it is crucial that more realistic heterogeneous loss rates, taking into account the life cycle of dust (i.e., dust aging and transport processes), be estimated.

CHAPTER V

CONCLUSIONS

The main properties of mineral dust that perturb the atmospheric photochemistry field through photolysis and heterogeneous loss are spectral light absorption/scattering and gaseous uptakes, respectively. Both mechanisms strongly depend on the size and the composition of dust particles. This thesis has addressed the importance of a size-resolved mineralogical mixture of dust species in photolysis, heterogeneous reactions, and atmospheric photochemistry.

A new approach was used to treat dust aerosol particles in the photochemistry model. The dust mixtures were built by introducing a size-resolved mineralogical composition such as iron oxide in clay aggregates, carbonate containing minerals, and quartz. New data available on the iron oxide content in clay aggregates and the amount of calcite were used, as were the dust size distributions published from past field experiments and modeling studies. This approach led to the examination of the effect of size-resolved mineralogical mixtures on spectral actinic fluxes and gaseous uptakes in a consistent manner. This study then investigated changes in the vertical profiles of photolysis rates and heterogeneous loss rates due to dust mixtures and then demonstrated how the size-resolved mineralogical mixture of dust aerosols changed the vertical distribution of photochemical species relative to those in clean or polluted marine environments.

Several interesting findings arose during the pursuit of the goals of this thesis. One was that spectral actinic fluxes and photolysis rates changed as a function of differing size and composition of mineral dust aerosols and their mixing with BC and other types of aerosols. Another was that heterogeneous loss rates varied according to the

size-resolved mineralogical mixtures. Finally, in order to examine how these two effects influence photochemistry, this study introduced the newly-developed photochemistry model, DUST-CHEM.

With regard to the first of the findings listed above, this study found that dust size distributions are as important as iron oxide content in clay aggregates of dust particle aerosols in spectral absorption and scattering in UV and visible regions. As the size distribution shifts to the fine mode, the wavelength-dependence of optical properties becomes large. In a reference case of H1 (low absorbing) dust particles, the combined features of size distribution and mineralogical composition are that the H10_C04 size distribution shows the largest absorption in the UV region, and the H1_B02 size distribution shows the largest scattering in the visible region. However, the mixing state of a dust-BC mixture makes a relatively small difference in its spectral optical properties or the effective spectral optical properties. When a dust-BC mixture is assumed to externally mix with other types of aerosols in the polluted marine environment, the effective single scattering albedo is larger than the single scattering albedo of the dust-BC mixtures in the UV region. The former becomes smaller than the latter in the visible region because non-absorbing aerosols enhance scattering in the UV and shorter visible regions.

The second finding is that the spectral optical properties of mineral dust result in distinct changes in spectral actinic fluxes $\Delta F(\lambda)$ relative to the clean marine atmosphere in both clean and polluted marine environments. These changes $\Delta F(\lambda)$ can be either negative or positive. The transition point λ_{tp}, at which the sign of $\Delta F(\lambda)$ changes, moves to longer wavelengths as the dust load increases, a dust size distribution shifts to a coarse size mode, and the iron oxide content in the dust aggregates increases. For a given dust-laden condition, λ_{tp} also changes with the sun's position (i.e., time of day) and altitude.

The third finding is that dust-induced changes in actinic fluxes affect J-values differently, depending on the photolytic wavelength range of a given gas. Among the 13

photolysis reactions, group I consisted of $J[O_3(O^1D)]$, $J[N_2O_5]$, $J[HNO_3]$, $J[HO_2NO_2]$, $J[H_2O_2]$, $J[CH_3OOH]$, $J[CH_2O(HCO)]$, and $J[CH_2O(H_2)]$, photolytic wavelengths that are in the UV region (210 - 380nm); group II consisted of $J[NO_2]$ and $J[HNO_2]$ in the UV and the shorter visible region (310 - 420nm), and group III consisted of $J[O_3(O^3P)]$ and $J[NO_3]$ in the longer visible region (410 - 730nm).

The values of ΔJs in group I are negative through the lower atmosphere. Group II has negative ΔJs in and below the dust layer, but ΔJs become positive above the dust layer with the B02 particle size distribution and low absorbing dust (H1). In contrast, the ΔJs of group III are positive for all size distributions considered for H1 dust, and they become negative as the iron oxide content increases. The changes in the vertical profiles of the ΔJ values are the largest in group I for any changes in the microphysical and chemical properties of mineral dust. The FCJs in group I at the surface fell between about -31% and -47.3%.

The temporal behavior of ΔJ of a given group is similar among the various size distributions and compositions of dust. The lowest values of ΔJ in groups I, II, and III appear at about noon, 4pm, and 6pm, respectively. However, the values of ΔJ vary by a factor of 1.5 to 2.0, depending on the dust properties. In all the cases, the largest changes in ΔJ are caused by the B02 or O98 size distribution. The J-values of groups I and II are the most sensitive to the varying amounts of iron oxide in the range of 1% to 5%, whereas group III is sensitive to the entire range (1% to 10%).

When dust mixes with a high concentration of BC, the external mixing state causes more negative values of FCJs in groups I and II. In the considered range of the microphysical and chemical parameters of dust particles, we found that the mineralogical composition and size distribution are equally important in controlling spectral actinic fluxes and photolysis rates; however, the mixing state is of relatively little importance.

The fourth finding is the importance of the relative contribution of individual mineral species to the overall heterogeneous loss rate. Mineral dust is assumed to be an

external mixture of three mineral species--iron oxide-clay aggregates, carbonate-containing minerals, and quartz--considering the light absorption and alkalinity of dust aerosols in a size-resolved manner. The selection of the mass fraction and uptake coefficients of each mineral species is based on field, laboratory, and modeling studies. If this approach is used, the limitations of past studies that use one-value parameterization of the uptake coefficient for mineral dust, so-called multi-component aerosols, can be overcome. This study found that the overall heterogeneous loss rates are determined by the mineral species with high uptake coefficients. The gaseous loss on mineral dust aerosols is caused not only by the alkalinity of dust particles (carbonate-containing minerals) but also by the reducing capacity of dust particles.

The fifth finding is the importance of the size distribution of mineral dust aerosols in heterogeneous loss rates. Due to differences in the dust size distribution, $k_{loss,j}$ changes by a factor of five to ten. As the fine mode mass fraction of mineral dust increases, $k_{loss,j}$ increases. The larger the $k_{loss,j}$, the larger the rate of change in $k_{loss,j}$ over fine mode fractions, which are mainly determined by mineral species with large uptake coefficients. Therefore, among the four gaseous loss reactions considered, HNO_3 loss is the most favorable in the fine mode. Abrupt changes in the vertical profiles of HNO_3, which can be observed by satellites and aircraft, might be good indicators of the location of the dust layer.

Using the results of photolysis and heterogeneous reactions, this study was the first to investigate the contributions of the two mechanisms to atmospheric photochemistry for the same size-resolved mineralogical mixtures of dust particles. The DUST-CHEM model was built by incorporating a new dust module into a 1-D photochemistry model. The dust module includes the vertical profiles of J-values and heterogeneous loss rates given the dust mixtures, consisting of a combination of calcite, clay aggregates, hematite, quartz, and particle size distributions.

The sixth finding concerns the relative roles of photolysis and heterogeneous loss in photochemical species. The vertical profiles of the species primarily change due to photolysis when they are closest to the surface and due to heterogeneous loss when they are in the middle of the dust layer due. For OH, HNO_3, and SO_2, both photolysis and heterogeneous loss enhance the reduction of concentrations. For O_3, NO_2, and NO, the two mechanisms act in opposite directions. The ratios of the contribution of photolysis to heterogeneous loss for changes in concentrations is 0.04 to 0.27 for O_3, 0.001 to 0.004 for HNO_3, and 0.02 to 0.2 for SO_2 which are heterogeneous process dominant by 1 to 3 orders of magnitude. The ratio of the contribution of photolysis to heterogeneous loss is also 0.7 to 3.8 for OH, 0.7 to 9.8 for NO, and 0.26 to 2.23 for NO_2. The upper bound of the ratio indicates that the B02 size distribution enhances the role of photolysis in atmospheric photochemistry.

The seventh finding is that the differences in microphysical and chemical properties of dust aerosols such as light absorption, alkalinity, and size distribution, are important to the variation in the vertical profiles of individual species. The concentration of HNO_3 is the most sensitive to the properties of dust aerosols in the middle of dust layer with coefficient of variation of 80%. Through photolysis, the B02 size distribution results in peculiar vertical distributions of species. However, light absorption only slightly affects the vertical profiles of the species. Through heterogeneous loss, alkalinity is as important as the dust size distribution. Hence, the dust size distribution is the most significant controlling factor of dust aerosols on photochemistry.

This thesis demonstrates that the impact of dust aerosols on atmospheric photochemistry, although not simple, exhibits a clear association with the size-resolved mineralogical composition. The dust mixtures introduced in this thesis capture the roles of mineralogical species, which are either active or inactive in both the radiation and chemistry fields. For HNO_3 loss, clay aggregates are important to gaseous uptake and photolysis rates, but quartz is insignificant in both mechanisms. Such roles can be tied to

the size-resolved properties of dust particles. In particular, the fine mode dominant size distribution enhances the impact of dust through either photolysis (light absorption/scattering) or heterogeneous loss (gaseous uptake). Thus, this thesis emphasizes the significance of the dust size distribution and also underscores the importance of the accurate measurement of the dust size distribution and the mineralogical composition as well as the careful selection of these properties in the modeling of the impact of dust aerosols on atmospheric photochemistry.

In the future, this thesis can be extended to detailed studies for the purpose of improving the assessment of the impact of dust in chemistry and climate modeling. In Chapter 2, the mixing of dust and BC was treated in a simple assumption, so-called "volume average mixing," for the photolysis study. A more realistic and sophisticated method such as core-shell mixing, Bruggman approximation, or discrete dipole approximation (DDA) can be used with additional microphysical and chemical properties of dust, BC, and non-absorbing aerosols.

In Chapter 3, overall heterogeneous loss rates were calculated as a snapshot of gaseous uptake by "pure" mineral dust species. During transport in the atmosphere, the mixing of mineral dust with other aerosols can cause the contamination of the surface of the mineral dust particles. Since some uptake coefficients are very sensitive to relative humidity, the heterogeneous loss rate needs to be estimated as a surface limited loss rate on dust particles such as $k_{loss,j} = f(RH, time)$.

In Chapter 4, the results of DUST-CHEM showed the distinct effects of the size-resolved mineralogical mixture of dust aerosols on the vertical distribution of photochemical species in a 1-D stable marine environment. Considering the differences in the size and composition of mineral dust aerosols, dust mixtures need to be well-posed in the dust-chemistry-climate system, which should lead to the estimation of realistic dust-chemistry interactions.

Considering the several roles of mineral dust in the aerosol-chemistry-climate system, one can feasibly assess radiative forcing with well-posed mineral dust, Figure 5.1 shows the dust properties and the impact of mineral dust aerosols on climate systems. The transformation of dust particles due to aging or mixing changes the size and the mineralogical composition of dust aerosols with time and space, which leads to the modification of other dust properties such as radiative and hygroscopic properties and the re-establishment of aerosol-chemistry interactions. Once heterogeneous chemistry modeling is improved, radiative, photochemical, and hydrological feedback within the chemistry-aerosol-climate system can be adequately assessed.

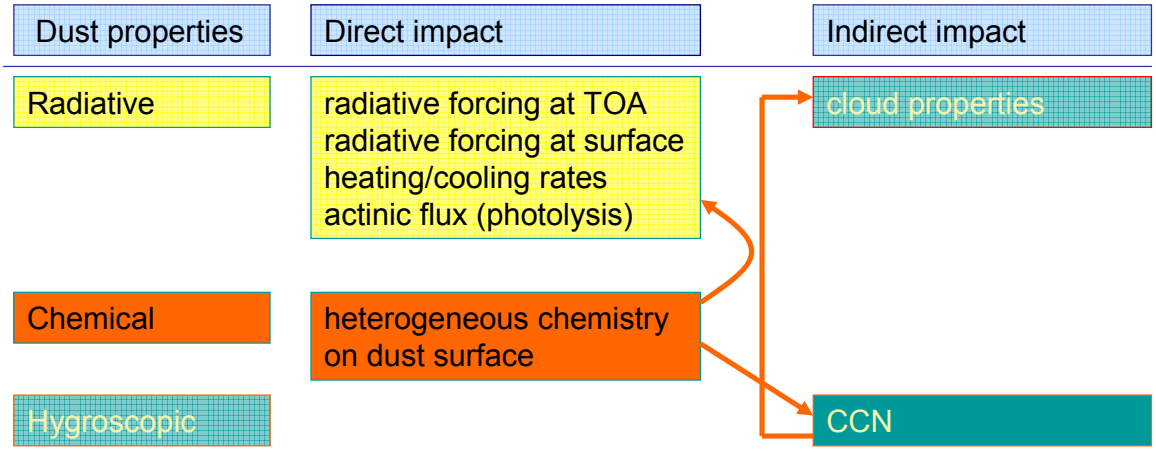

Figure 5.1 The properties and impact of mineral dust aerosols on climate systems

APPENDIX A
Number, area, mass size distribution of dust particles analized in this study (see Chapter 2, Table 2.3)

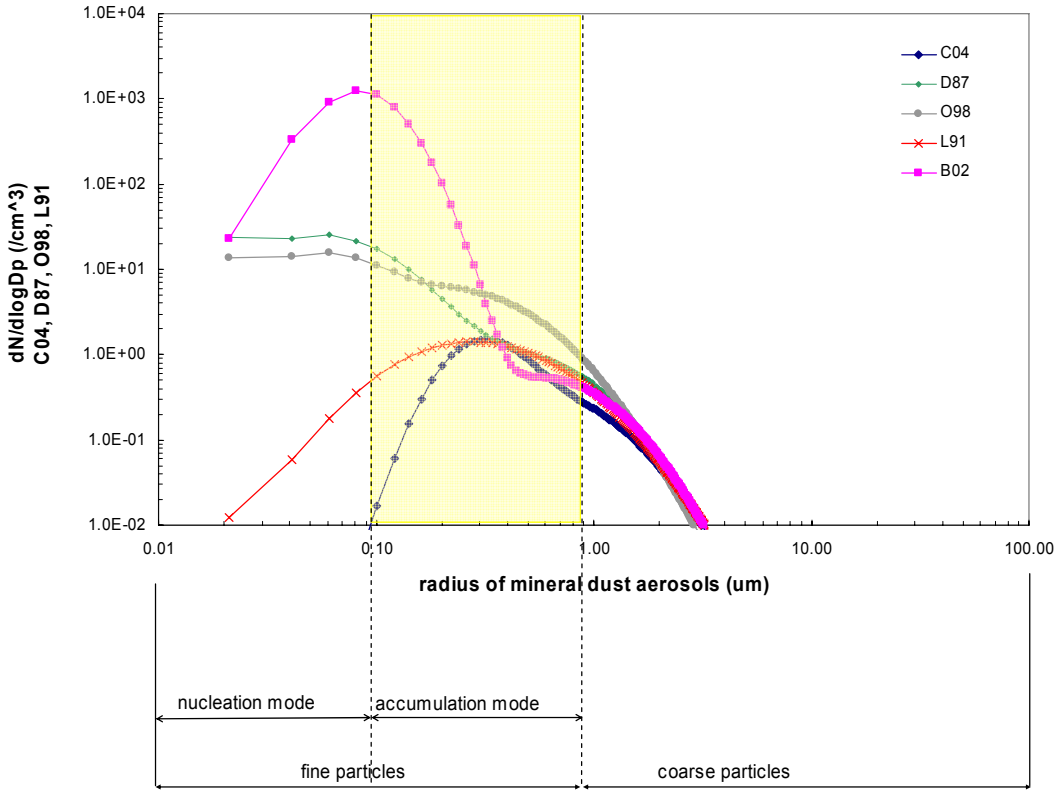

Figure A1. Comparison of five number size distributions of dust particles. Notations are same as in Table 2.3 Mass concentration of dust is 1000 $\mu g/m^3$.

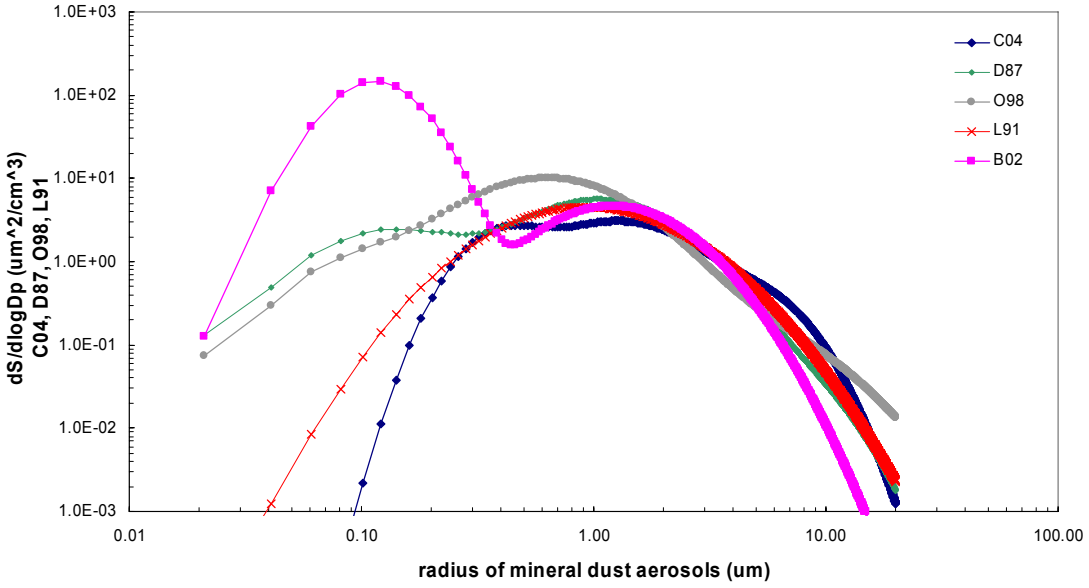

Figure A2. Same as Figure A1, except for particle surface area size distributions.

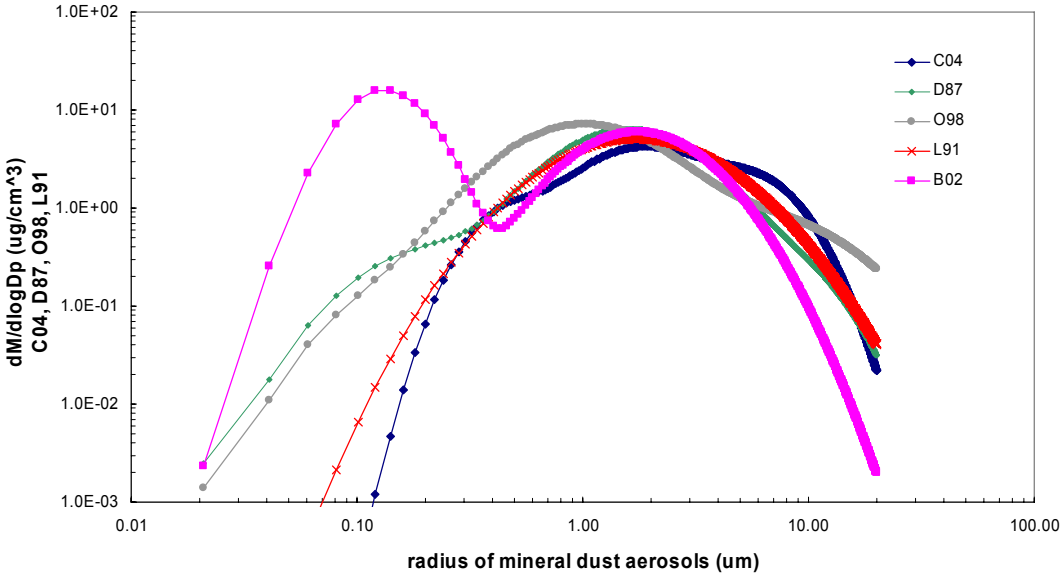

Figure A3. Same as Figure A1, except for particle mass size distributions.

APPENDIX B

CHEMICAL REACTIONS USED IN THE DUST-CHEM

K = A * (300 / T)**B * EXP(C / T)

G1 = ATKINSON ET AL. (1997) J. PHYS. CHEM. REF. DATA 26, 521 - 1011
G2 = DEMORE ET AL. (1997) CHEMICAL KINETICS AND PHOTOCHEMICAL DATA FOR USE IN STRATOSPHERIC MODELING. EVAL #12. JPL.
G3 = GERY ET. AL., [1989] JGR VOL. 94, NO. D10, P. 12,925-12,956
G7 = SANDER ET AL, (2006) CHEMICAL KINETICS AND PHOTOCHEMICAL DATA FOR USE IN STRATOSPHERIC MODELING. EVAL #15. JPL.
G8 = STOCKWELL W. R. (1995) ON THE HO2 + HO2 REACTION: ITS MISAPPLICATION IN ATMOSPHERIC CHEMISTRY MODELS. J. GEOPHYS. RES. 100, 11,695 - 11,698.
L = Lucas (2004)

Table B1 Gaseous chemistry reactions (O_x cycle)

No	Reaction								A	B	C	reference
R1	$O[^3P]$	+	O_2	M	→	O_3			6.00E-34	2.4		G7
R2	$O[^3P]$	+	O_3		→	O_2	+	O_2	8.00E-12		-2060	G1
R3	$O[^1D]$			O_2	→	$O[^3P]$			3.30E-11		55	G7
R4	$O[^1D]$			N_2	→	$O[^3P]$			2.15E-11		110	G7
R5	$O[^1D]$	+	H_2O		→	2 OH			1.63E-10		60	G7
R6	$O[^1D]$	+	H_2		→	OH	+	H	1.10E-10			G1

Table B2 Gaseous chemical reactions (HO_x cycle)

No	Reaction								A	B	C		reference
R7	H	+	O_2	M	→	HO_2	+		4.40E-32	1.3			G7
R8	H	+	O_2		→	HO_2	+		4.70E-11	0.2			G7
R9	H	+	O_3		→	OH	+	O_2	1.40E-10		-470		G2
R10	H	+	HO_2		→	H_2	+	O_2	6.90E-12				G7
R11	H	+	HO_2		→	OH	+	OH	7.20E-11				G1
R12	H	+	HO_2		→	H_2O	+	$O[^3P]$	1.60E-12				G7
R13	OH	+	$O[^3P]$		→	H	+	O_2	2.20E-11		120		G7
R14	OH	+	O_3		→	HO_2	+	O_2	1.70E-12		-940		G7
R15	OH	+	H_2		→	H_2O	+	H	2.80E-12		-1800		G7
R16	OH	+	OH		→	H_2O	+	$O[^3P]$	1.80E-12				G7
R17	OH	+	HO_2		→	H_2O	+	O_2	4.80E-11		250		G1
R18	OH	+	H_2O_2		→	HO_2	+	H_2O	2.80E-12				G7
R19	H_2O_2	+	$O[^3P]$		→	OH	+	HO_2	1.40E-12		-2000		G1
R20	OH	+	OH	M	→	H_2O_2			6.90E-31	1.0		0.60	G7
R21	OH	+	OH		→	H_2O_2			2.60E-11				G1
R22	HO_2	+	$O[^3P]$		→	OH	+	O_2	3.00E-11		200		G7
R23	HO_2	+	O_3		→	OH	+	2 O_2	1.00E-14		-490		G7
R24	HO_2	+	HO_2		→	H_2O_2	+	O_2	3.50E-13		430		G7,G8
R25	HO_2	+	HO_2		→	H_2O_2	+	O_2	1.70E-33		1000		G2,G8
R26	HO_2	+	HO_2		→	H_2O_2	+	O_2	4.90E-32				G7,G8

Table B3 Gaseous chemical reactions (NO_x cycle)

No	Reaction										A	B	C		reference
R27	OH	+	NO	N_2	→	HONO					7.00E-31	2.6		0.60	G7
R28	OH	+	NO		→	HONO					3.60E-11	0.1			G7
R29	OH	+	HONO		→	NO_2	+	H_2O			1.80E-11		-390		G7
R30	OH	+	NO_2	N_2	→	HNO_3					1.80E-30	3.0		0.43	G7
R31	OH	+	NO_2		→	HNO_3					2.80E-11				G7
R32	OH	+	HNO_3		→	NO_3	+	H_2O			2.40E-14		460		G7
R33	OH	+	HNO_3		→	NO_3	+	H_2O			2.70E-17		2199		G7
R34	OH	+	HNO_3	M	→	NO_3	+	H_2O			6.50E-34		1335		G7
R35	OH	+	NO_3		→	HO_2	+	NO_2			2.20E-11				G7
R36	HO_2	+	NO		→	OH	+	NO_2			3.50E-12		250		G7
R37	HO_2	+	NO_2	M	→	HO_2NO_2					2.00E-31	3.4		0.60	G7,G2
R38	HO_2	+	NO_2		→	HO_2NO_2					2.90E-12	1.1			G7,G2
R39	HO_2	+	NO_3		→	HNO_3	+	O_2			3.50E-12				G7
R40	HO_2NO_2	+		M	→	HO_2	+	NO_2			5.00E-6		-10000		G1
R41	HO_2NO_2	+			→	HO_2	+	NO_2			2.60E+15		-10900		G1
R42	HO_2NO_2	+	OH		→	HO_2	+	H_2O	+	O_2	1.30E-12		380		G7
R43	NO	+	$O[^3P]$	M	→	NO_2					9.00E-32	1.5			G7
R44	NO	+	$O[^3P]$		→	NO_2					3.00E-11	0.0			G7
R45	NO	+	O_3		→	NO_2	+	O_2			3.00E-12		-1500		G7
R46	NO_2	+	$O[^3P]$		→	NO	+	O_2			5.10E-12		210		G7
R47	NO_2	+	$O[^3P]$	M	→	NO_3					2.50E-31	1.5			G7
R48	NO_2	+	$O[^3P]$		→	NO_3					3.00E-11				G7
R49	NO_2	+	O_3		→	NO_3	+	O_2			1.20E-13		-2450		G1
R50	NO_3	+	$O[^3P]$		→	NO_2	+	O_2			1.00E-11				G1

Table B4 Gaseous chemical reactions (CH_4 oxidation)

No	Reaction									A	B	C		reference
R51	NO_3	+	NO		→	$2NO_2$				1.50E-11		170		G7
R52	NO_3	+	NO_2	N_2	→	N_2O_5				2.00E-30	4.4		0.33	G7
R53	NO_3	+	NO_2		→	N_2O_5	+	O_2		1.40E-12	0.7			G7
R54	N_2O_5	+		N_2	→	NO_3	+	NO_2		1.10E-03	3.5	-11000	0.33	G1
R55	N_2O_5	+			→	NO_3	+	NO_2		9.70E+14	-0.1	-11080		G1
R56	N_2O_5	+	H_2O		→	$2HNO_3$				2.00E-21				G1
R57	CH_4	+	$O[^1D]$		→	CH_2O	+	H_2		1.50E-10				G7
R58	CH_4	+	$O[^1D]$		→	CH_3	+	OH		1.50E-10				G7
R58	CH_4	+	$O[^1D]$		→	CH_3O				1.50E-10				G7
R59	OH	+	CH_4		→	CH_3	+	H_2O		2.45E-12		-1775		G7
R60	CH_3	+	O_2	N_2	→	CH_3O_2				4.00E-31	3.6			G7
R61	CH_3	+	O_2		→	CH_3O_2				1.20E-12	-1.1			G7
R62	CH_3O_2	+	CH_3O_2		→	CH_3O	+	CH_3O	+ O_2	9.50E-14		390		G7
R63	CH_3O_2	+	NO		→	CH_3O	+	NO_2		2.80E-12		300		G7
R64	CH_3O_2	+	HO_2		→	CH_3OOH	+	O_2		4.10E-13		750		G7
R65	CH_3OOH	+	OH		→	CH_3O_2	+	H_2O		3.80E-12		200		G7
R66	CH_3O	+	O_2		→	CH_2O	+	HO_2		3.90E-14		-900		G7
R67	CH_2O	+	NO_3		→	HCO	+	HNO_3		5.80E-16				G1
R68	CH_2O	+	$O[^3P]$	O2	→	OH	+	HO_2	+ CO	3.40E-11		-1600		G2
R69	CH_2O	+	OH		→	HCO	+	H_2O		5.50E-12		125		G7
R70	CH_2O	+	HO_2		→	$HOCH_2O_2$				6.70E-15		600		G7
R71	$HOCH_2O_2$	+			→	HO_2	+	CH_2O		2.40E+12		-7000		G1
R72	$HOCH_2O_2$	+	NO	O2	→	NO_2	+	HO_2	+ HCOOH	7.00E-12				G3-CB45
R73	HCOOH	+	OH		→	H_2O	+	CO_2	+ HO_2	4.00E-13				G7
R74	CO	+	OH	O2	→	HO_2	+	CO_2		1.50E-13				G7

Table B5 Gaseous chemical reactions (Sulfur cycle)

No	Reaction							A	B	C	reference
R75	CH_3SCH_3	+	OH	→	CH_3SCH_2	+	H_2O	1.10E-11		-240	G7
R76	CH_3SCH_3	+	OH	→	$CH_3S(OH)CH_3$			6.00E-12			L
R77	$CH_3S(OH)CH_3$	+	O_2	→	$CH_3S(O)CH_3$	+	HO_2	9.60E-13			G7
R78	$CH_3S(OH)CH_3$	+		→	CH_3SOH	+	CH_3	5.00E+05			L
R79	$CH_3S(O)CH_3$	+	OH	→	$CH_3S(O)(OH)CH_3$			6.10E-12		800	G7
R80	$CH_3S(O)(OH)CH_3$	+	O_2	→	$CH_3S(O_2)CH_3$		HO_2	1.00E-13			L
R81	$CH_3S(O)(OH)CH_3$	+		→	$CH_3S(O)OH$	+	CH_3	2.00E+6			L
R82	$CH_3S(O)OH$	+	OH	→	CH_3SO_2	+	H_2O	9.00E-11			G7
R83	CH_3SCH_2	+	O_2	→	CH_3SCH_2OO			5.70E-12			G7
R84	CH_3SCH_2OO	+	NO	→	CH_3SCH_2O		NO_2	7.90E-12		128	L
R85	CH_3SCH_2O	+		→	CH_3S	+	CH_2O	3.30E+04			L
R86	CH_3SOH	+	OH	→	CH_3SO	+	H_2O	5.00E-11			L
R87	CH_3S	+	NO_2	→	CH_3SO	+	NO	3.00E-11		240	G7
R88	CH_3S	+	O_3	→	CH_3SO	+	O_2	1.50E-12		360	G7
R89	CH_3S	+	O_2	→	CH_3SOO	+		3.00E-18			G7
R90	CH_3SOO	+		→	CH_3S	+	O_2	1.50E+11		-3910	L
R91	CH_3SOO	+	NO	→	CH_3S	+	NO_2	1.10E-11			G7
R92	CH_3SOO	+	NO_2	→	$C_3SOO\ NO_2$	+		2.20E-11			G7
R93	$CH_3SOO\ NO_2$	+		→	CH_3SOO	+	NO_2	4.00E-03			L
R94	CH_3SO	+	NO_2	→	CH_3SO_2	+	NO	1.20E-11			G7
R95	CH_3SO	+	O_3	→	CH_3SO_2	+	O_2	4.00E-13			G7
R96	CH_3SO	+	O_2	→	$CH_3S(O)OO$	+		3.60E-16		1550	L
R97	$CH_3S(O)OO$	+		→	CH_3SO	+	O_2	3.90E+11		-3910	L
R98	$CH_3S(O)OO$	+	NO	→	CH_3SO_2	+	NO_2	8.00E-12			L
R99	$CH_3S(O)OO$	+	NO_2	→	$CH_3S(O)OO\ NO_2$	+		1.00E-12			L
R100	$CH_3S(O)OO\ NO_2$	+		→	$CH_3S(O)OO$	+	NO_2	4.20E-03			L

Table B5 Continued (Sulfur cycle)

No	Reaction										A	B	C	reference
R101	CH_3SO_2	+	NO_2		→	CH_3SO_3	+	NO			2.20E-12			L
R102	CH_3SO_2	+	O_3		→	CH_3SO_3	+	O_2			5.00E-15			L
R103	CH_3SO_2	+	OH		→	CH_3SO_3H	+				5.00E-11			L
R104	CH_3SO_2	+	O_2		→	$CH_3S(O_2)OO$	+				1.20E-16		1550	L
R105	$CH_3S(O_2)OO$	+			→	CH_3SO_2	+	O_2			1.30E+11		-3910	L
R106	$CH_3S(O_2)OO$	+	NO		→	CH_3SO_3	+	NO_2			1.00E-11			L
R107	$CH_3S(O_2)OO$	+	CH_3O_2		→	CH_3SO_3	+	CH_2O	+	HO_2	5.50E-12			L
R108	$CH_3S(O_2)OO$	+	NO_2		→	$CH_3S(O_2)OONO_2$	+				1.00E-12			L
R109	$CH_3S(O_2)OONO_2$	+			→	$CH_3S(O_2)OO$	+	NO_2			4.20E-03			L
R110	CH_3SO_2	+			→	CH_3	+	SO_2			2.72E-17			L
R111	CH_3SO_2	+			→	CH_3	+	SO_2			3.02E+14		-15320	L
R112	CH_3SO_3	+			→	CH_3	+	SO_3			1.60E-01			L
R113	CH_3SO_3	+	HO_2		→	CH_3SO_3H	+	O_2			5.00E-11			L
R114	SO_2	+	OH	M	→	HSO_3	+				3.30E-31	4.3		G7
R115	SO_2	+	OH		→	HSO_3	+				1.60E-12			G7
R116	HSO_3	+	O_2		→	SO_3	+	HO_2	+		1.30E-12		-330	L
R117	SO_3	+	H_2O		→	H_2SO_4	+		+		1.20E-15			L
R118	CH_3SOO	+			→	CH_3SO_2	+		+		1.00E+00		-650	L
R119	$CH_3S(O)OO$	+			→	CH_3SO_3	+		+		0.80E+00		-650	L
R120	$CH_3S(O)OH$	+	O_3		→	CH_3SO_3H	+	O_2	+		1.00E-06		-1200	L
R121	CH_3SOH	+	O_2		→	CH_3SO_3H	+		+		5.00E-05			L
R122	SO_2	+	$O[^3P]$	N_2	→	SO_3	+		+		1.80E-33	-2		G7
R122	SO_2	+	$O[^3P]$		→	SO_3	+		+		4.20E-14	-1.8		G7
R123	SO_2	+	HO_2		→	SO_3	+	OH	+		1.00E-18			G7
R124	OCS	+	$O[^3P]$		→	SO	+	CO	+		2.10E-11		-2200	L

Table B5 Continued (Sulfur cycle)

No	Reaction								A	B	C	Reference
R125	OCS	+	OH	→	HS	+	CO_2	+	1.10E-13		-1200	G7
R126	CS_2	+	$O[^3P]$	→	SO	+	CS	+	3.20E-11		-650	G7
R127	CS_2	+	$O[^3P]$	→	OCS	+	S	+	2.98E-12		-650	L
R128	CS_2	+	OH	→	CS_2OH	+		+	1.25E-16		4550	G7
R129	CS_2OH	+		→	OCS	+	SO_2	+ HO_2	3.00E-12			L
R130	HSO_3	+	OH	→	SO_3	+	H_2O	+	1.00E-11			L
R131	H_2S	+	$O[^3P]$	→	OH	+	HS	+	9.20E-12		-1810	G7
R132	H_2S	+	OH	→	HS	+	H_2O	+	6.10E-12		-75	G7
R133	S	+	O_2	→	SO	+	$O[^3P]$	+	2.30E-12			G7
R134	SO	+	O_2	→	SO_2	+	$O[^3P]$	+	1.25E-13		-2190	G7
R135	SO	+	O_3	→	SO_2	+	O_2	+	3.40E-12		-1100	G7
R136	SO	+	NO_2	→	SO_2	+	NO	+	1.40E-11			G7
R137	CS_2	+	OH	→	OCS	+	HS	+	3.28E-12			L
R138	H_2S	+	$O[^3P]$	→	OH	+	HS	+	9.20E-12		-1810	L
R139	H_2S	+	OH	→	HS	+	H_2O	+	6.00E-12		-75	L
R140	HS	+	HS	→	H_2S	+	S	+	1.50E-11			L
R141	HS	+	O_2	→	SO	+	OH	+	4.00E-19			G7
R142	HS	+	HO_2	→	H_2S	+	O_2	+	3.00E-11			L
R143	CS	+	O_2	→	SO	+	CO	+	5.00E-20			L
R144	CS	+	O_2	→	OCS	+	$O[^3P]$	+	2.90E-19			G7
R145	CS	+	OH	→	HS	+	CO	+	1.00E-11			L

Table B6 Photodissociations

No	Reaction						A	B	C	reference
J1	O_3	+	→	$O[^3P]$	+	O_2				
J2	O_3	+	→	$O[^1D]$	+	O_2				
J3	NO_2	+	→	NO	+	$O[^3P]$				
J4	NO_3	+	→	NO_2	+	$O[^3P]$				
J5	NO_3	+	→	NO	+	O_2				
J6	HONO	+	→	OH	+	NO				
J7	N_2O_5	+	→	NO_2	+	NO_3				
J8	HNO_3	+	→	OH	+	NO_2				
J9	HO_2NO_2	+	→	HO_2	+	NO_2				
J10	H_2O_2	+	→	2OH	+					
J11	CH_3OOH	+	→	CH_3O	+	OH				
J12	CH_2O	+	→	$2HO_2$	+	CO				
J13	CH_2O	+	→	CO	+	H_2				

Table B7 Heterogeneous reactions on dust particle surfaces

No	Reaction						A	B	C	reference
H1	O_3		→	$1.5O_2$						
H2	SO_2		→	SULFATE						
H3	NO_2		→	0.5NITRITE	+	0.5NITRATE				
H4	HNO_3		→	NITRATE						

APPENDIX C

INITIAL CONCENTRATION

Table C1 Initial volume mixing ratio of gaseous species, deposition velocity, emission and top flux.

Species	Clean marine (SAGA3)	(PEM-tropicsB)	Polluted marine (TRACE-P)	Deposition velocity (cm/s)	Emission from Surface (#/cm^2/s)	Top flux (#/cm^2/s)
NO	**1.40 (pptv)**	**10.00 (pptv)**	**30.00 (pptv)**	**0.1 (P)**	**8.2 E7(T)**	**0.40E+08 (T)**
NO2	**4.80 (pptv)**	**10.00 (pptv)**	**60.00 (pptv)**	**0.1 (P)**		**0.40E+08 (T)**
NO3	4.00E-3 (pptv)	4.00E-3 (pptv)	700.00 (pptv)	**0.4 (P)**		**0.40E+08 (T)**
HNO3	26.00 (pptv)	**60.00 (pptv)**	**300.00 (pptv)**	**1.0 (K)**		**0.40E+08 (T)**
O3	**20.00 (ppbv)**	**28.00(ppbv)**	**53..00 (ppbv)**	**0.05 (K)**		
H2O2	**580.00 (pptv)**	**670.00 (pptv)**	850.0 (pptv)	**1.0 (K)**		
CH3OOH	**640.00 (pptv)**	**660.00 (pptv)**	1000.00 (pptv)	**0..35 (K)**		
CH2O	87.00 (pptv)	**200.00 (pptv)**	200.000 (pptv)			
SO2	**10.00 (pptv)**	**57.00 (pptv)**	**875.00 (pptv)**		**0.1 (T)**	
H2SO4	0.30 (pptv)	**0.30 (pptv)**	**0.48 (pptv)**	0.8 (P)		
OCS	516.0 (pptv)	516.0 (pptv)	**523.00 (pptv)**			
CH3SCH3 (DMS)	**200~500(pptv)**	**166.18 (pptv)**	**3.82 (pptv)**		**7.6 E9 (T)**	
CH3SO3H (MSA)	170 (pptv)	**0.65 (pptv)**	**0.37 (pptv)**			
CH3S(O)CH3	4.50 (pptv)	**4.50 (pptv)**	4.50 (pptv)			
CH4	**1800 (pptv)**	1800 (pptv)	**1800 (pptv)**			
CO2	340.0 (ppmv)	**368.00 (ppmv)**	**374.00 (ppmv)**			
CO	**60-80 (ppbv)**	**80.00 (ppbv)**	**167.50 (ppbv)**		1.2 E11(T)	
CH3CHO	10.1 (pptv)	10.1 (pptv)	10.1 (pptv)			
HCOOH	1.80 (ppbv)	1.80 (ppbv)	1.80 (ppbv)			
H2S					5.3E7 (T)	
HONO					5.8E7 (T)	

T: Thompson et al., 1993
K: Kuhlmann et al., 2003
P: Pender et al., 1994

APPENDIX D

DIURNAL CYCLES OF GASEOUS SPECIES

(a)

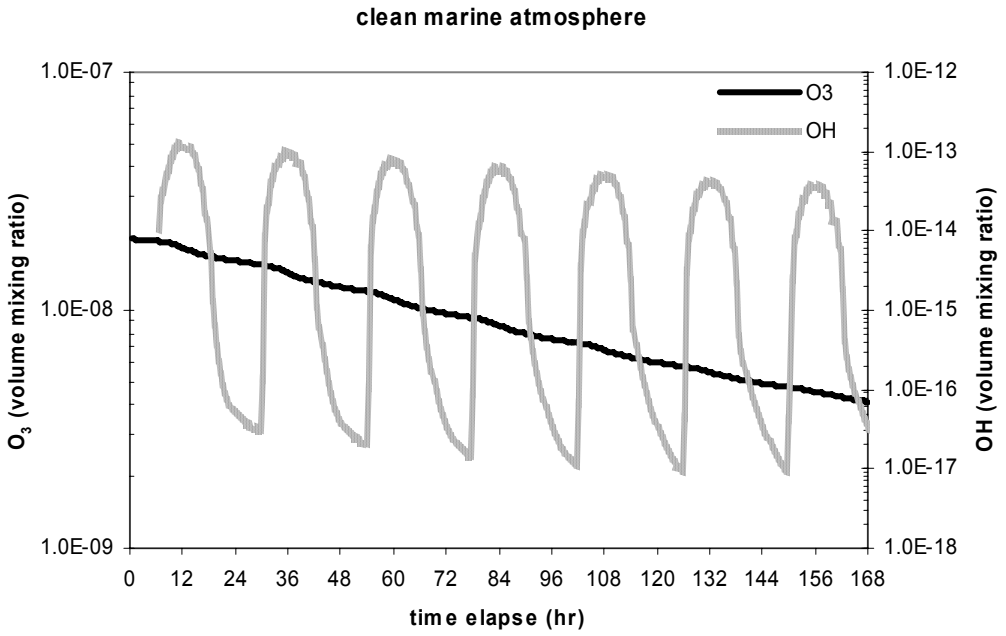

(b)

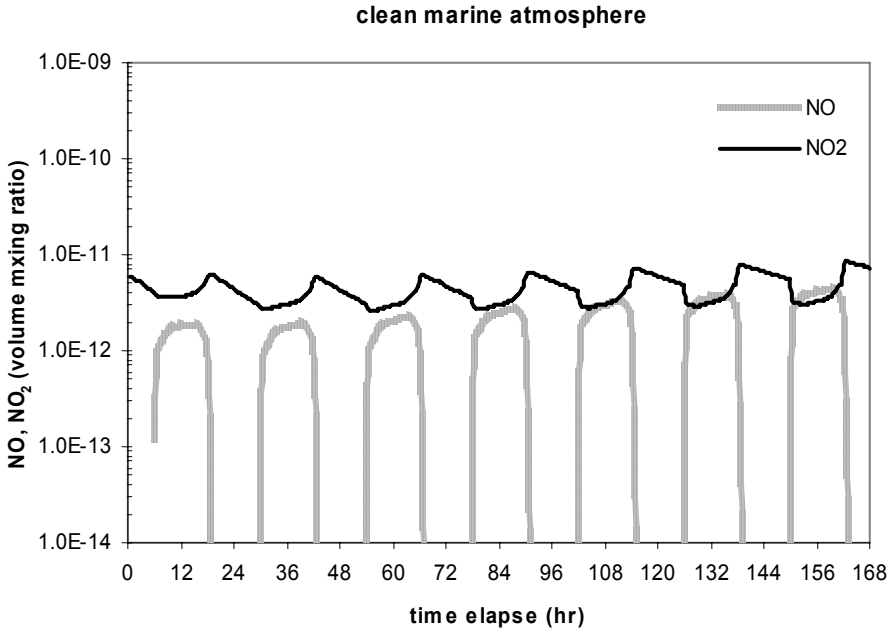

Figure D.1: Diurnal cycle of atmospheric photochemical species at surface in the clean marine environments. (a) O_3 and OH, (b) NO and NO_2

(c)

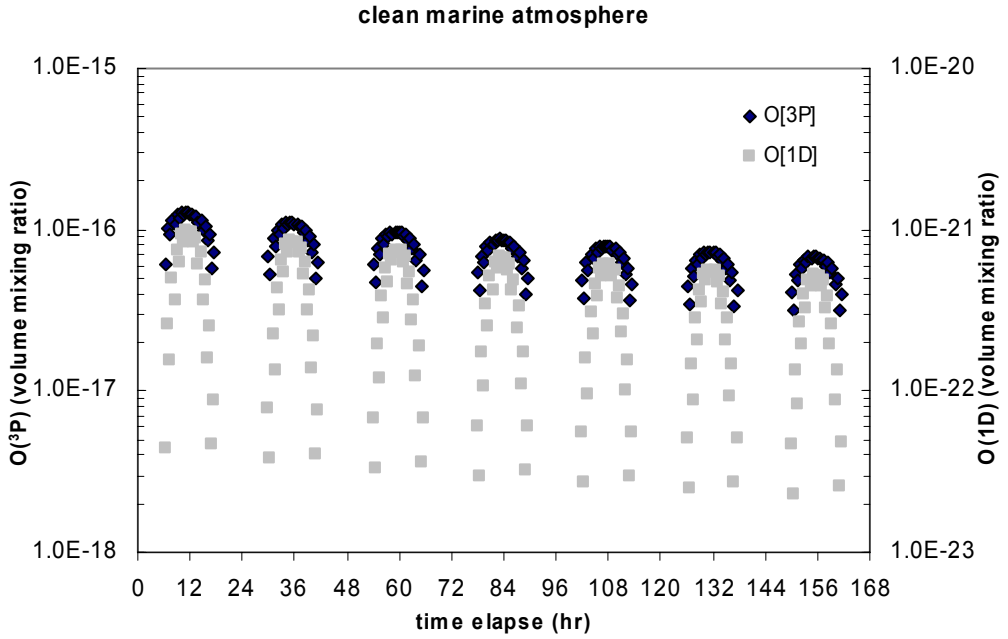

(d)

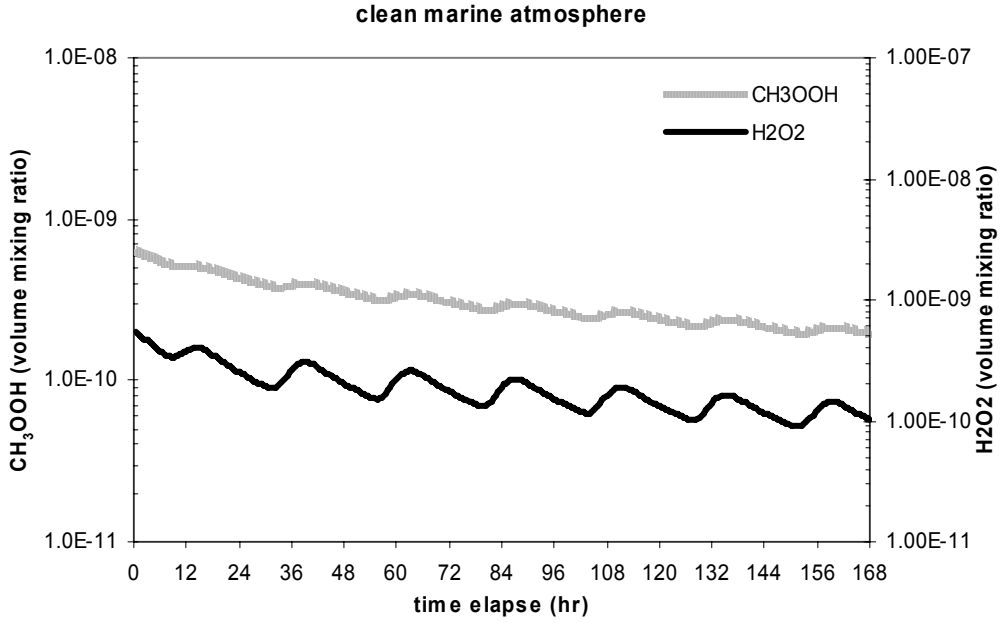

Figure D.1: Continued. (c) $O(^3P)$ and $O(^1D)$, (d) CH_3OOH and H_2O_2

(e)

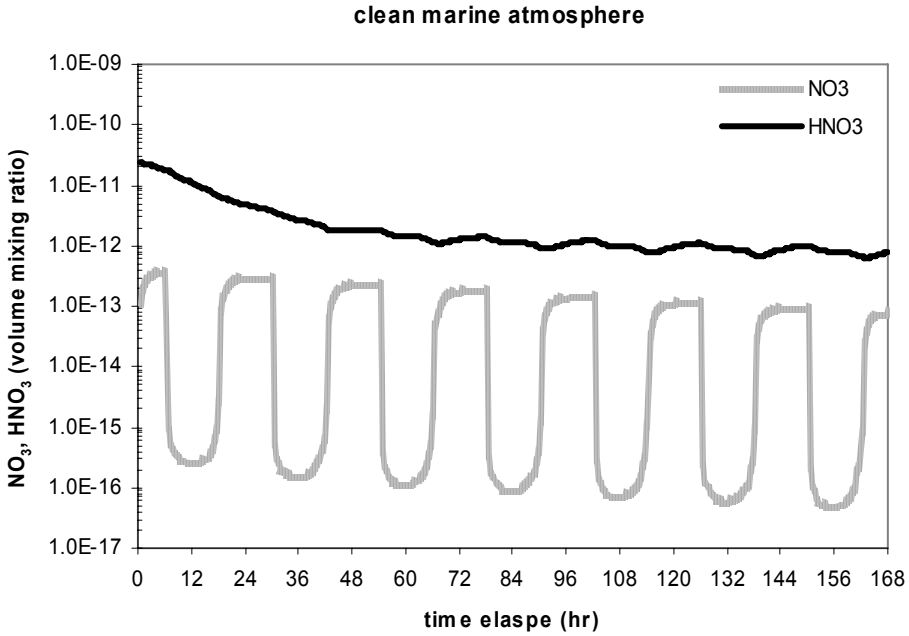

(f)

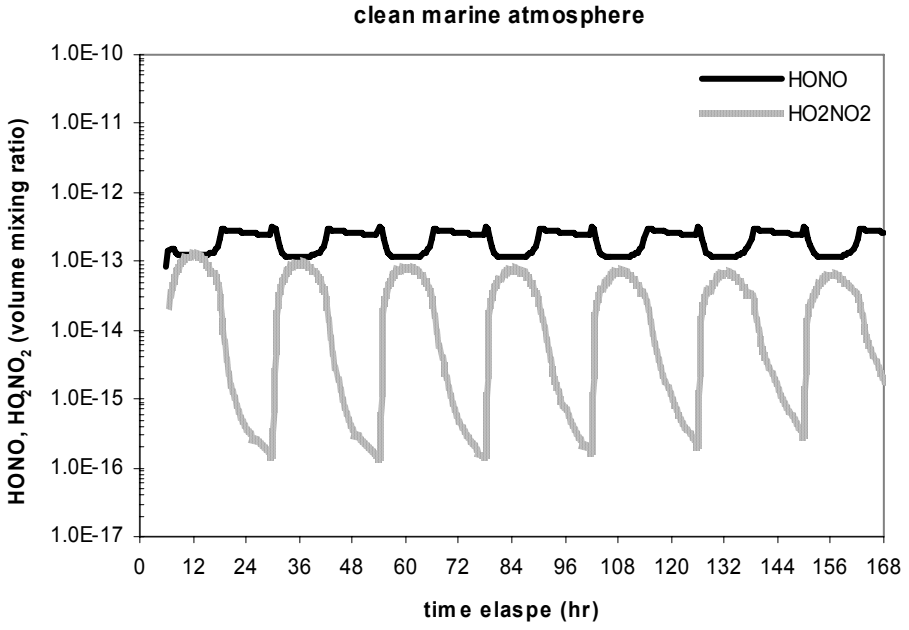

Figure D.1: Continued. (e) NO_3 and HNO_3, (f) HONO and HO_2NO_2

(g)

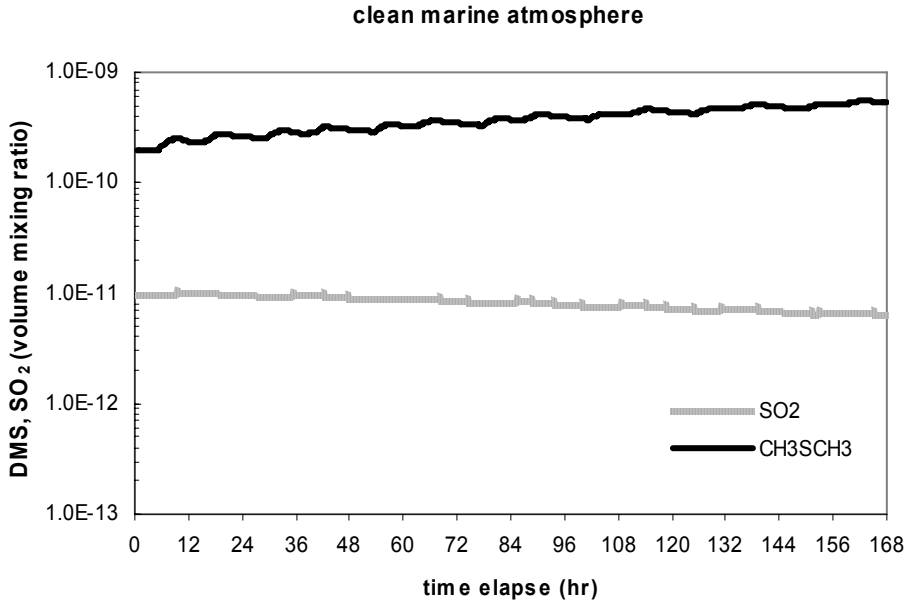

(h)

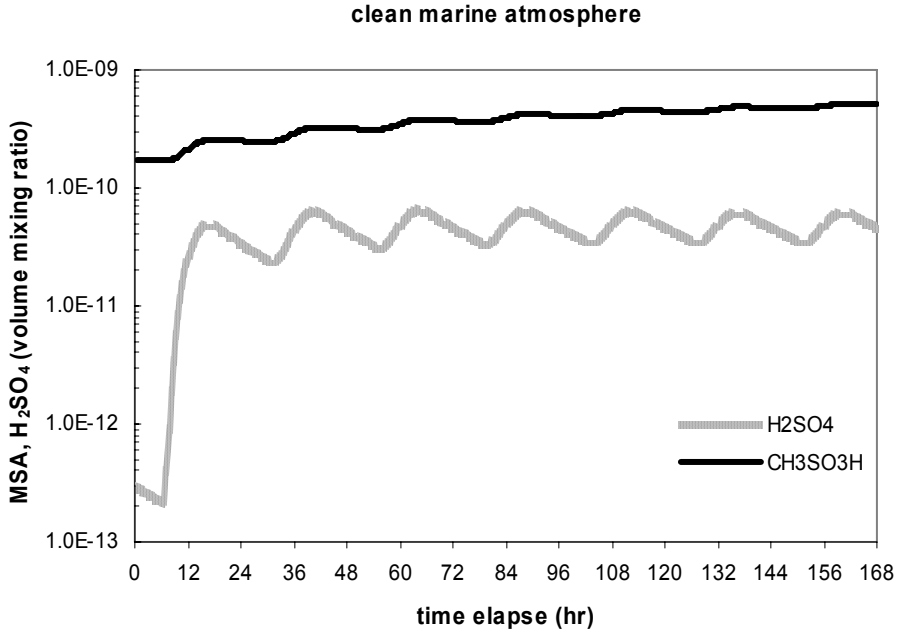

Figure D.1: Continued. (g) SO_2 and CH_3SCH_3 , (h) H_2SO_4 and CH_3SO_3H

(a)

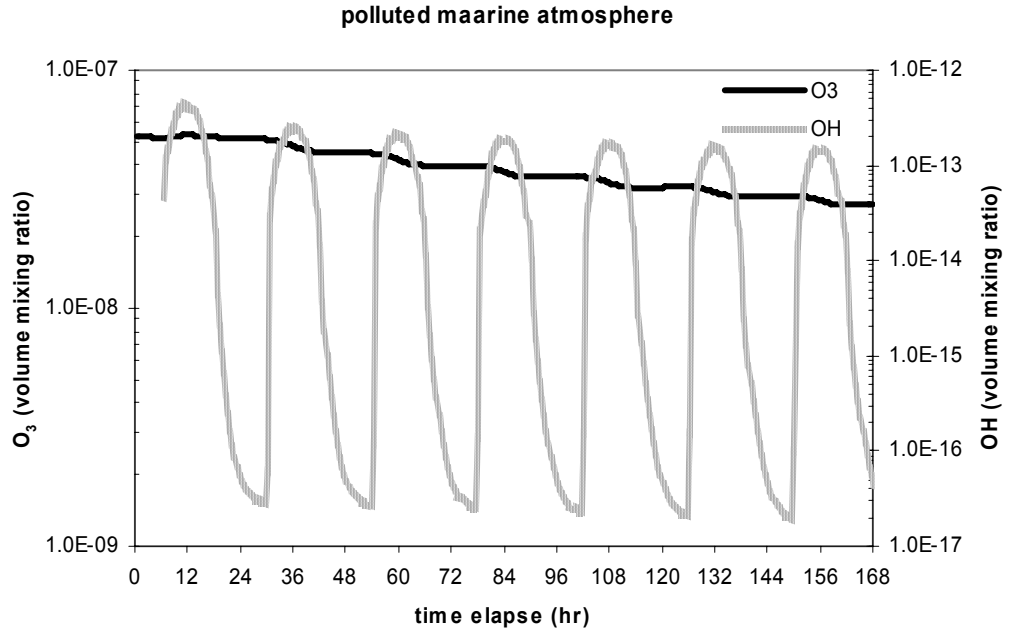

(b)

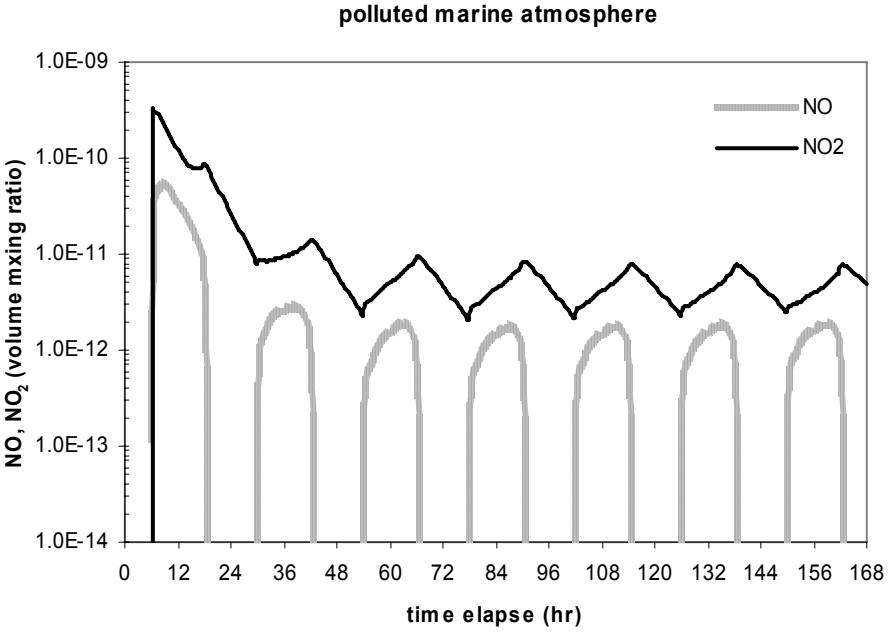

Figure D2: Diurnal cycle of atmospheric photochemical species at surface in the polluted marine environments. (a) O_3 and OH, (b) NO and NO_2

(c)

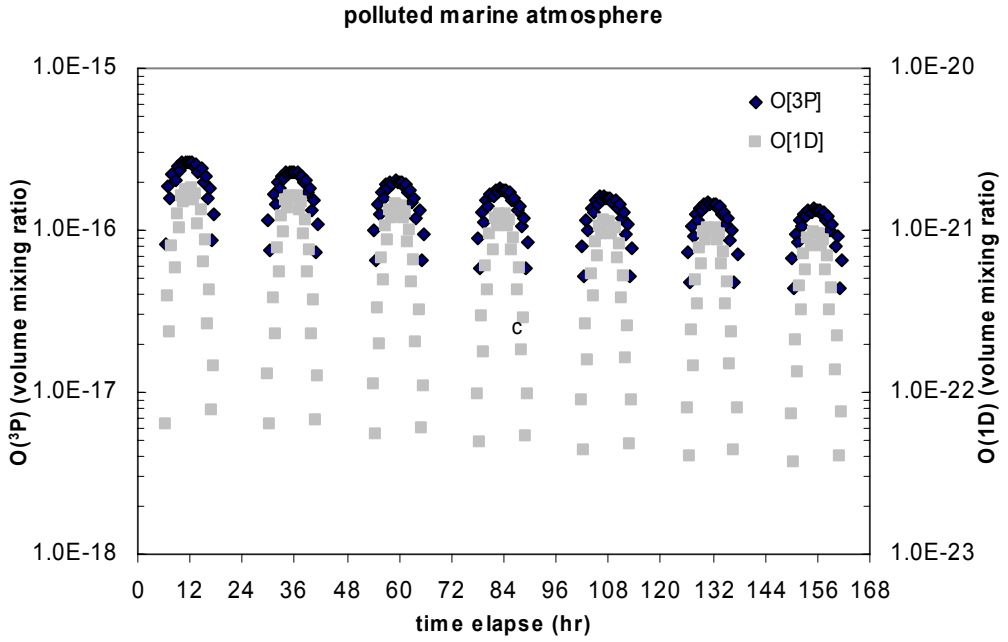

(d)

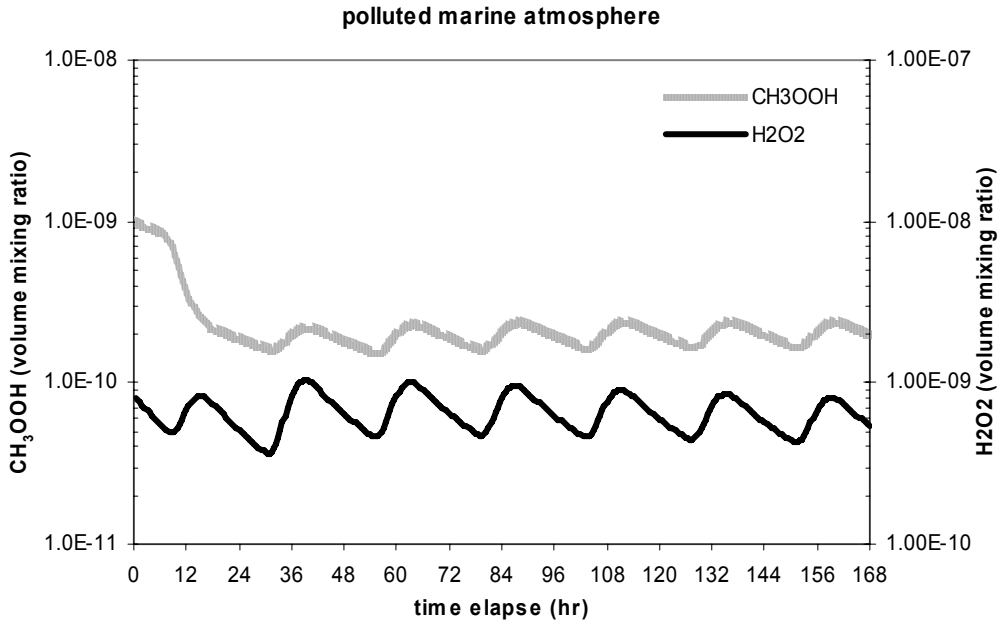

Figure D2: Continued. (c) $O(^3P)$ and $O(^1D)$, (d) CH_3OOH and H_2O_2

(e)

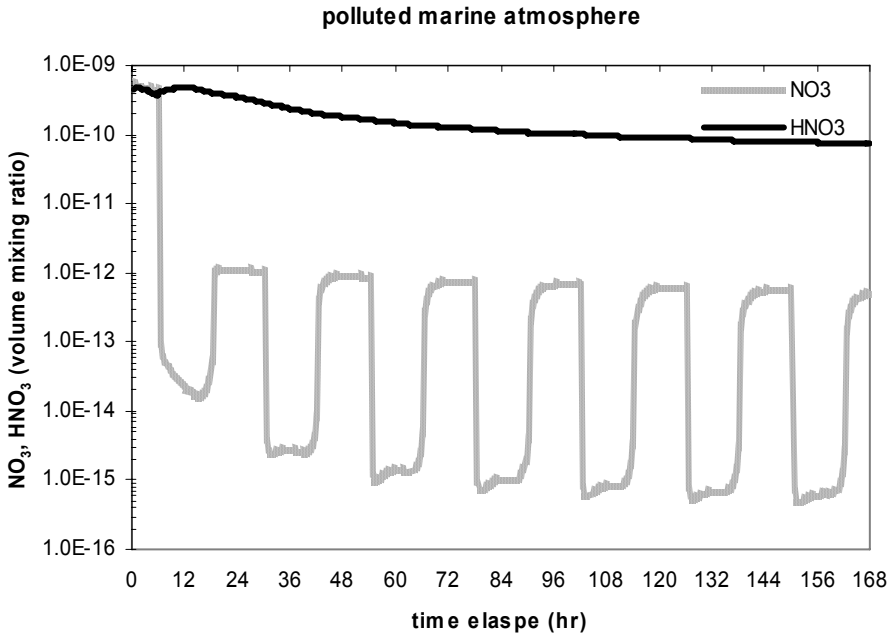

(f)

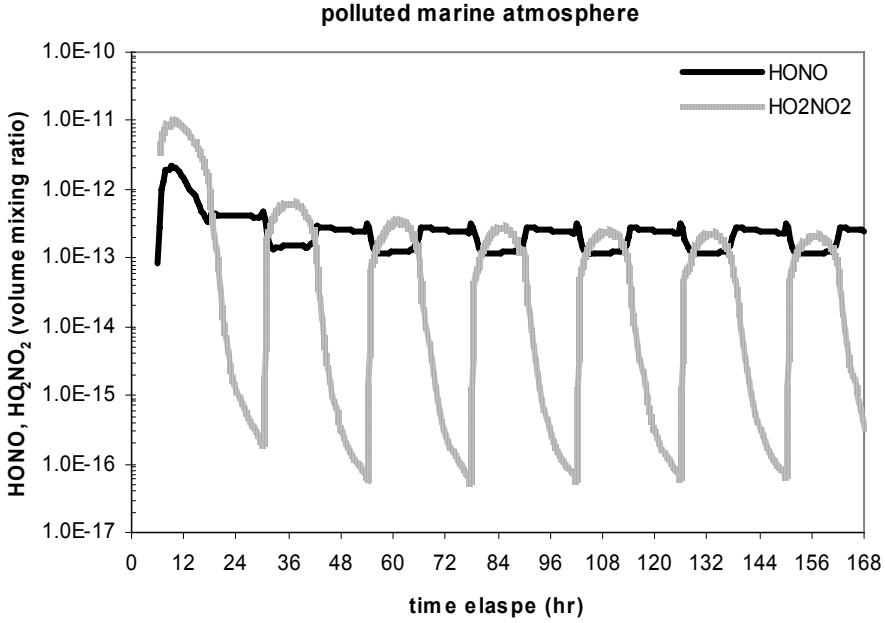

Figure D2: Continued. (e) NO_3 and HNO_3, (f) HONO and HO_2NO_2

(g)

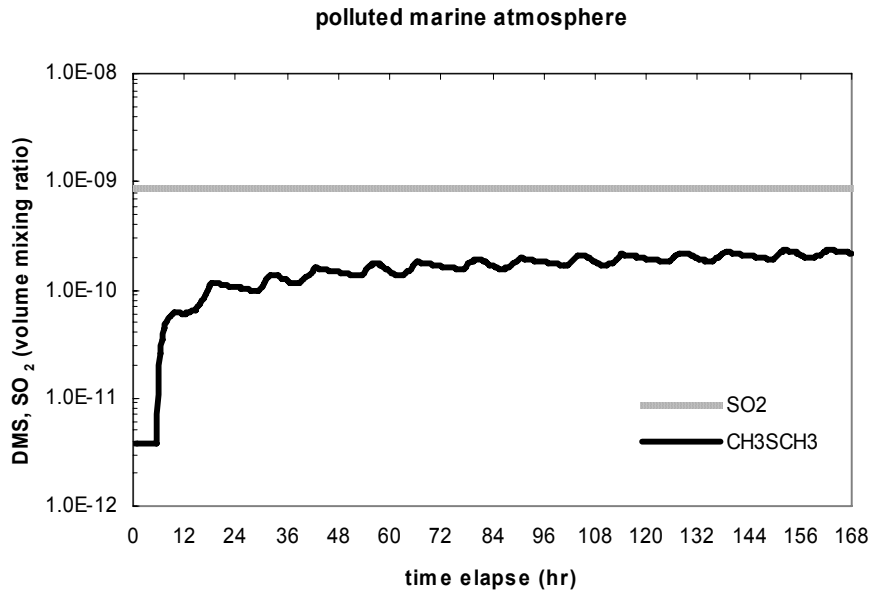

(h)

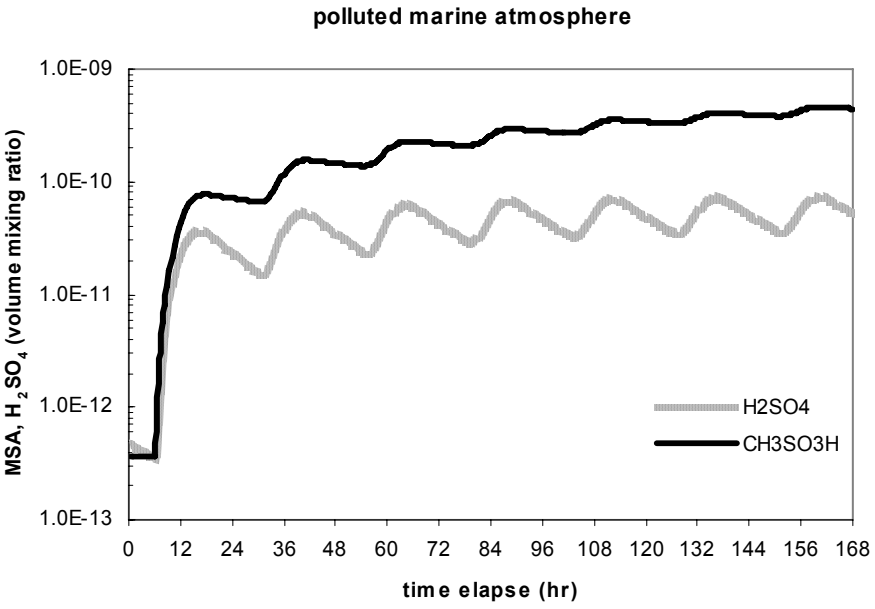

Figure D2: Continued. (g) SO_2 and CH_3SCH_3, (h) H_2SO_4 and CH_3SO_3H

REFERENCES

Alfaro, S. C., A. Gaudichet, L. Gomes, and M. Maille (1998), Mineral aerosol production by wind erosion: aerosol particle size and binding energies, *Geophys. Res. Lett.*, *25*(7), 991-994.

Alfaro, S. C., L. Gomes, J. L. Rajot, S. Lafon, A. Gaudichet, B. Charenet, M. Mallie, G. Gautenet. F. Lasserre, H. Cachier, and X.Y. Zhang (2003), Chemical and optical characterization of aerosols measured in spring 2002 at the ACE-Asia supersite, Zhenbeitai, China, *J. Geophys. Res.*, *108*(D23), 8641, doi:10.1029/2002JD003214.

Alfaro, S.C., S. Lafon, J.L. Rajot, P.Formenti, A.GAudichet, and M.Maille(2004), Iron oxides and light absorptioin by pure desert dust: An experimental study, *J. Geophys. Res.*, 109, doi:10.1029/2003JD004374.

Alebic-Juretic, A., T. Cvitas, L.Klasinc (2000), Kinetics of heterogeneous ozone reactions, *Chemosphere,* 41, 667 – 670.

Arimoto, R., Y.J. Kim, Y.P.Kim, P.K. Quinn, T.S. Bates, T.L.Anderson, S. Gong, I. Uno, M. Chin, B. J. Huebert, et al., A.D. Clarke, Y. Shinozuka, R.J. Weber, J.R. Anderson, S.A. Gauzzotti, R.C.Sullivan, D.A.Sodeman, K.A.Prather, and I.N. Sokolik (2006), Characterization of Asian Dust during ACE-Asia, *Global ad Planetary Change*, 52, 23 - 56.

Avila, A., I. Queralt-Mitjans, and M. Alarcon (1997), Mineralogical composition of African dust delivered by red rains over northeastern Spain, *J. Geophys. Res. 102*(D18), 21,977-21,996.

Bahreini, R., J. L. Jimenez, J. Wang, R. C. Flagan, J. H. Seinfeld, J. T. Jayne, and D. R. Worsnop (2003), Aircraft-based aerosol size and composition measurements during ACE-Asia using an Aerodyne aerosol mass spectrometer, *J. Geophys. Res, 108*(D23), 8645, doi:10.1029/2002JD003226.

Bauer, S.E., Y. Balkanski, M. Schulz, and D.A. Hauglustaine (2004), Global modeling of heterogenous chemistry on mineral aerosol surfaces: Influence on tropospheric ozone chemistry and comparison to observations, *J. Geophys. Res. 109*(D02304), doi:10.1029/2003JD003868.

Bauer, S. E. and Koch (2005), Impact of heterogeneous sulfate formation at mineral dust surfaces on aerosol loads and radiative forcing in the Goddard Institute for Space Studies general circulation model, *J. Geophys. Res.,* 110(D17202), doi:10.1029/2005JD005870.

Beilke, S. and Gravenhorst, G. (1978), Heterogeneous SO_2 oxidation in the droplet phase, *Atmos. Environ.*, 12, 171-177.

Bergstrom, R. W., P. Pilewskie, J. Pommier, M. Rabbette, P. B. Russell, B. Schmid, J. Redemann, A. Higurashi, T. Nakajima, and P. K. Quinn (2004), Spectral absorption of solar radiation by aerosols during ACE-Asia, *J. Geophys. Res., 109*(D19S15), doi:10.1029/2003JD004467.

Bian, H., M.J. Prather, and T. Takemura (2003), Tropospheric aerosol impacts on trace gas budgets through photolysis, *J. Geophys. Res.,* 108(D8), 4242, doi:10.1029/ 2002JD002743.

Bian, H., and C. S. Zender (2003), Mineral dust and global tropospheric chemistry: Relative roles of photolysis and heterogeneous uptake, *J. Geophys. Res.*, *108*(D21), 4672, doi:10.1029/2002JD003143.

Bond, T. C. and R. W. Bergstrom (2006), Light absorption by carbonaceous particles: An Investigative review, *Aerosol Sci. Technology*, 40, 27-67.

Bonneau, R. (1987), Wavelength dependence of quantumn yield of OH radical formation from photolysis of nitrite ion in water, *Photo-chem. Photobiol.*, 45, 723-727, 1987

Bucholtz, A. (1995), Rayleigh-scattering calculations for the terrestrial atmosphere, *Appl. Optics.*, *34*(15), 2765-2773.

Caquineau,S., A. Gaudichet, L. Gomes. and M. Legrand (2002), Mineralogy of Saharan dust transported over northwestern tropical Atlantic ocean in relation to source regions, *J. Geophys. Res.,* Vol. 107, No. D15, 4251, doi:10.1029/2000JD000247 *et al.*, 2002

Caquineau, S., A.Gudichet, L. Gomes, M. Magonthier, and B. Chatenet (1998), Saharan dust : Clay ratio as a relavant tracer to assess the origin of soil-derived aerosols*, Geophys. Res. Lett.,* Vol. 25, No.7, 983-986.

Cao, J.J., S.C. lee, X. Y. Zhang, J. C. Chow, Z.S.An, K.F. Ho, J. G.Watson.K. Fung, Y. Q. Wang, and Z.X. Shen (2005), characterization of airborne carbonate over a site near Asian dustsource regions during spring 2002 ad its climatic and environmental significance, *J. Geophys. Res.,* 110(D03203), doi:10.1029/2004JD005244.

Chang, R. Y.-W., R.C.Sullivan, and J.P.D.Abbatt, Initial uptake of ozone on Saharan dust at atmospheric relative humidity (2005), *Geophys. Res. Lett.,* 32, L14815, doi:10.1029/2005GL023317.

Claquin, T., M. Schulz, and Y.J. Balkanski (1999), Modeling the mineralogy of atmospheric dust sources, *J. Geophys. Res.*, *104*(D18), 22,243-22,256.

Clarke, A. D., Y. Shinozuka, V. N. Kapustin, S. Howell, B. Huebert, S. Masonis, T. Anderson, D. Covert, J. Anderson, H. Zin, K. G. Moore II, C. McNaughton, G. Carmichael (2004), Size-distributions and mixture of dust and black carbon aerosol in Asian outflow: Physio-Chemistry and Optical Properties, *J. Geophys. Res., 109* (D15S09), doi:10.1029/2003JD004378.

Conant, W. C., J. H. Seinfeld, J. Wang, G. R. Carmichael, Y. Tang, I. Uno, P. J. Flatau, K. M. Markowicz, and P. K. Quinn (2003), A model for the radiative forcing during ACE-Asia derived from CIRPAS Twin Otter and R/V Ronald H. Brown data and comparison with observations, *J. Geophys. Res.*, *108* (D23), 8661, doi:10.1029/2002 JD003260.

d'Almeida, G. A. (1987), On the variability of desert aerosol radiative characteristics, *J. Geophys. Res.*, *92*(D3), 3017-3027.

d'Almeida, G. A., P. Koepke, and E. P. Shettle (1991), Atmospheric aerosols, global climatology and radiative characteristics, A. Deepak publishing.

Darmenova, K. (2006), Integrated Spatiotemporal Characcterization of Dust Sources and Outbreaks in Central and East Asia, Ph.D. thesis, Georgia Institute of Technology, http://smartech.gatech.edu/bitstream/1853/10512/1/darmenova_kremana_t_200605_phd.pdf.

DeMore, W. B., S. P. Sander, D. M. Golden, R. F. Hampson, M. J. Kurylo, C. J. Howard, A. R. Ravishankara, C. E. Kolb, and M. J. Molina, Chemical kinetics and photochemical data for use in stratospheric modeling, Eval. 12 97-4, Jet Propul. Lab., Pasadena, Calif., 1997.

Dentener, F. J. and P.J.Crutzen (1993), Reaction of N_2O_5 on tropospheric aerosols: impact on the global distribution of NOx, O_3, and OH. *J. Geophys. Res.*, 98, 7149-7163.

Dentener, F.J., G.R.Carmichael, Y. Zhang, J. Lelieveld, and P. J. Crutzen (1996), Role of mineral aerosol as a reactive surface in the global troposphere, *J. Geophys. Res. 101,* No. D17, 22,869-22,889.

de Reus,M., F. Dentener, A. Thomas, S. Borrmann, J. Strom, andJ. Lelieveld (2000), Aitborne observations of dust aerosol over the north Atlantic ocean during ACE 2: Indications for heterogeneous ozone destruction, *J. Geophys. Res. 105,* No. D12, 15,263-15,275.

Dickerson, R. R., S. Kondragunda, G. Stenchikov, K. L. Civerolo, B. G. Doddridge, and B.N. Holben (1997), The impact of aerosols on solar UV radiation and photochemical smog, *Science, 278*, 827-830.

Dubovik, O., B. Holben, T. F. Eck, A. Sminov, Y. J. Kaufman, M. D. King, D. Tanre, and I. Slutsker (2002), Variability of absorption and optical properties of key aerosol types observed in worldwide locations, *J. Atmos. Sci*, *59*, 590-608.

Eschenbacher, W.L., Kullman, G.J., Gomberg, C.C. (2000), *In Patty's Industrial Hygiene*, 5th ed., Harris, R.L., Ed. Wiley New York, Vol.1.

Fuchs, N.A., and A.G. Sutugin (1970), Highly dispersed Aerosols, Ann Arbor Science Publishers, INC.

Fan, S.-M., L.W. Horowitz, H. Levy II, and W.J. Moxim (2004), Impact of air pollution on wet deposition of mineral dust aerosols, *Geophys. Res. Lett.*, 31, L02104, doi:10.1029/2003GL018501.

Galbally, I.E. and C.R. Roy (1980), Destruction of ozone at the eartj's surface, *Q.J.R. Meteorol. Soc.*, 106, 559-620

Garland, J.A.(1976), Dry deposition of SO2 and other gases, *Proc. Atmos. Surf. Exchange Particul. Gaseou pollut. 1974 Symp.*, U.S. Dep. of Commerce.

Galy-Lacaus. C., G.R. Carmichael, C.H.Song, J.P. Lacaus, H.Al Ourabi, and A.I. Modi (2001), Heterogenous processes involving nitrogen compounds and Saharan dust inferred from measurements and model calculates, *J. Geophys. Res., 106,* D12, 12559-12578.

Gary, B. L. (1989), Observational results using the microwave temperature profiler during the airborne Antarctic ozone experiment, *J. Geophys. Res.*, *94*(D9), 11,223–11,231.

Gibson, E.R., P.K.Hudson, andV.H. Grassian (2006), Aerosol chemistry and climate: Laboratory studies of the carbonate component of mineral dust and its reaction products, *Geophys. Res. Lett. 33,* L13811, doi:10.1029/2006GL026386.

Glaccum, R.A. and J. M. Prospero (1980), Saharan aerosols over the tropical North atlantic-Mineralogy, *Mar. Geol.*, 37, 295-321.

Gomes, L. and D.A.Gillette (1993), A comparison of characteristics of aerosolfrom dust storms in central Asia with soil-derived dust from other regions, *Atmos. Environ.*, Vol. 27A, No 16, 2539-2544.

Goudie, A.S.(1983), Dust storms in space and time. *Prog. Phys. Greg.*, 7, 52-530.

Grassian, V.H., (2001), Heterogeneous uptake ad reaction of nitrogen oxides and volatile organic compounds on the surface of atmospheric particles including oxides, carbonates, soot and mineral dust: implications for the chemical balance of the troposphere, *Int. Rev. Phys. Chem.*, vol 2001, No.3, 467-548.

IPCC (2007), Intergovernmental panel on climate change (IPCC), Climate Change 2007: Working Group4. The Physical Basisof Climate Change, Chapter 2. Changes in atmospheric constituents and in radiative forcing, 2.2.4.6 Mineral dust aerosols, 167 ~ 168, (http://ipcc-wg1.ucar.edu/wg1/Report/AR4WG1_Pub_Ch02.pdf)

Hanisch, F. and J.N.Crowley (2003), Ozone decomposition on Saharan dust: an experimental investigation, *Atmos. Chem. Phys.*, 3, 119-130.

He, S. and G. R. Carmichael (1999), Sensitivity of photolysis rates and ozone production in the troposphere to aerosol properties*, J. Geophys. Res*., D21, 26,307-26,324.

Hess, M., P. Koepke, and I. Schult (1998), Optical properties of aerosols and clouds: The software package OPAC, *Bull. Am. Meteorol. Soc., 79*, 831-844.

Hov Ø. (1983), One-dimensional vertical model for ozone and other gases in the atmospheric boundary layer, *Atmos. Environ.*, 17, 535-549

Jacob, D.J., J.H. Crawford, M.M.Kleb, V.S.Connors, R.J.Bendura, J.L.Raper, Glen W. Sachse, J.C.Gille, L. Emmons, C.L.Heald, (2003), Transport and chemical evoluti over the pacific (TRACE-P) aircraft mission: Design, execution, and first results, *J. Geophys. Res., 108,*D20, 9000, doi:10.1029/2002JD003276.

Jacobson, M,Z, and R.P. Turco (1994), SMVGEAR: A sparse-matrix, vectorized gear code for atmospheric models, Atmos. Environ., vol 28, No2, 273-284.

Jacobson, M.Z., (1995), Computation of global photochemistry with SMV GRAR II., *Atmos. Environ.*, 29A, 2541-6.

Jacobson, M. Z. (1998), Studying the effects of aerosols on vertical photolysis rate coefficient and temperature profiles over an urban airshed, *J. Geophys. Res*., *103*(D9), 10,593-10,604.

Jaenicke, R. (1993), Tropospheric aerosols, in Arosol-loud-Climate Interactions edited by P.V.Hobbs, pp1-31, *Academic, San Diego, Calif.*

Jickells,T.D., Z.S. An, K.K.Anderson, A.R.Baker, G. ergametti, N. Brookd, J.J.Cao, P.W.Boyd, R.A.Duce, K.A.Hunter, H.Kawahata, N.Kubilay, J.Laroche, P.S.Liss, N. Mahowald, J.M. Prospero, A.J.Ridgwell, I.Tegen, and R.Torres (2005), Global iron connection between desertt dust, ocean, biogeochemistry, and climate, *Science*, vol 308, 67-71

Kim, K. W., Z. He, and Y. J. Kim (2004), Physicochemical characteristics and radiative properties of Asian dust particles observed at Kwangju, Korea, during the 2001 ACE-Asia intensive observation period, *J. Geophys. Res., 109*(D19S02), doi:10.1029/2003 JD003693.

Krueger et al., (2004), Heterogeneous chemistry of individual mineral dust particles from different dust source regions: the implication of particle mineralogy, *Atmos. Env.* 38, 6253-6251.

Krueger, B.J., V.H. grassian, A.Laskin, and J.P.Cowin (2003), The transformation of soild atmospheric particles into liquid droplets through heterogeneous chemistry: laboratory insight into the processing of calcium cotaining mineral dust aerosol in the tropospohere, *Geophys. Res. Lett.* Vol. 30, No3,1148, doi:10.1029/2002GL016563

Kuhlmann, R.V., M.G.Lawrence, P.J.Crutzen, and P.J.Rasch, A model for studies of tropospheric ozone and nomethane hydrocarbond: Model description and ozone results, *J. Geophys. Res.,* 108, NO. D9, 4294, doi:10.1029/2002JD002893.

Lafon, S., I. N. Sokolik, J. L. Rajot, S. Caquineau, and A. Gauduchet (2006), Characterization of iron oxides in mineral dust aerosols: implications to light absorption, *J. Geophys. Res.,* 111, D21207, doi:10.1029/2005JD007016.

Laskin, A.T.W.Wietsma,T.W., B.J. Krueger, and V.H.Grassian (2005), Heterogeneous chemistry of individual mineral dust particles with nitric acid: A combined CCSEM/EDX, ESEM, and ICP-MS study, *J. Geophys. Res.* 110(D10208), doi:10.1029/2004JD005206.

Lesins G., P. Chylek, and U. Lohmann (2002), A study of internal and external mixing scenarios and its effect on aerosol optical properties and direct radiative forcing, *J. Geophys. Res., 107*(D10), doi:10.1029/2001JD000973.

Levin., S., Herbert, R., Skloot, G., Szeinuk, J, Teirstein, A., Fischler, D.Milek, G. Piligian, E. Wilk-Rivard, J. Miline (2002), Health effects of World Trade Center Site Workers, *Am. J. Ind. Med.*, 2002, 42, 545

Levin, Z., E. Ganor, and V. Gladstein (1996), The effects of desert particles coated with sulfate on rain formation in the eastern Mediterranean, *J. Appl. Meteorol.*, 35, 1511-1523.

Levin, A et al.(1990), the contribution of sulfate and desert aerosols to the acidification of clouds and rain in Israel, *Atmos. Environ.*, 24, 1143-1151.

Liao, H., P. J. Adams, S. H. Chung, J. H. Seinfeld, L. J. Mickley and D. J. Jacob (2003), Interactions between tropospheric chemistry and aerosols in a unified general circulation model, *J. Geophys. Res., 108*(D1), 4001, doi:10.1029/2001JD001260.

Liao, H., J. H. Seinfeld, P. J. Adams and L. J. Mickley (2004), Global radiative forcing of coupled tropospheric ozone and aerosols in a unified general circulation model, *J. Geophys. Res.*, 109(D16207), doi:10.1029/2003JD004456.

Liao, H., Y. L. Yung, and J. H. Seinfeld (1999), Effects of aerosols on the tropospheric photolysis rates in clear and cloudy atmospheres, *J. Geophys. Res., 104*(D19), 23,697-23,707.

Lucas, D.D. and R.G.Prinn (2004), Parametric sensitivity and uncertainty analysis of dimenthylsulfide oxidation in the remote marine boundary layer, *Atmos. Chem. Phys. Discuss.*, 4, 6379-6430.

Lucas, D.D. (2005), Mechanics, Sensitivity, and Uncertainty Studies of the Atmospheric Oxidation of Dimethylsulfide, Ph.D. thesis, Massachusetts Institute of Technology, Cambridge, MA, Center for Global Change Science Report 71, http://web.mit.edu/cgcs/www/MIT_CGCS_Rpy71.html, 2003

Mader, B., R. C. Flagan, and J.H. Seinfeld (2002), Airborne measurements of atmospheric carbonaceous aerosols during ACE-Asia, *J. Geophys. Res.*, *107*(D23), 4704, doi:10.1029/2002JD002221.

Madronich, S. (1989), Photodissociation in the atmosphere 1. Actinic flux and the effect of ground reflections and clouds, *J. Geophys. Res.*, 92, 9740-9752.

Martin R. V., D. J. Jacob, J. A. Logan, I. Bey, R. M. Yantosca, A. C. Staudt, Q. Li, A. M. Fiore, B. N. Duncan, H. Liu, P. Ginous, and V. Thouret (2002), Interpretation of TOMS observations of tropospheric ozone with a global model and in situ observations, *J. Geophys. Res.*, *107*(D18), 4351, doi:10.1029/2001JD001480.

Martin R. V., D. J. Jacob, R. M. Yantosca, M. Chin, and P. Ginoux (2003), Global and regional decreases in tropospheric oxidants from photochemical effects of aerosols, *J. Geophys. Res.*, *108*(D3), 4097, doi:10.1029/2002JD002622.

Martin, S.T., J.Shlenker, J.H. chelf, and O.W.Duckworth (2001), Structure-activity relationship of mineral dust as heterogeneous nuclei for ammonium sulfate crystallization from supersaturated aqueous solutions, *Environ. Sci. Technol.*, 35, 1624-1629

Matsumoto,J., K. Takahashi, Y. Matsumi, A. Yabushita, A Shmizu, I. Matsui, and N. Sugimoto (2006), Scavenging of pollutant acid substances by Asian mineral dust particles, *Geophys. Res. Lett.* Vol. 33, L07816, doi:10.1029/2006GL025782, 2006

Mashburn, C.D., E.K. Frinal, and M.A. Tolbert (2006), Heterogeneous uptake of nitric acid on Na-montmorillonite clay as a function of relative humidity, *J. Geophys. Res.*, 111, D15213, doi:10.1029/2005JD006525.

Meskhidze, N., W.L.Chameides, and A. Nenes (2005), Dust and pollution: A recipe for enhanced ocean fertilization? *J. Geophys. Res.*, 110, D03301, doi:10.1029/2004JD005082.

NASA Tropospheric chemistry inetrgrated data center http://www-air.larc.nasa.gov/cgi-bin/datlas.

Nishikawa, M, S. Kanamori, and T. Mizoguchi, Kosa aerosol as eolian carrier of anthropogenic material (1991), *The Science of the Total Environment*, 107, 13-27

Ooki, A. and M. Uematsu (2005), Chemical interactions between mineral dsut particles and acd gases during Asian dust events, *J. Geophys. Res.*, *110*, D03201, doi:10.1029/2004JD004737.

Patterson, E.M. and D.A. Gillette (1977), Commonalities in measured size distributions for aerosols having a soil-derived component, *J. Geophys. Res.*, *82*, 2074-2082.

Patterson, E. M., D. A. Gillette, and B. H. Stockton (1977), Complex index of refraction between 300 and 700nm for Saharan aerosols, *J. Geophys. Res.*, *82*(15), 3151-3160.

Parungo, F., Y. Kim, C-J Zhu, J. Harris, R. Schnell, X-S Li, D-Z Yang, M-Y Zhou, Z. Chen, and K. Park (1995), Asian dust storms and their effects on radiation and climate, STC RRep. 1906, Natl. Oceanic and Atmos. Admin. Air Resour. Lab, Silver Spring, Md.

Penner, J.E., C.S. Atherton, and T.E. Graedel (1994), Global emissions and models of photochemically active compounds, *Global Atmospheric-Biospheric Chemistry*, Edited by R.G. Prinn, Plenum Press, New York, pp223-247.

Penner, J.E. et. al., Aerosols, their direct and indirect effects, in Climate Cgange 2001: The Scientific Basis. Contribution of Working Group I to the Third Assessment Reoprt of th eIntergavernmental Oanel on Climate Change, edited by J.T. Houghton et al., chap.5, pp191-336, Cambridge Univ. Press, New York, 2001.

Pye, K. *Aeolian Dust and Dust Deposits*, Academic, San Diego, Calif., 1987

Reid, J. S., H. H. Jonsson, H. B. Maring, A. Smirnov, D. L. Savoie, S. S. Cliff, E. A. Reid, J. M. Livingston, M. M. Meier, O. Dubovik, and S.-C. Tsay (2003), Comparison of size and morphological measurements of coarse mode dust particles from Africa, *J. Geophys. Res.*, *108*(D19), 8593, doi:10.1029/2002JD002485.

Sano, I., S. Mukai, Y. Okada, B. N. Holben, S. Ohta, and T. Takamura (2003), Optical properties of aerosols during APEX and ACE-Asia experiments, *J. Geophys. Res., 108*(D23), 8649, doi:10.1029/2002JD003263.

Seinfeld, J. H. and S. N. Pandis (1998), *Atmospheric Chemistry and Physics*, Johan Wiley & Sons., Inc.

Sharif, S.(1995), Chemical and mineral composition of dust and its effect on the dielectric constant, *IEEE Transactions on Geoscience and remote sensing.*, vol. 33, No.2, 353-359.

Shen, Z., J. Cao, X. Li, T. Okuda, Y. Wang, X. Zhang (2006), Mass concentration and mineralogical characteristics of aerosol particles collected at Dunhuang during ACE-Asia, Advances in atmospheric Sciences, Vol. 23, No. 2, 291-298.

Shi, Z., L. Shao, T.P. Jones, and Senlin Lu (2005), Microscopy and mineralogy of airborne particles collected during severe dust storm episodes in Beijing, China, *J. Geophys.Res.110,*D01303,doi:10.1029/2004JD005073.

Smirnov, A., B. N. Holben, O. Dubovik, R. Frouin, T. F. Eck, and I. Slutsker (2003), Maritime component in aerosol optical models derived from Aerosol Robotic Network data, *J. Geophys. Res., 108*(D1), 4033, doi:10.1029/2002JD002701.

Sokolik, I.N., A. Andronova, and T. C. Johnson (1993), Complex refractive index of atmospheric dust aerosols, *Atmos. Environ., 27A*(16), 2495-2502.

Sokolik, I.N. (1999), Nuts and bolts in the radiative forcing by mineral dust, *IGACtivities Newsletter*, 24(17)

Sokolik, I. N., and O. B. Toon (1999), Incorporation of mineralogical composition into models of the radiative properties of mineral aerosol from UV to IR wavelengths, *J. Geophys. Res.*, *104*, 9423-9444.

Sokolik, I.N., O.B. Toon, and R.W.Bergstrom (1998), Modeling the radiative characteristics of airborne mineral aerosols ar infrared wavelengths, *J. Geophys. Res.*, *103*, NO. D8, 8813-8826.

Sokolik. I. N., D. M. Winker, G. Bergametti, D. A. Gillette, G. Carmichael, Y. J. Kaufmn, L. Gomes, L. Schuetz, and J. E. Penner (2001), Introduction to special section: Outstanding problems in quantifying the radiative impacts of mineral dust, *J. Geophys. Res.*,*106*(D16), 18,015-18,027.

Song, C. H. and G.R. Carmichael (2001), A three-dimensional modeling investigation of the evolution processes of dust and sea-salt particles in east Asia, *J. Geophys. Res. 106,* D16, 18,131-18,154.

Stelson, A. W. (1990), Urban Aerosol Refractive Index Prediction by Partial Molar Refractive Approach, *Environ. Sci. Technol*, *24,* 1,676-1,679.

Stockwell, W.R. (1995), On the HO_2+HO_2 reaction: Its misapplication in atmospheric chemistry models, *J. Geophys. Res.*, VOL. 100, NO. D6, PAGES 11,695–11,698, 1995

Tang, Y., G. R. Carmichael, I. Uno, J.-H Woo, G. Murata, B. Lefer, R. E. Shetter, H. Huang, R. E. Anderson, M. A. Avery, A. D. Clarke, and D. R. Blake (2003), Impacts of aerosols and clouds on photolysis frequencies and photochemistry during TRACE-P: 2. Three-dimensional study using a regional chemical transport model, *J. Geophys. Res., 108*(D21), doi:10.1029/2002JD003100.

Tang, Y., G. R. Carmichael, G. Kurata, I. Uno, R.J. Weber, C. -H. Song, S. K. Guttikunda, J. –H. Woo, D. G. Streets, C. Wei, A. D. Clarke, B. Hubert, and T. L. Anderson (2004a), Impact of dust on regional tropospheric chemistry during the ACE-Asia experiment: A model study with observations, *J. Geophys. Res.*, *109*(D19S21), doi: 10.1029/2003JD003806.

Tang, Y. , G. R. Carmichael, J. H. Seinfeld, D. Dabdub, R. J. Weber, Barry. Huebert, A. D. Clarke, S. A. Guazzotti, D. A. Sodeman, K. A. Prather, I. Uno, J.-H. Woo, J. J. Yienger, D. G. Streets, P. K. Quinn, J. E. Johnson, C.-H. Song, V. H. Grassian, A. Sandu, R. W. Talbot, and J. E. Dibb (2004b), Three-dimensional simulations of inorganic aerosol distributions in east Asia during spring 2001, *J. Geophys. Res. 109,*D17S23,doi:10.1029/2003JD004201.

Thompson, A.M., J.E.Johnson, A.L. Torres, T.S.Bates, K.C.Kelly, E.Atlas, J.P.Greenberg, N.M.Donahue, S.A.Yvon, E.S.Saltzman, B.G.Heikes,B.W.Mosher, A.A.Shashkov, and V.I.Yegorov (1993), Ozone Observation and a model of marine boundary layer photochemistry during SAGA3, *J. Geophys. Res.*, vol. 98, NO. D9, 16,955-16,968.

Thompson, A.M. and D.H.Lenschow (1984), Mean profiles of trace reactive species in te unpolluted marine surface layer, *J. Geophys.Res.89,*D3, 4788-4796.

Tie, X., G. Brasseur,L. Emmons, L. Horowitz, and D. Kinnison (2001), The effect of aerosols on tropospheric oxidants: Aglobal model study, *J. Geophys.Res.*106,22,931-22,964.

Treinin, A. and E. Hayon (1970), Absorption spectra and reaction kinetics of NO_2, N_2O_3, and N_2O_4 in aqueous solution, *J. Am. Chem. Soc.*, 92, 5821-5828.

Trochkine D., Y. Iwasaka, A. Matsuki, M. Yamada,. Y-S. Kim, T. Nagatani, D. Zhang, G. –Y. Shi, and Z. Shen (2003), Mineral aerosol particles collected in Dunhuang, china, and their comparison with chemically modifies particles collected over Japan, *J. Geophys.Res.108,*D23, 8642, doi: 10.1029/2002JD003268.

Usher, C.R., H. Al-Hosney, S.Carlos-Cuellar, and V.H.Grassian (2002), A laboratory study of the heterogeneous uptake and oxidation of sulfur dioxide on mineral dust partcles, *J. Geophys.Res.107,*D23, 4713, doi: 10.1029/2002JD00251.

Usher, C.R., A. E. Michel, and V. H. Grassian (2003), Reactions on Mineral dust, *Chem. Rev.*, 2003.

Underwood, G.M., C.H.Song, M. Phadnis, G.R. Carmichael, amdV.H. Grassian, Heterogeneous reactions of No2 and HNO3 on oxides and mineral dust: A combined laboratory and modeling study, *J. Geophys.Res. 106,* D16, 18055, 18066.

Vlasenko, A., S. Sjogren, E. Weingartner, K.Stemmler, H.W.Gäggeler, and M. Ammann (2006), Effect of humidity on nitric acid uptake to mineral dust aerosol particles, *Atmos. Chem. Phys.*, 6, 2147-2160.

Wang, J., R. C. Flagan, J. H. Seinfeld, H. H. Jonsson, D. R. Collins, P. B. Russell, B. Schmid, J. Redemann, J. M. Livingston, S. Gao, D. A. Hegg, E. J. Welton, and D. Bates (2002), Clear-column radiative closure during ACE-Asia: Comparison of multiwavelength extinction derived from particle size and composition with results from Sun photometry, *J. Geophys. Res., 107*(D23), doi:10.1029/2002JD002465.

Whitby, K. T. and B. Cantrell (1976) "Fine particles", *International conference on environmental sensing and assessments.* Las Vegas, NV, Institute of Electric and Electronic engineers.

Zender, C.B., H. Bian, and D.Newman (2003), Mineral Entrainment And Deposition (DEAD) model: Description and1990s dust climatology, *J. Geophys. Res., 108*, 4416, doi:10.1029/2002JD002775.

Zhang, X. Y., S. L. Gong, R. Arimoto, Z. X. Shen, F. M. Mei, D. Wang, and Y. Cheng (2003), Characterization and temporal variation of Asian dust aerosol from a site in the northern Chinese deserts, *J. Atm. Chemistry*, *44*, 241-257.

Zhang, Y. and G.R. Carmichael (1999), The role of mineral aerosol in tropospheric chemistry in East Asia –A model study, *J. Appl. Meteo.*, vol. 38, 353-366.

Zhang, Y., Y. Sunwoo, V. Kotamarthi, and G.R. Carmichael (1994), Photochemical oxidant processes in the presence of dust: An Evalation of the impact of dust on particulate nitrate and ozone formation, *J. Appl. Meteo.*, vol. 33, 813-824.